The Critical Role of NaCMC on Electrode Properties and Cell Performance in Lithium-Ion Batteries

Zur Erlangung des akademischen Grades eines
Doktors der Naturwissenschaften
(Dr. rer. nat.)

von der KIT-Fakultät für Chemie und Biowissenschaften
des Karlsruher Instituts für Technologie (KIT)

genehmigte

Dissertation

von

Noah Keim

1. Referent: Prof. Dr. Helmut Ehrenberg
2. Referent: Prof. Dr. Patrick Théato

Tag der mündlichen Prüfung: 06.05.2025

Kurzfassung

Diese Dissertation umfasst, wie Natriumcarboxymethylcellulose (NaCMC) die Elektrodeneigenschaften von Lithium-Ionen-Batterien beeinflusst, wobei der Schwerpunkt auf Faktoren wie Haftung, elektrischer Widerstand und Wasserrückhaltevermögen der Anoden liegt. Daran anschließend wird untersucht, wie sich diese Änderungen auf die entsprechenden elektrochemischen Zellen übertragen lassen. Dafür wird zunächst ein Ansatz basierend auf der freien Oberflächenenergie (SFE) verwendet. Damit werden NaCMCs mit unterschiedlichen Substitutionsgraden (DS) untersucht, wobei durch die SFE-Methode Zusammenhänge zwischen den Elektrodeneigenschaften und den Polymereigenschaften geschlossen werden können. Ein höherer DS verbessert die elektrische Leitfähigkeit aufgrund stärkerer Wechselwirkungen mit dem Leitfähigkeitsadditiv und zeigt gleichzeitig eine hohes Wasserrückhaltevermögen. Im Vergleich dazu verbessert ein niedrigerer DS die Adhäsion durch effektivere Wechselwirkungen mit dem Haftadditiv und dem Stromableiter, während die geringere Wechselwirkung mit den Leitfähigkeitsadditiv zu einem Anstieg des elektrischen Widerstands führt.

Das einflussreichste Ergebnis dieser Arbeit ist der Einfluss von Gelpartikeln, einer Verunreinigung in NaCMC. Es zeigt sich, dass ein höherer Gehalt an Gelpartikeln das Wasserrückhaltevermögen signifikant erhöht, was die Zellleistung beeinträchtigt, da Nebenreaktionen während der Entstehung der Festelektrolytgrenzfläche (SEI) verstärkt werden. Ein niedriger Gelpartikelgehalt zeigt ein sehr geringes Wasserrückhaltevermögen und liefert die Möglichkeit, die Sekundärtrocknung der Elektroden zu vermeiden, somit den Energieverbrauch zu senken und die Effizienz in der Herstellung zu verbessern.

Die vielversprechendsten NaCMC-Polymereigenschaftsvarianten zeigen sich bei NaCMC mit niedrigem Molekulargewicht und einem Substitutionsgrad von 0,67. Elektroden mit dieser NaCMC zeigen einen vergleichsweise geringen elektrischen Widerstand und ein dazu geringes Wasserrückhaltevermögen, welches die besten Zellergebnisse bedeutet. Die Arbeit zeigt außerdem, wie ein höheres Molekulargewicht die Menge an Restwasser in den Elektroden drastisch erhöht und damit zu einer schlechteren Zellleistung führt.

Darüber hinaus stellt diese Arbeit einen neuen Ansatz für die selektive Färbung von NaCMC mit (Heptadecafluorodecyl)-Trimethoxysilan vor, der die Visualisierung der NaCMC Verteilung in Elektroden mittels EDS ermöglicht.

Insgesamt verändert diese Arbeit die Wahrnehmung von NaCMCs, indem sie die kritische Rolle des Binders bei der Herstellung der Elektroden und den Einfluss auf die Zellleistung hervorhebt. Diese Ergebnisse erlauben es neue Wege für einen effizienteren und effektiveren Einsatz von NaCMCs in der Batterietechnologie, insbesondere für eine mögliche Reduzierung des Herstellungsaufwands und des Energiebedarfs, durch besseres Verständnis der NaCMC zu beschreiten. Zudem sollte der Gelpartikelgehalt in NaCMCs als neue Eigenschaft etabliert werden.

Abstract

This dissertation explores how sodium carboxymethyl cellulose (NaCMC) impacts electrode properties and battery performance, focusing on key factors such as adhesion, electrical resistance, and water retention. A novel approach based on the Surface Free Energy (SFE) method is used to study NaCMCs with different degrees of substitution (DS), uncovering trends that influence electrode behaviour. Higher DS improves electrical conductivity due to stronger interactions with conductive additives, while showing high water retention. In comparison, lower DS enhances adhesion by interacting more effectively with the adhesive additive and current collector, while the decrease in interaction with conductive additives leads to an increase in electrical resistance.

An innovative finding in this work is the influence of gel particle impurities in NaCMC, an area previously overlooked in the field. It is discovered that higher gel particle content drastically increases water retention, which impairs battery performance by enhancing unwanted reactions during solid electrolyte interphase (SEI) formation. Low gel particle content shows low water retention, thereby reducing the need for secondary drying, offering a significant opportunity to lower energy consumption and improve manufacturing efficiency.

Among the NaCMC polymer property variations studied, NaCMC with low molecular weight and a degree of substitution of 0.67 emerges as the most promising. It balances low electrical resistance and low water retention to deliver the best cell performance. The dissertation further showcases how higher molecular weight drastically increases water retention of the electrodes and therefore leads to worse cell performance.

Additionally, this work introduces a novel approach for selectively staining NaCMC using (heptadecafluorodecyl) trimethoxysilane, enabling visualization of its distribution in electrodes via EDS. This tool offers valuable insights for optimizing electrode design and improving the manufacturing process.

Overall, this research changes the perception of NaCMCs by emphasizing the critical role of the binder in manufacturing electrodes and the resulting cell performance. These findings open new pathways for more efficient and effective use of NaCMCs in battery technology, particularly in possibly reducing manufacturing complexity and energy demands by understanding the impact of the NaCMC in more detail. This also shows the need for establishing a new key figure for NaCMCs, the gel particle content to understand which property of the NaCMC actually affects the performance.

List of Contents

List of Figures

List of Tables

Abbreviations

AM	Active Material
CA	Conductive Additives
CB	Carbon Black
CBD	Carbon-Binder-Domain
CC	Current Collector
CC	Constant Current (only applicable in Chapter 4.5)
CEI	Cathode Electrolyte Interface
CV	Constant Voltage
DSA	Drop Shape Analysis
DIM	Diiodo Methane
DMC	Dimethyl Carbonate
DMSO	Dimethyl Sulfoxide
DS	Degree of Substitution (regarding NaCMC)
EC	Ethylene Carbonate
EDS	Energy Dispersive X-ray Spectroscopy
EG	Ethylene Glycol
EV	Electric Vehicle
HDF -TMS	(Heptadecafluorodecyl)-Trimethoxysilane
HF	Hydrogen Fluoride
HOMO	Highest Occupied Molecular Orbital
KF	Karl-Fischer
L	Liquid (regarding Surface Free Energy)
LCO	Lithium Cobalt Oxide
LEDC	Lithium Ethylene Dicarbonate

LFP	Lithium Iron Phosphate
Li^+	Lithium-Ion
LIB	Lithium-Ion Battery
LiBOB	Lithium Bis(oxalato)borate
LMC	Lithium Methyl Carbonate
LNMO	Lithium Nickel Manganese Oxide
LTO	Lithium Titanium Oxide
LUMO	Lowest Unoccupied Molecular Orbital
MW	Molecular Weight
NaCMC	Sodium Carboxymethyl Cellulose
NMC	Lithium Nickel Manganese Cobalt Oxide
NMP	N-Methyl-2-Pyrrolidone
NMR	Nuclear Magnetic Resonance
OWRK	Owens-Wendt-Rabel-Kälble
PVDF	Polyvinylidene difluoride
Py	Pyridine
S	Solid (regarding Surface Free Energy)
SBR	Styrene-Butadiene-Rubber
SEI	Solid Electrolyte Interface
SEM	Scanning Electron Microscopy
SFE	Surface Free Energy
V	Vapour (regarding Surface Free Energy)
Vol.-%	Volume Percent
Wt.-%	Weight Percent

Acknowledgement

This Dissertation was created during my work as a scientific assistant at the Institute for Applied Materials (IAM) at the Karlsruhe Institute of Technology (KIT) and contributes to the research of the Centre for Electrochemical Energy Storage (CELEST) of Karlsruhe and Ulm. The successful completion of this work was only possible due to the positive and productive environment in the research group for Energy Storage Systems. Therefore, I want to thank all the colleagues, students and partners, who were part of this environment and accompanied me on my journey.

I want to sincerely thank Dr. Werner Bauer, the group leader of my ESS research group and my supervisor during my time as a scientific assistant. He gave me the freedom to explore research topics that I found interesting and valuable. I am also very grateful to my office neighbour Dr. Marcus Müller for his guidance, patience, and the many helpful discussions that greatly advanced this work while motivating me to understand hard-to-solve challenges. Finally, I would like to thank Dr. Bayer and Dr. Petermann for their many discussions, insightful ideas, and for helping me better understand NaCMC.

I thank Prof. Dr. Helmut Ehrenberg from the Institute for Applied Materials - Energy Storage Systems (IAM-ESS) for the possibility to write this dissertation and for taking over the examination of this work together with Prof. Dr. Patrick Théato from the Institute for Chemical Technology and Polymer Chemistry (ITCP). I also thank Prof. Clare Grey for the opportunity to be a guest researcher in her group in Cambridge, as well as Dr. Chris O'Keefe for making it possible.

A special thanks to Dr. Ulrike Kauffmann, Pirmin Koch, Dr. Andreas Gyulai, Francesco Colombo, Xuebin Wu, Mattes Renner, Bianka Seitz, Bianca Ehlert, David Burger, and of course (soon to be Dr.) Andreas Weber and all the countless others creating a healthy and fun environment at work, while making the period of my PhD a memorable one.

Finally, I want to especially thank my parents, my grandparents, my expanded family, friends, and my girlfriend for always encouraging me to enjoy my time in research as much as possible and for their unconditional support.

Karlsruhe, March 2025

Noah Keim.

1 Introduction

In recent years the interest in energy storage with high energy density has steadily increased and is therefore the subject of current research and development. However, the battery research and development for those energy storage systems cannot keep up with the demand for newly created technologies. [1] Lithium-ion batteries (LIBs) still represent the gold standard when special requirements are necessary such as low weight and high energy density due to space constraints, as in electric vehicles (EVs). However, the low specific capacity of graphite, as well as the low abundance of lithium are seen as the main challenges for future LIBs. [2] To address those challenges, researchers focus on the active materials, as they take up the largest part of the electrode and directly influence the energy density or capacity. This is possible by increasing the content of the active material, using alternative materials (e.g. silicon instead of graphite) with a higher specific capacity, or completely new battery chemistries (e.g. sodium-ion batteries).

However, binders usually get overlooked, despite being an integral part of the battery. [3,4] This is mainly due to the fact, that the binder polymer only accounts for a tiny portion of the system and appears to not influence the specific capacity of the battery. In contrast, it has a major influence on the system. [2,5] Mechanically the binder is primarily contributing to the adhesion of the current collector and cohesion of the electrode itself and is supposed to create a suitable environment for the active material. [6-9] This includes the binder to be electrochemically stable and a good dispersant during manufacturing in the slurry. Finally, the binder is considered to have a possible influence on the creation of the solid electrolyte interface (SEI). [1,10,11] Considering half cells, this effect could be negligible. For full cells, losing any amount of lithium ions to side reactions drastically impacts capacity retention. Furthermore, the thickness of the SEI impacts the charge transfer resistance of the respective electrode and leads to capacity fading over time.

While the state-of-the-art manufacturing process of positive electrodes is still based on the application of harmful N-methyl-2-pyrrolidone (NMP) and polyvinylidene difluoride (PVDF), manufacturing on the negative electrodes is already transferred to water-based processing. [2,12] By using water as a solvent, the change from PVDF to a water-soluble polymer was imminent. Sodium carboxymethyl cellulose (NaCMC) combined with styrene-butadiene rubber (SBR) for increased adhesion is since used. [2,13] The change to NaCMC was based on its wide availability, low toxicity, and low cost. Additionally, NaCMC allows for tuneable properties by modifying its degree of substitution (DS) and molecular weight (MW). NaCMC therefore established itself as one of the main binders used, when manufacturing negative electrodes, as it shows good dispersive abilities, and withstands some tribochemical stress, which it is subject to during processing.

While already established for multiple years, research regarding NaCMC often focuses investigations on its rheological influence, while potentially disregarding its influence on

electrochemical aspects. [14-16] On the other hand, investigations regarding the electrochemical performance lack a wide variety of NaCMCs, therefore eventually missing influences due to different polymer properties of the NaCMC. [17] Additionally, NaCMC is not as well-studied as other polymer binders, especially compared to PVDF, and there is still limited knowledge about its properties and behaviour in LIBs. Investigations yet need to provide results for explaining interactions between the NaCMC with the active material or other components of the electrodes. Additionally, there is a lack of a more specific connection of how key polymer properties of NaCMC influence the electrochemical performance.

Therefore, the main objective of this PhD thesis is to provide insights into the impact that the NaCMC has on the overall electrode and how those findings are translated into the cell performance. This work can be divided into three different parts.

(1) The first part is focusing on the study of the interactions between the water-soluble NaCMC and the other components of the electrode. It further explores how those findings translate into electrode properties and where the boundaries of the surface free energy calculations are.

(2) The second part focuses on the influence of key properties like DS and molecular weight of the NaCMC on the cell performance and connecting them to the respective electrode properties. Additionally, the influence of a yet almost unreported impurity, the gel particles, is displayed in great detail.

(3) Finally, the challenges of staining NaCMC are shown, with a novel method allowing for the selective detection of the polymer when applied to electrodes.

2 Theoretical Background

This chapter establishes the theoretical framework essential for understanding key aspects of LIBs, serving as a foundation for the discussions that follow. It begins by explaining the fundamental principles of lithium-ion batteries. The focus of the initial part is going to be on explaining the electrochemical mechanisms, commonly used materials inside LIBs, and essential mechanisms like intercalation and the “rocking-chair” principle. The adjacent section delves into the design of battery cells, introducing the development of the industrially favoured battery cell design. It further describes some beneficial and adverse effects regarding selected cell formats.

Central to this work is the influence of polymer binder on electrodes, which contributes significantly to the mechanical and electrochemical integrity of the respective electrode and therefore the cell. The most commonly used cathode binder, polyvinylidene difluoride (PVDF) and current expectations regarding binders are therefore introduced. Special attention is given to sodium carboxymethyl cellulose (NaCMC). NaCMC is a polymer binder which is also used as a dispersant in slurry processing. It offers a promising alternative as it shows no toxicity and is water-soluble, therefore allowing researchers to avoid using organic solvents. The main focus is going to be on the synthesis, key figures of the NaCMC such as the degree of substitution, and impurities left in the final NaCMC.

In addition, the chapter also introduces the solid electrolyte interface (SEI), which is a layer forming on top of the anode material during the initial cycles of the cell and evolves over its lifetime. Furthermore, the main degradation products as well as the SEI evolution over time are going to be discussed in more detail. Additionally, the influence of impurities in the cell, such as water is also shown.

Finally, the theory of surface free energy (SFE) is introduced to provide insights into the theoretical development of the interfacial interactions of different materials. Due to different approximations, there are various theoretical developments, with the Owens-Wendt-Rabel-Kälble (OWRK) method proving to be the most applicable. As most calculations for interactions only regard those interactions in a gaseous atmosphere, it is necessary to extend the theoretical concepts further by introducing the work of van Oss. This allows for the calculation of the interaction of two solids when submerged in liquid. Following this, it becomes possible to investigate the interactions of materials during slurry processing while submerged in a solvent.

2.1 Fundamentals of Lithium-Ion Batteries

Lithium-ion batteries (LIBs) are one of the most widely used energy storage technologies in the world due to their high energy density and long cycle life as secondary batteries. Since their commercialisation by SONY in 1991, LIBs have significantly changed the landscape of energy storage systems and their application extend from portable electronics to electric vehicles (EV). [1,18-20] Especially the spatial constraints in EVs lead to a high interest in LIBs, due to them currently being the only viable option in regards to the energy density required.

LIBs consist of different active and inactive components, namely the cathode, anode, electrolyte, and separator. [3] A schematic illustrating the key components and the movement of lithium ions during the charge and discharge cycles is shown in Figure 2.1.

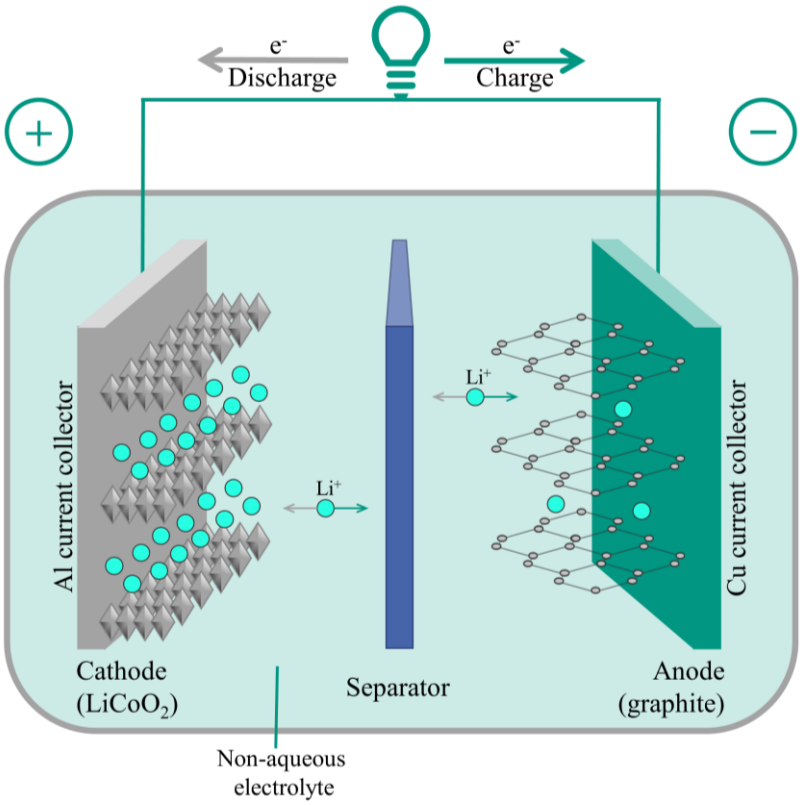

Figure 2.1: Schematic illustration of a LIB highlighting the cathode, anode, electrolyte, and external circuit (adapted from Cholewinski et al. [3]).

2.1.1 Components and Reactions in Lithium-Ion Batteries

The cathode acts as the positive electrode of the battery and is the source of lithium ions (Li^+), which leads the half-cell reaction to be represented by

$$LiMO_2 \underset{\text{Discharging}}{\overset{\text{Charging}}{\rightleftharpoons}} Li_{1-x}MO_2 + x\,Li^+ + x\,e^- \tag{2.1}$$

With the Li^+ being provided during charge and incorporated during discharge. MO_2 represents the transition metal oxide material used. Cathode materials are typically lithium-containing compounds, such as lithium cobalt oxide ($LiCoO_2$, LCO), lithium nickel manganese oxide ($LiNi_{0.5}Mn_{1.5}O_4$, LNMO), or lithium iron phosphate ($LiFePO_4$, LFP). [21] The cathode materials are chosen for their ability to provide and intercalate Li^+ while also remaining stable and providing a high reversible capacity. To further increase the energy output of layered oxides, like LCO-based materials, nickel is introduced. [1,22,23] This allows for a higher reversibly accessible specific capacity, which led it to be also used in commercial applications with nickel contents increasing from $LiNi_{1/3}Co_{1/3}Mn_{1/3}O_2$ (NMC111), to $LiNi_{0.6}Co_{0.2}Mn_{0.2}O_2$ (NMC622) and even $LiNi_{0.8}Co_{0.1}Mn_{0.1}O_2$ (NMC811).

The anode is the negative electrode in LIBs and is responsible for reversibly storing lithium ions during the charge cycle. When the battery is charging, lithium ions move from the cathode to the anode, where they are intercalated into the anode host material. The most widely used anode material in LIBs is graphite, which is a highly ordered carbon structure with layered graphene stacks. [24-26] Graphite intercalates Li^+ between its graphene layers leading to the following half-cell reaction: [27]

$$x\ C_6 + x\ Li^+ + x\ e^- \underset{\text{Discharging}}{\overset{\text{Charging}}{\rightleftharpoons}} x\ LiC_6 \tag{2.2}$$

However, graphite is categorised into different varieties in itself. [25,28] Different types of graphite, such as natural graphite and synthetic graphite, are used based on various factors like capacity, cycle life, and cost. While natural graphite is mined and processed, synthetic graphite is manufactured using petroleum or coal precursors, sometimes even leading to differences in morphology. In comparison, natural graphite tends to have higher initial capacity, whereas synthetic graphite often provides better cycle life and stability. [25,28] It has to be noted, that alternative anode materials like silicon and lithium titanium oxide ($Li_4Ti_5O_{12}$, LTO) are being studied to further enhance cell properties. Due to the different drawbacks of those anode materials, commercial usage remains largely dominated by conventional graphite due to its balance of performance, cost-effectiveness, and stability over many cycles. [24,25]

By bridging both the anode and cathode via an electrolyte, the combined reaction of both half-cells leads to

$$LiMO_2 + x\ C_6 \underset{\text{Discharging}}{\overset{\text{Charging}}{\rightleftharpoons}} Li_{1-x}MO_2 + x\ LiC_6 \tag{2.3}$$

Allowing for the repeated charge and discharge of the LIB. [29] Usually, a lithium salt dissolved in carbonates is used in commercial and research applications as an electrolyte. The most prominent electrolyte being a 1 M $LiPF_6$ dissolved in a carbonate mixture consisting of 50 vol.-% ethylene carbonate (EC) and 50 vol.-% dimethyl carbonate (DMC). [30]

While being bridged via an electrolyte, the anode and cathode have to be physically set apart to prevent a short circuit of the system while allowing for ion flow between both electrodes. [31] This

is made possible by using a porous and electrically insulating separator. For one the porosity allows for the ions to migrate freely, while the separator, being an insulator, prevents the free pass of electrons. [32-35] Currently, industrial applications commonly use polyethylene, polypropylene, ceramic composites and various other polymers. [36-39] To ensure low internal resistance, the separator has to be as thin as possible, resulting in separators being as thin as 25 µm and even thinner for general use. [40,41]

The main process to allow the storage of energy in LIBs is called intercalation. Intercalation describes the process of lithium ions (Li^+) reversibly being inserted into the vacant sites of the crystal lattices of the electrode materials. [42-44] By allowing ions to move in and out of the host material without significantly altering its structure, intercalation minimises mechanical strain on the active materials during charge and discharge cycles. This minimal stress induced by intercalation allows for achieving a high cycle life of the LIBs. While intercalation explains the storage mechanism for the active materials, the "rocking chair" mechanism describes the shuttling of Li^+ from cathode to anode and vice versa. [45] For this to be true, the metal has to be present as an ion the whole time, which is correct regarding LIBs.

2.1.2 Cell Design

For both the industry and research, the choice of the battery cell format has a significant impact on the performance, cost and long-term stability. [46,47] There are different primary cell designs namely cylindrical, prismatic, and pouch cells. Each design offers unique advantages, based on its appearance, which makes them suited for specific applications. A summary of the global market share for individual cell designs is illustrated in Figure 2.2.

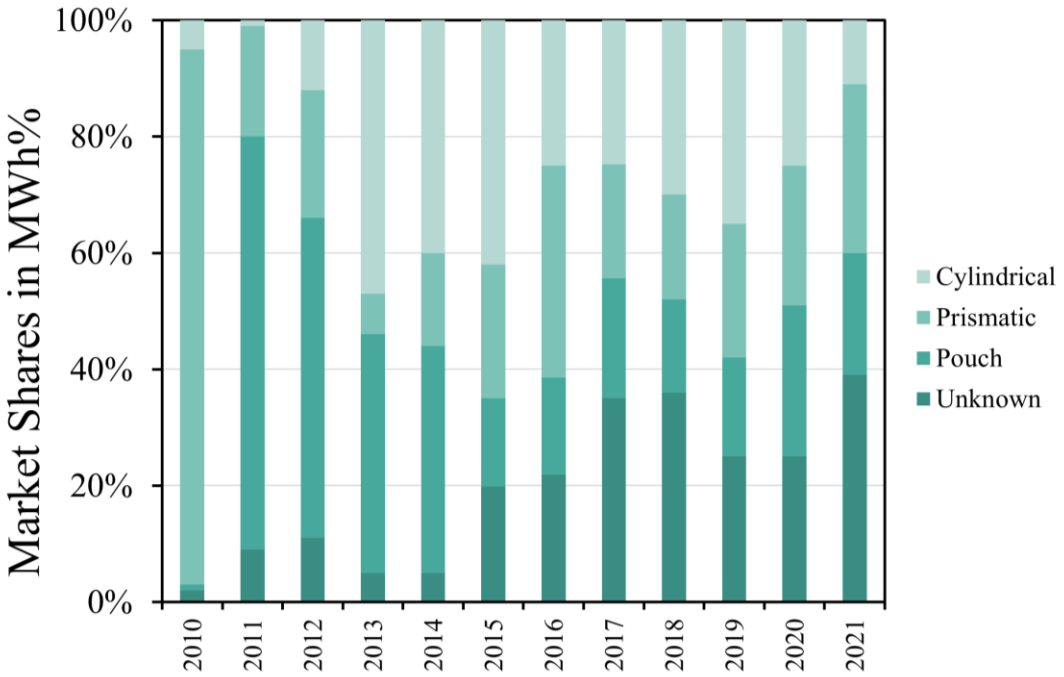

Figure 2.2: Summary of the market share of individual cell designs, from 2011 until 2021. Shares labelled unknown were not able to be assigned properly (adapted from Link et al. [46]).

Prismatic cells are widely adopted in industry and particularly in electric vehicles. [48] Cylindrical cells are often used in medical instruments and power tools. [46,49,50] Pouch cells, meanwhile, are frequently used in both consumer electronics and EVs due to their lightweight and flexible structure, though they are more prone to swelling through gas development under extreme conditions.

However, the format most used in research investigations is the coin cell format. It is often preferred for initial testing because coin cells are cost-effective and simpler to assemble, facilitating fast investigations. Nonetheless, coin cells have demonstrated limitations in replicating the long-term performance and degradation characteristics observed in larger cell formats. [47] Consequently, reliance on coin cells in early testing phases may lead to discrepancies when scaling to commercial applications, as they do not provide a fully accurate model of real-world battery ageing and stability, due to a higher ratio of electrolyte masking negative implications on the cell performance. [47,51,52] This discrepancy highlights the importance of using testing methodologies that better approximate industry conditions, like using laboratory pouch cells.

2.2 Polymer Binders in LIBs

Polymer binders only contribute a small fraction to the total amount of the electrode. [1,3] While often labelled inactive, binders have a significant impact on the electrode properties and the resulting cell performance. [4-6,53,54] The binder has a crucial part in the battery manufacturing process, particularly during electrode fabrication. One of the most commonly used manufacturing techniques is the wet coating via doctor blade or slot die. [2,4,6,55,56] This sort of electrode manufacturing involves creating a slurry, where the active material (AM), conductive additives (CA), and binder are dispersed in a solvent and then coated onto a current collector (CC) before drying. The binder has to properly deagglomerate the CAs and AMs while resisting the tribochemical strain during mixing. [57,58] This allows for a well-dispersed slurry, which ensures that the AM and CA particles are evenly distributed, while also having to prevent agglomeration. The binder also controls the slurry's viscosity, which is crucial for the coating process. [14,59] If the slurry is too viscous, it may not be coated evenly, while if it is below a certain viscosity threshold, it could fail to wet the current collector sufficiently. The drying of the electrode, when the solvent evaporates after the coating, is another critical stage. [60-63] The binder must create a dry and crack-free electrode film, by contributing proper cohesion with a low degree of binder migration. Binder migration leads to an inconsistent binder distribution which can result in defects in the dried electrode. [60,61] This negatively impacts the mechanical stability and the electrochemical performance.

Binders ensure that the active materials adhere to the current collector and that conductive additives are evenly spread throughout the electrode. This is important for maintaining good electrical contact between particles and crucial for proper electron and ion transport during cycling. [3,7-9,64] Additionally, the binder is required to create a suitable environment for the active material, not only in regards to mechanical but also electrochemical stability. This includes contributing to a proper formation of the solid electrolyte interface (SEI), allowing for proper electrolyte wetting, while simultaneously staying chemically inert and providing enough mechanical stability to withstand the strain induced by volume changes of the active material during cycling.

A schematic summary of some of the specific demands regarding an efficient binder are illustrated in Figure 2.3.

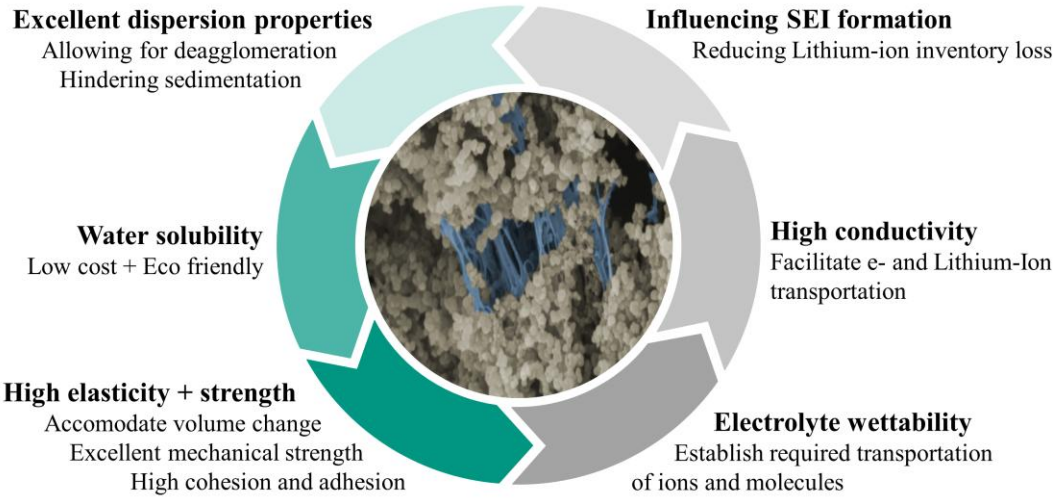

Figure 2.3: Schematic summary of the optimal properties of a binder, green shades focussing on processing and grey shades focussing on impact in cells (adapted from Cholewinski et al. [3]).

2.2.1 Polyvinylidene fluoride (PVDF)

The previously mentioned demands for binder meant a multitude of requirements a binder had to fulfil and led to the wide commercial application of polyvinylidene fluoride (PVDF). PVDF is one of the most widely used binders in LIB electrodes, particularly in cathodes, where it has become the standard. [6,65-67] Its popularity is largely due to its unique combination of properties that meet the aforementioned demands for the use in battery applications. The strong electrochemical stability allows it to operate effectively under the high voltages encountered at the cathode side. Additionally, PVDF provides sufficient adhesion strength, contributing to the mechanical integrity of the electrode. Nevertheless, PVDF is only capable of creating weak van-der-Waals interactions with other materials in the electrode. In the slurry-making process for a wet coating, PVDF is commonly dissolved in N-methyl-2-pyrrolidone (NMP).

One significant advantage of PVDF is that it has been extensively studied and characterised, particularly concerning its electrochemical behaviour, side reactions, and impact on the degradation of long-term cycling. [5,67-70] The fluorinated structure of PVDF, with its high fluorine content, is easily identifiable using analytical techniques like energy dispersive X-ray spectroscopy (EDS). [69] This makes it relatively straightforward to detect and monitor PVDF in the electrode, especially when investigating migration or degradation phenomena. PVDF's chemical composition has been shown to undergo minimal decomposition under typical battery operating conditions, making it a reliable binder choice in many applications. The extensive characterization of PVDF in terms of side reactions and migration has provided valuable insights into its long-term behaviour, and its straightforward detectability with EDS has made it a model binder for fundamental studies in binder migration and other processing related investigations.

While having some positives, there are also a multitude of drawbacks. Due to the weak van-der-Waals interactions and linear polymer structure, PVDF cannot be used as a binder for systems with significant volume expansion or high mass loading. [4,71,72] In addition to the low interactions, PVDF is also capable of swelling in electrolytes which reduces the binding capability even further. When used in carbon-based systems, like graphite anodes, PVDF possibly reacts with the lithiated graphite to form unsaturated C=C-F-bonds. [4,70,73,74] The side reaction leads to a coating which shows electronic and ionic insulating properties, which increases the overall resistance of the system. PVDF also relies on an organic solvent to be dissolved, which usually is NMP. [2,75-77] Because NMP is a harmful solvent, not only the handling of the slurry is more dangerous, but the whole manufacturing process has to be adjusted accordingly. This includes proper safety precautions in industrial scale application as well as solvent recovery during the drying of the electrode.

While PVDF remains the dominant binder in cathode applications, in anode formulations, the preferred binder choice has changed. [13,18,78] For anodes, a combination of sodium carboxymethyl cellulose (NaCMC) and styrene-butadiene rubber (SBR) has become the standard due to its improved cell performance and the possibility to interchange NMP with water as a solvent. While the improved cell performance alone would reason a change, using water as a solvent comes with further benefits, as summarised in Figure 2.4. Firstly, the whole process decreases in cost and energy consumption due to drying requiring lower temperatures and solvent recovery being expandable. Additionally, water as a resource is way cheaper in comparison to NMP, decreasing the cost from 1-3 $ per kg to only 0.015 $ per L for water. [2] Finally, the working conditions in large scale applications with water are safer in comparison to NMP, reducing the risk of work-related incidents and the need for specialised handling equipment significantly.

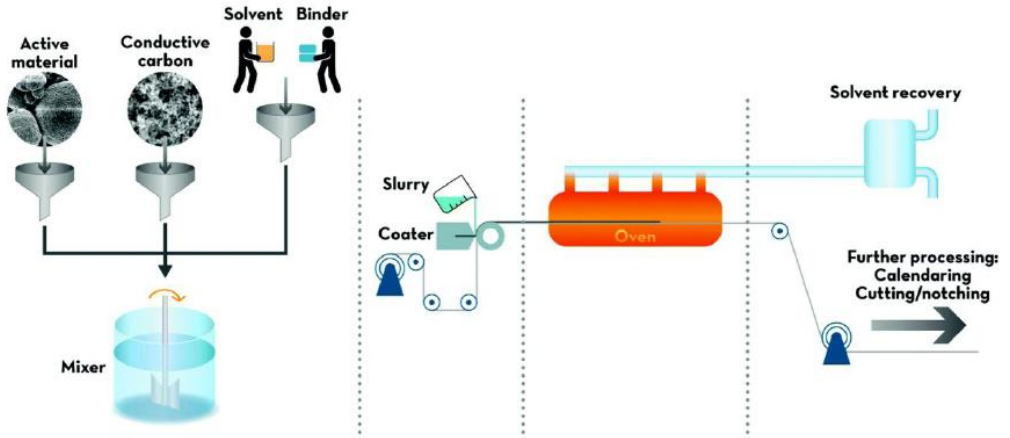

Solvent	Mixing	Coating	Drying	Recovery
NMP	Hazardous handling requires ventilation system and PSE	Controlled enviroment needed	Solvent vapours need to be collected to avoiding dispersion in the atmosphere	Recovery system required to recycle the expensive solvent
Water	PSE only required for handling of powders	Can be performed in air	No recovery necessary	Not needed

Figure 2.4: Comparison of a fictional electrode manufacturing process with one using NMP and one using water as the main solvent. Differences in the solvents are shown for each step separately (reproduced from Bresser et al. [2]).

2.2.2 Sodium Carboxy Methyl Cellulose (NaCMC)

Sodium Carboxymethylcellulose (NaCMC) is the sodium salt of carboxymethylcellulose and is entirely based on cellulose. [79] The production was already industrialised in the early 1920s in Germany and led NaCMC to become the most important ionic cellulose products in the world. [80-82] The high importance of NaCMC can be attributed to its low toxicity, water-solubility and stabilizing as well as thickening properties once dissolved. Nevertheless, while being labelled safe for human consumption, how NaCMC affects the human body is still a topic of research. [83-85] NaCMC currently is applied in a variety of applications, like in tablets, as food stabilizer, as an additive for the secondary crude oil production, in batteries and many more. [60,79,81,83-89] Depending on the application of NaCMC, the requirements of the final product can vary regarding purity and which cellulose precursor can be used for the synthesis. [79,87] Usually the quality of NaCMC is divided into food grade, industrial grade and pharmaceutical grade, depending on the amount of impurities, molecular weight and the degree of substitution. [79,87,90-92] Traditionally wood is preferred for the synthesis of pharmaceutical grade NaCMC. While NaCMC with lower requirements like food and industry grade, e.g. for crude oil, can be synthesised from a variety of cellulose precursors, like corn husk or biowaste. [87,90,92-94] A reaction scheme for the synthesis of NaCMC from cellulose, including selected side products, is illustrated in Figure 2.5. [81,92,95-97]

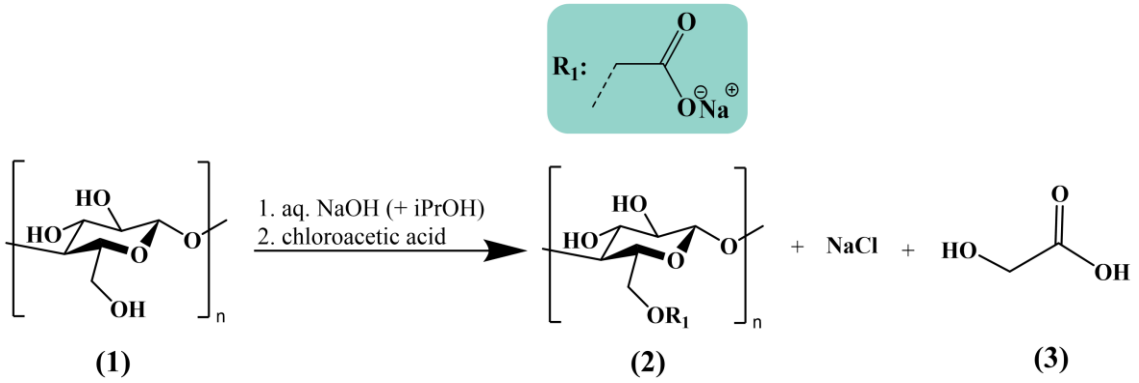

Figure 2.5: Reaction scheme of cellulose to NaCMC (DS = 1.0) with selected impurities. The different educts and products are labelled: (1) cellulose (2) NaCMC with a DS of 1.0, and (3) glycolic acid. Carboxymethyl moiety (R_1) is highlighted green.

The main reason, why the precursor varies for different qualities of NaCMC is the amount of impurities (e.g. NaCl and glycolic acid) and side products in the product (e.g. carboxymethylated hemicellulose) which vary depending on the cellulose source. [81,95] To synthesise NaCMC from the aforementioned cellulose based precursors, the cellulose source has to be dispersed in a concentrated sodium hydroxide solution for the alkalinisation of the cellulose. Alkalinisation of the cellulose is required to activate the hydroxyl groups in the cellulose to allow for swelling of the cellulose. Additionally, a process called “mercerisation” is initiated. [95,98-101] While increasing the reactivity of the cellulose, it leads to the crystalline domains of the cellulose precursors to swell as well. The alkaline solution interferes with the intermolecular interactions, leading to

penetration and swelling of the previously crystalline sections of the cellulose by the solvent. This allows for the chemicals to uniformly react with the cellulose source. [95] It furthermore leads to an equal distribution of substitution reactions of the amorphous and crystalline parts of the cellulose. Should the sodium hydroxide concentration be low, a preference of the reaction for the amorphous part of the cellulose is actually reported, showing that mercerisation is important for selectivity. [102] Additionally, if the mercerisation is not successful, low or not substituted parts of NaCMC are created, which show reduced or no solubility in water due to higher intermolecular interactions. [103]

The degree of substitution (DS), which was mentioned regarding the quality of NaCMC, is the number of substituents per repeating unit. [95,104] It gets determined via the mean average of the number of substituents across the whole sample, which can be determined through (potentiostatic) titration or different spectroscopy methods (e.g. IR spectroscopy). [96,97,105] The maximum DS possible for NaCMC therefore is three, while there is no defined lower boundary. Nevertheless, decreasing the DS below 0.2 usually leads to too many unsubstituted areas, rendering NaCMC insoluble and therefore unusable. A schematic illustration of a change in DS from 0.5 up to 3.0 is shown in Figure 2.6. The DS for application and commercially available NaCMCs usually range from 0.7 < DS < 1.2. [79,97]

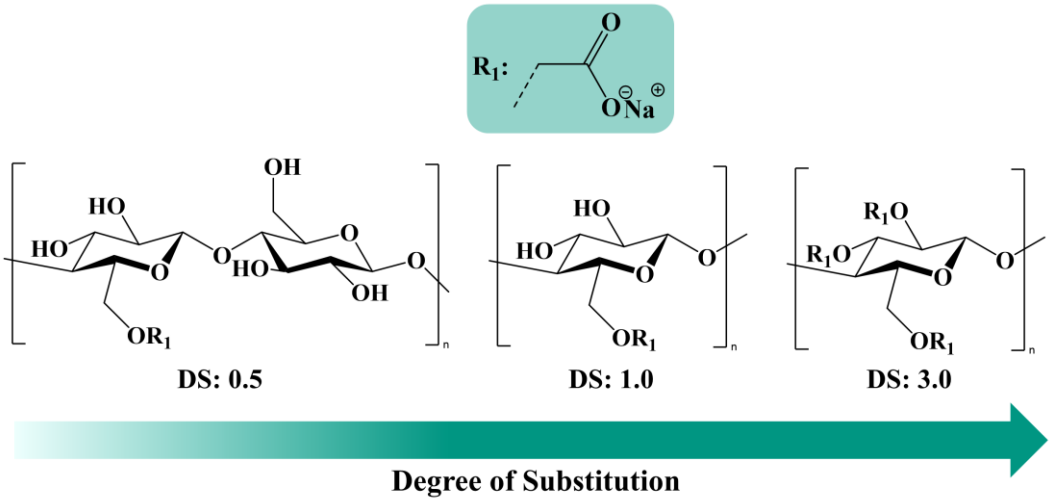

Figure 2.6: Schematic illustration to showcase the amount of carboxymethyl moieties per repeating unit and the corresponding DS of NaCMC. Showcased is a DS starting at DS = 0.5 up to DS = 1.0 and the maximum of DS = 3.0. The carboxymethyl moiety (R_1) is highlighted green.

NaCMC is more seen as a dispersant than as a binder for anodes, due to it usually being paired with SBR latex to allow for proper adhesion strength of the final electrode. Therefore, the main focus of research often tends to investigate the influence of NaCMC on processing parameters, viscosity, and the resulting impact on the slurry properties. [14-16] While the DS and molecular weight of NaCMC are identified as key factors impacting the flow behaviour of the slurry, electrochemistry often is disregarded. On the other hand, investigations regarding the electrochemistry and other electrode properties, usually investigate a select few NaCMCs without systematically understanding the influence of each key property of the NaCMC. Therefore, the influence of both key properties has to be understood in more detail.

Finally, there are additional properties of the NaCMC polymer which are poorly addressed in literature at the moment, especially side products left in the NaCMC. One of the investigated impurities of NaCMC regarding their impact on the battery performance is NaCl. But as shown in Figure 2.5 and previously explained others are present as well. Another possible side product found in NaCMC are the so-called gel particles. [106] One possible result of the gel particles is an excess of glycolic acid being present locally during synthesis, leading to a reaction between separate NaCMC polymer chains. The cross-linking reaction of the NaCMC via glycolic acid is illustrated in Figure 2.7.

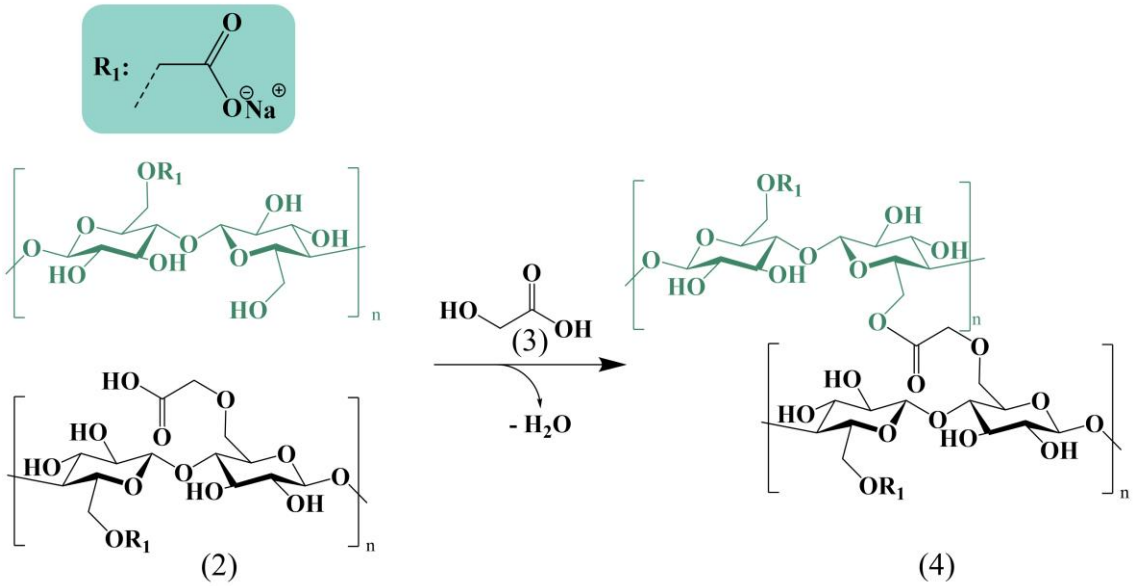

Figure 2.7: Simplified reaction scheme for the reaction of croscarmellose sodium (4) from two separate NaCMC chains (DS = 1.0) (2) via esterification catalysed by glycolic acid (3). Carboxymethyl moiety (R_1) is highlighted green (modified from Keim et al. [106]).

This reaction leads to the creation of croscarmellose sodium which could be one possible constituent of the gel particles. Croscarmellose sodium is known to be a water-insoluble particle, able to swell and to absorb water four to eight times its original volume. [107] While its swelling property makes it of interest for pharmaceutical use in tablets to control the dosage of drugs as a super disintegrant, water negatively impacts LIBs due to a variety of side reactions. [108-110] Gel particles therefore need further investigation regarding their impact on electrode quality and the resulting cell performance.

In summary, the role of NaCMC extends beyond that of a simple binder, serving as a multifunctional material whose properties can significantly influence electrode fabrication and performance. There is a knowledge gap which has to be addressed to understand how NaCMC influences the cell performances based on the impact of NaCMC on the electrode properties. Despite the long use of NaCMC, there still are unknown contributions to the NaCMCs' properties like gel particles, which have to be addressed in more detail.

2.3 Solid Electrolyte Interface on Anodes

To allow for the functionality of energy storage within a cell, both the anode and cathode are bridged by an electrolyte. When first cycling a cell, there will be a potential gap in between the electrodes and said electrolyte. [111,112] Considering, the electrodes have a uniform potential throughout, the change in potential will be present at the interface of the electrolyte and the electrode. This potential gap is widely recognised as a trigger leading to a reaction creating a transitional interface in between the electrolyte and the electrodes. [111,112] This new layer or interface balances the potential in the cell, allowing for the desired energy storage. The classification of the new interface formed is dependent on the electrode it is formed at. On anodes it is called solid electrolyte interface (SEI) while the interface on cathodes is named cathode electrolyte interface (CEI). [111,113-115] While the CEI formation has to be noted, the impact of the SEI is of higher relevancy in application, leading to higher interest in further understanding the influence on SEI formation. [10]

The aforementioned potential difference between the electrolyte and the electrode leads to the electrolyte being outside its electrochemical stable window E_g leading to the creation of the electrolyte interface. Goodenough and Kim used the frontier orbital theory to describe a cell, and propose a reason for the electrolyte interface creation, as shown schematically in Figure 2.8. [116]

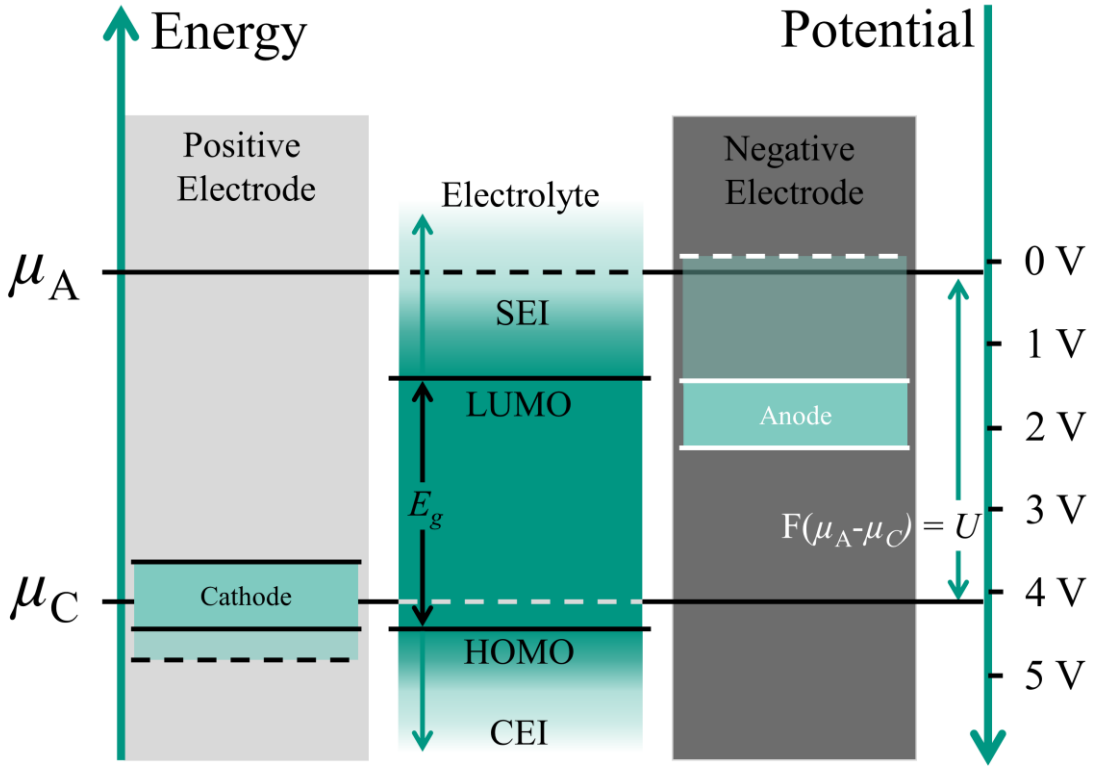

Figure 2.8: Schematic open-circuit energy diagram of an electrolyte, including a cathode, and anode. E_g: The electrochemical stability window of the electrolyte. μ_A: Redox potentials of the anode. μ_C Redox potentials of the cathode (Adapted from Li et al. [111]).

The schematic is simplified for the electrolyte to illustrate the proposed trigger for the SEI and CEI formation, due to it not considering the mixture of the different electrolyte components like co-solvents and the dissolved salt. [112] The electrolyte can be outside its electrochemically stable window E_g either at the cathode or anode. CEI formation on the cathode side depends on the highest occupied molecular orbital (HOMO) when compared to the Fermi energy of the cathode. [111,112,117,118] If the HOMO is lower, the electrolyte is stable. If the redox potential of the cathode μ_C is lower than the HOMO, the electrons of the electrolyte tend to be driven to the cathode. The electrolyte then is oxidised on the cathode side creating the CEI. On the other hand, the electrolyte is unreactive on the anode side if the lowest unoccupied molecular orbital (LUMO) is considered lower than the Fermi energy of the anode. When the redox potential of the anode μ_A is higher than the LUMO, the electrons of the anode diffuse into the orbital, creating an unstable electrolyte leading to the SEI formation. The resulting SEI should have high electrical resistance, with high permeability and selectivity of the cation, be as thin as possible (few nm) whilst being uniform, not grow over repeated cycling and resist mechanical stress induced by volume variations of the active material. [119] While the reasoning of the trigger for SEI formation is more theoretical, depending on the electrolyte used, there are various SEI components which are detected and reported. Especially considering that the LUMO of most electrolyte components is higher than the Fermi energy of lithiated graphite with approximately 0.1 eV. [111] Therefore, the creation of a SEI in real world applications is almost certain to happen.

Due to the multitude of electrolyte components, the focus is going to be on the most commonly used commercial electrolyte, LP30, consisting of EC, DMC as co-solvents and $LiPF_6$ as electrolyte salt. The most common initial degradation reactions and resulting products found in the SEI on the anode side considering the carbonates in LP30 are summarised in Figure 2.9. [10,111,119-121]

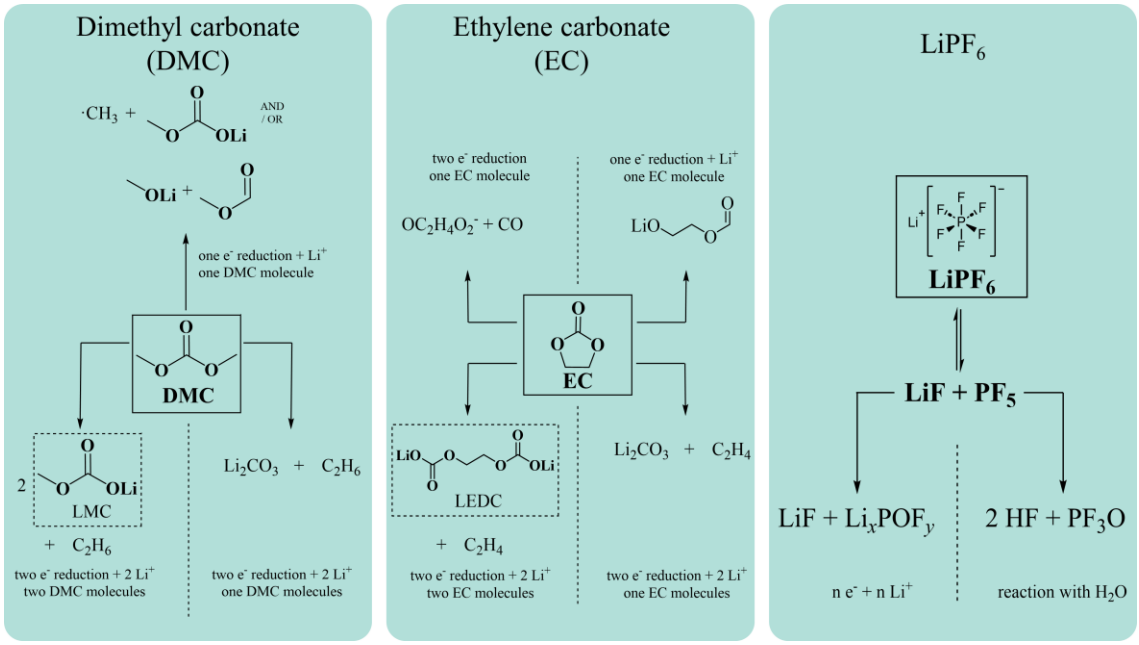

Figure 2.9: Initial degradation products for components of LP30, with DMC (a) [122-127], EC (b) [128-131], and $LiPF_6$ (c) [124,125,127] being highlighted separately. [10,111,119-121]

During the first few cycles the SEI is formed in cells, with the initial SEI being a mix of the inorganic and organic species previously shown, like lithium fluoride (LiF), lithium methyl carbonate (LMC), lithium methoxide, and lithium ethylene dicarbonate (LEDC). [10,122,123,130,131] This first SEI is dominated by the direct degradation products of the electrolyte, while cross-talk of the electrodes and cycling can lead to further variety of SEI components. Due to the initial SEI on the anode being considered unstable, it leads to a varying composition of the SEI over the lifetime of a cell. [10,132-134] The reason being that some of the organic components of the SEI are being dissolved in the electrolyte again. Especially, LEDC is dissolved again leading to a multitude of degradation products, with following products being the primary reported ones for LEDC. Equation (2.4) is regarding a thermally induced decomposition of the LEDC, while Equation (2.5) shows the reaction of LEDC with the electrolyte salt $LiPF_6$. [10]

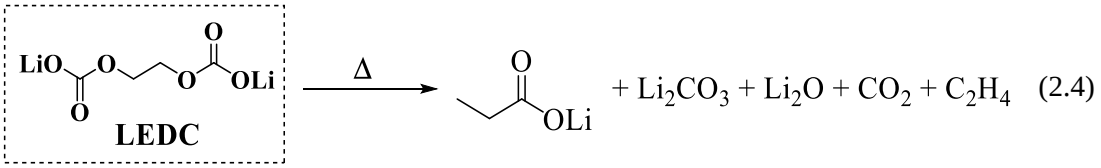

(2.4)

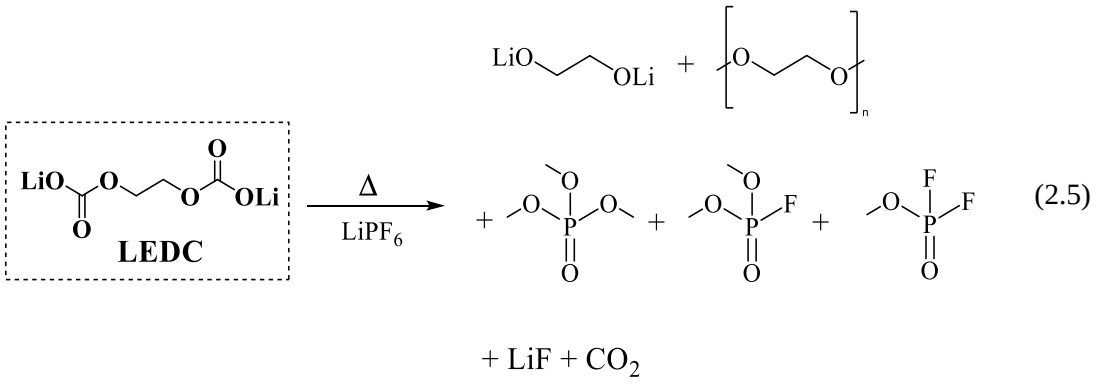

(2.5)

While reacting, the LEDC further consumes an increased amount of the electrolyte salt, in this case $LiPF_6$. A multitude of the reaction products are considered soluble, like the poly- and oligoethylene oxides, in the electrolyte or are gaseous, which indicates a lower amount of insoluble inorganic SEI components. [10] Those side reactions combined with the solubility of the LEDC leads to a porous SEI. Additionally, by dissolving the organic constituents of the SEI, there is a higher concentration of insoluble inorganic decomposition products close to the active material site. Due to new electrolyte being exchanged by decomposition products, its distance to the electrode or active material increases. Therefore, the concentration of the organic degradation products increases further away creating a gradient in the composition of the SEI. This leads to more soluble products accumulating, while in parallel, the porosity of the insoluble SEI components leads to a further reduction of the electrolyte solvents followed by an increase in thickness of the

SEI over time. This development in SEI formation and composition on top of the anode material graphite is visualised in Figure 2.10.

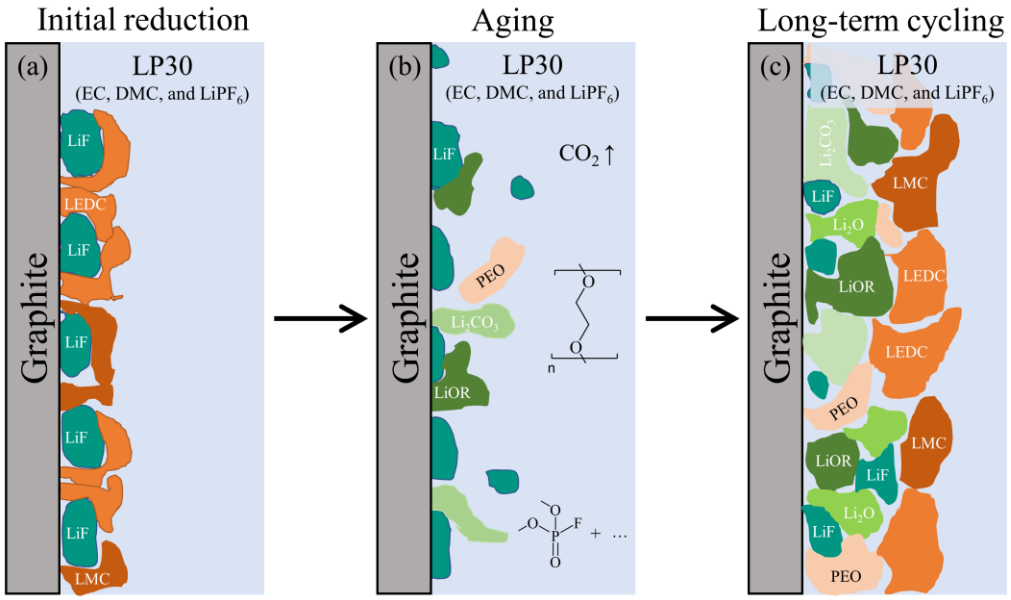

Figure 2.10: Schematic representation of SEI development on a graphite anode (a) shows the initial SEI (b) aging, which emphasises the dissolution of LEDC and the side products (c) increasing SEI thickness due to longer cycling and gradient in the SEI composition (modified from Heiskanen et al. [10]). Products are colour coded: orange shades = organic, green shades = inorganic constituents.

While those reactions are certainly true and reported a multitude of times, the degradation considers model application or ignores one of the most important impurities for electrolytes, which is water. As shown in the summary of degradation products, water enables the degradation of the electrolyte salt $LiPF_6$. [10,135] The reaction of $LiPF_6$ and water is highlighted in Figure 2.9, while the subsequent impact on components of the SEI like LMC or LEDC is highlighted in the following reaction equations:

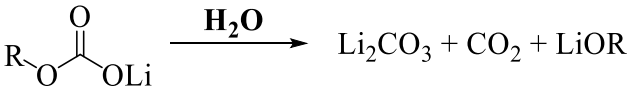

(2.6)

An increase in water therefore leads to a higher rate of degradation products. Furthermore, a multitude of the decomposition reactions are catalysed by the addition of low concentrations of acidic impurities (like H_2CO_3 and HF), which are correlated to the water concentration. While directly reacting with one of the electrolyte components negatively impacts the quality of the SEI, water readily reacts with a few components of the SEI like the LEDC and LMC. [10,135] This underlines the negative impact water has and highlights that it should be avoided to include water in the cell. It is important to note that, while the previous chapter summarises the current research, the research is still ongoing and the mechanisms behind SEI evolution are not fully understood, with the SEI being regarded as one of the most important but least understood parts of a cell. [10,112]

2.4 Surface Free Energy

By applying a liquid drop on the non-swellable surface of a solid, a droplet is formed. [136,137] By adding a tangent to the profile of the resulting droplet at the three-phase interface of vapour (V), liquid (L), and solid (S), the corresponding contact angle can be determined, see Figure 2.11. [136,138]

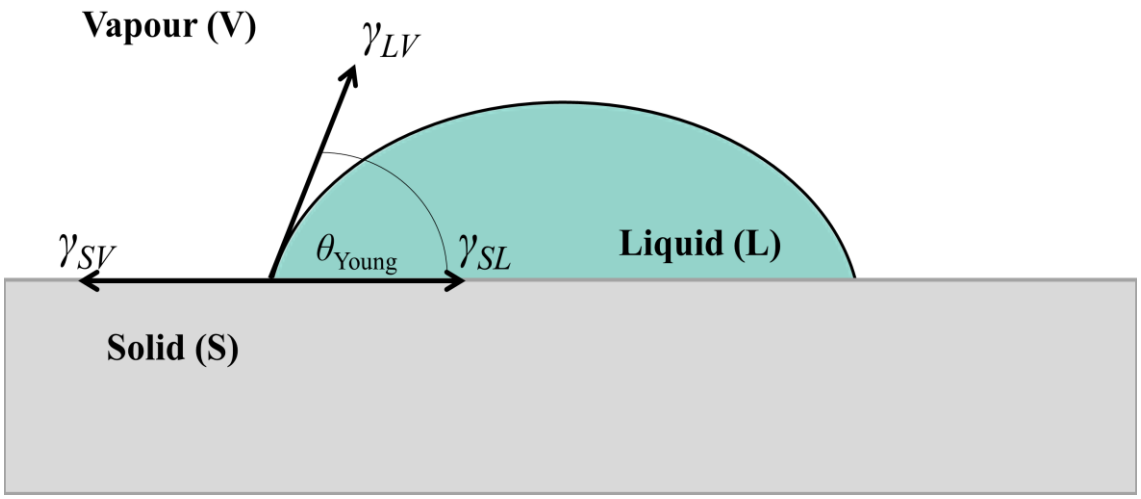

Figure 2.11: Schematic representation of a liquid droplet on a "perfect" solid surface. The contributing interfacial tensions and the tangent used to determine the contact angle θ_{Young} are shown.

2.4.1 Theoretical Framework

The contact angle first was described by Young's equation, showing the relation between the contributing interfacial tensions, resulting in: [139]

$$\gamma_{SV} = \gamma_{SL} + \gamma_{LV}\, cos(\theta_{Young}) \tag{2.7}$$

The Young equation is only viable for an ideal surface, which is smooth, non-deformable and shows no swelling behaviour for the liquids. [136,140-142] The apparent contact angle θ_{App} measured can vary from the contact angle described by the Youngs equation. [137] This hysteresis is due to the development of local energy minima, which are due to a heterogenous sample surface. [137,143,144] Therefore, more advanced relationships were developed to allow for a better description of real samples. For one, the Wenzel equation takes surface roughness and other properties of real samples into account. [138,142] The Cassie-Baxter publication further expanded on the equation by considering air inclusion in between the surface and the droplet. [145] Based on the Youngs equation, further work was done by Dupré. [146] By expressing γ_{SL} as a sum of interfacial tensions, the work of adhesion can be written as:

$$W_{SL}^{ad} = \gamma_{SV} + \gamma_{LV} - \gamma_{SL} = -\Delta G_{SL}^{IF} \tag{2.8}$$

The expression can be further simplified by combining both (2.7) and (2.8) resulting in the following equation:

$$-\Delta G_{SL}^{IF} = W_{SL}^{ad} = \gamma_{LV}(1 + cos(\theta_{Young})) \quad (2.9)$$

which is known as the Young-Dupré Equation. The work of adhesion W_{SL}^{ad} allows to calculate the theoretical force needed to separate the liquid from the solid. [146-148] Further, the expression shows, that the amount of Gibbs free energy of interfacial interaction ΔG_{SL}^{IF} released during the formation of the interface needs to be introduced as work to form two separate surfaces of the solid and liquid again. This extension of the Youngs equation now allows studying γ_{SL} through W_{SL}^{ad} which can be directly determined by measuring $\theta_{App.}$

While the work of adhesion W_{SL}^{ad} and free energy of adhesion ΔG_{SL}^{IF} can be determined this way, to further understand the surface tension and the contributing factors in more detail it required Fowkes to postulate the idea of partition of the surface tension. [149-152] Therefore γ_{SV} has a number of contributors and is given by

$$\gamma_{SV} = \gamma_{SV}^{d} + \gamma_{SV}^{P} + \gamma_{SV}^{h} + \gamma_{SV}^{i} + \gamma_{SV}^{AB} \quad (2.10)$$

Here the contributions of the dispersion (γ_{SV}^{d}), dipole-dipole interaction (γ_{SV}^{P}), hydrogen bonding (γ_{SV}^{h}), induced dipole–dipole interaction (γ_{SV}^{i}), and acid-base components γ_{SV}^{AB} for the surface tension γ_{SV} shown. By considering a solid surface only having a dispersive contribution to its total SFE, Fowkes expressed the liquid-solid interfacial tension as

$$\gamma_{SL} = \gamma_{SV} + \gamma_{LV} - 2\sqrt{\gamma_{SV}^{d} \cdot \gamma_{LV}^{d}} \quad (2.11)$$

Which would allow the determination of γ_{SV} trough θ_{App} after combination with the Young-Dupré equation. Fowkes also postulated, that the contributions for the Gibbs free energy of interfacial interaction ΔG_{SL}^{IF} can be calculated by adding the individual polar and dispersive contributions together.

$$\Delta G_{SL}^{IF} = \Delta G_{SL}^{p} + \Delta G_{SL}^{d} \quad (2.12)$$

ΔG_{SL}^{IF} showing positive values, expresses respulsion, while negative values indicate attraction between particles. Nevertheless, the previous expressions of Fowkes are only viable for solid materials with only dispersive contributions to the surface. This led the Fowkes model to be further expanded by Owens, Wendt, Rabel and Kälble (OWRK). [152-155] By approximating that the solid surface tension and the liquid surface tension are composed of the dispersion component γ^{d} and hydrogen-bonding component γ^{P} it was now expressed by

$$\gamma_{SV} = \gamma_{SV}^{d} + \gamma_{SV}^{P} \quad (2.13)$$

$$\gamma_{LV} = \gamma_{LV}^{d} + \gamma_{LV}^{P} \quad (2.14)$$

Similar to the Fowkes model in (4), γ_{SL} can be derived by assuming a geometric mean form of the polar components and is expressed by

$$\gamma_{SL} = \gamma_{SV} + \gamma_{LV} - 2\sqrt{\gamma_{SV}^{d} \cdot \gamma_{LV}^{d}} - 2\sqrt{\gamma_{SV}^{P} \cdot \gamma_{LV}^{P}} \quad (2.15)$$

Like (2.7), it again can be combined with the Young-Dupré equation leading to

$$\gamma_{LV}(1 + cos(\theta)) = 2\sqrt{\gamma_{SV}^{d} \cdot \gamma_{LV}^{d}} + 2\sqrt{\gamma_{SV}^{P} \cdot \gamma_{LV}^{P}} \tag{2.16}$$

Where there are only two unknown terms γ_{SV}^{d} and γ_{SV}^{P} left. By determining θ_{App} for multiple liquids with known γ_{LV}^{d} and γ_{LV}^{P}, the remaining terms can be calculated.

The expression then can be rewritten to

$$\frac{\gamma_{LV}(1 + cos(\theta_{Young}))}{2\sqrt{\gamma_{LV}^{d}}} = \sqrt{\gamma_{SV}^{P}}\frac{\sqrt{\gamma_{LV}^{P}}}{\sqrt{\gamma_{LV}^{d}}} + \sqrt{\gamma_{SV}^{d}} \tag{2.17}$$

Allowing to determine γ_{SV}^{d} and γ_{SV}^{P} by performing a linear fit for multiple solvents and is then evaluated when $\gamma_{LV}(1 + cos(\theta))/2\sqrt{\gamma_{LV}^{D}}$ is plotted against $\sqrt{\gamma_{LV}^{P}}/\sqrt{\gamma_{LV}^{D}}$.[156] The y-axis intercept then can be attributed to the dispersive contribution to the SFE, while the slope of the linear fit allows for the calculation of the polar contribution to the SFE. To visualise the OWRK, the process is illustrated in Figure 2.12. The different sample solvents are colour coded, with the same colour connecting the fluid with the corresponding data point in the diagram.

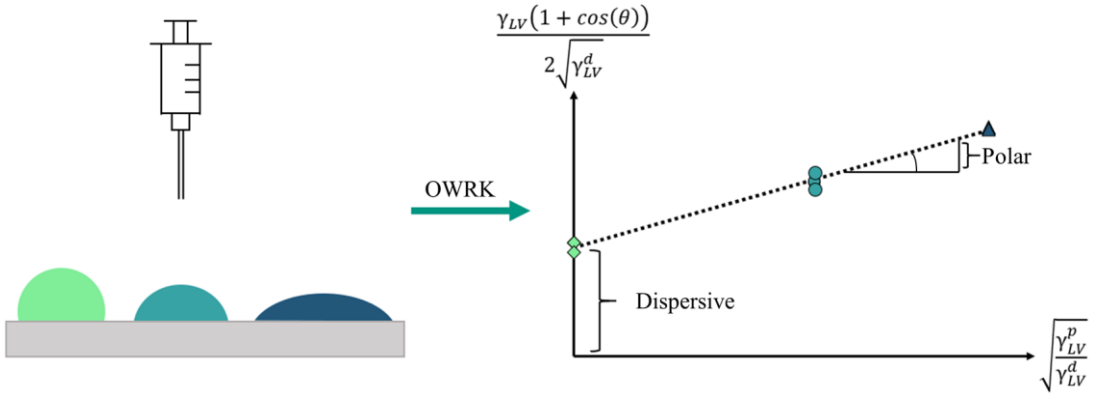

Figure 2.12: Schematic representation of the OWRK-method to dissect the surface free energy into the polar and dispersive part. Data points in diagram are coloured according to the sample liquids (reproduced from Weber et al. [157]).

All the aforementioned expressions are solely focused on a liquid system contacting a solid in a gaseous atmosphere, but are not applicable when investigating a system which is submersed in another solvent and are therefore limited. Van Oss et al. [158] expanded the previous expressions to also be viable when submerged in a liquid. [158-160] They began by further expanding the approximation of the contributing parts of the surface free energy. By including all electron-acceptor and -donor interactions for the polar interaction γ^{AB} – similar to the Lewis acid and Lewis base

concept – the polar part got extended from the previous hydrogen-bonding interactions. The electron-acceptor and donor contribution to γ^{AB} were expressed as:

$$\gamma^{AB} = 2\sqrt{\gamma^{+} \cdot \gamma^{-}} \tag{2.18}$$

With γ^{+} being the electron acceptor (Lewis acid) and γ^{-} being the electron donor (Lewis base) parameter. Additionally, the dispersive component was focused on the Lifshitz-van der Waals interaction γ^{LW} which included dipole-dipole (Keesom), induced dipole-dipole (Debye), and dispersion (London) interactions. [158-160] The expression of the surface tension for liquids and solids therefore changed to:

$$\gamma_{SV} = \gamma_{SV}^{LW} + \gamma_{SV}^{AB} \tag{2.19}$$

$$\gamma_{LV} = \gamma_{LV}^{LW} + \gamma_{LV}^{AB} \tag{2.20}$$

Similar to the work by OWRK this can be further combined with the Young-Dupré equation resulting in:

$$\gamma_{SL} = \gamma_{SV} + \gamma_{LV} - 2\sqrt{\gamma_{SV}^{LW} \cdot \gamma_{LV}^{LW}} - 2\sqrt{\gamma_{SV}^{+} \cdot \gamma_{LV}^{-}} - 2\sqrt{\gamma_{SV}^{-} \cdot \gamma_{LV}^{+}} \tag{2.21}$$

In comparison to (2.17) which is able to be solved by geometrical means, the aforementioned expression (2.21) leaves three unknowns namely γ_{SV}^{LW}, γ_{SV}^{+}, and γ_{SV}^{-}. Van Oss et al. [158] postulate, that there are liquids and solids, which only contribute to a γ^{+} or a γ^{-} parameter and are monopolar. [158,161] By being monopolar, γ^{AB} in equation (2.18) results in zero, with only the Lifshitz-van der Waals γ^{LW} contributing to the total surface free energy. Monopolar materials still are able to interact with other materials, having contributions to both γ^{AB} and γ^{LW}. This allows for the explanation of interactions of monopolar materials with bipolar systems, otherwise not included with the OWRK theory. Nevertheless, because there are no known absolute values for either the electron acceptor γ^{+} or donor γ^{-} parameter all subsequent calculations are based on an estimated value for water as reference with van Oss postulating $\gamma_{water}^{+} = \gamma_{water}^{-} = 25.5$ mJ m^{-2}. [158,162] Van Oss et al. [158]also expanded the free energy of interfacial interaction ΔG^{IF} for various cases of investigated systems. [158,163,164] When regarding only the free energy of interfacial interaction ΔG^{IF} for one material, it is expressed by:

$$\Delta G_{11}^{d} = -2\gamma_{1}^{d} \tag{2.22}$$

Where the free energy can be seen as an indicator for cohesion, as ΔG_{11}^{d} is always going to be negative and therefore implying attraction. Interactions between two materials (indexed with 1 and 2), where material 1 is a solid and material 2 can be either solid or liquid, are expressed through:

$$\Delta G_{12}^{d} = -2\sqrt{\gamma_{1}^{d}\gamma_{2}^{d}} \tag{2.23}$$

With ΔG_{12}^{d} again always being negative and therefore an indicator for adhesion.

Equations (2.22) and (2.23) both are expressions only viable in vapour atmosphere. To investigate the free energy of interaction between the surfaces of material 1 and material 2 while submersed in a liquid 3, the connection is shown in the following equation:

$$\Delta G_{132}^{d} = -2\left(\sqrt{\gamma_1^d} - \sqrt{\gamma_3^d}\right)\left(\sqrt{\gamma_2^d} - \sqrt{\gamma_3^d}\right) \tag{2.24}$$

For this equation ΔG_{132}^{d} is not always negative. Therefore, it is possible to detect repulsive or attractive forces for different surfaces submerged in a liquid. For repulsive forces either $\gamma_1^d < \gamma_3^d < \gamma_2^d$ or $\gamma_1^d > \gamma_3^d > \gamma_2^d$ need to be true. For the case, that the interaction between two surfaces of material 1 submerged in liquid are of interest, equation (2.24) can be simplified. In this case ΔG_{131}^{d}, again, is always negative and indicates attraction between same surfaces:

$$\Delta G_{131}^{d} = -2\left(\sqrt{\gamma_1^d} - \sqrt{\gamma_3^d}\right)^2 \tag{2.25}$$

Equations (2.22) to (2.25) are valid for both dispersive (superscript d) and polar contributions (superscript p) to the Gibbs free energy of interfacial interaction.

2.4.2 Practical Limitations

The contact angle determined in actual experiments is going to vary from the ideal contact angle of θ_{Young}. This is due to Young approximating a perfect homogenous surface. [137] Common surfaces are heterogeneous leading to a multitude of local energy minima allowing for meta stable apparent contact angles θ_{App} to be formed. Figure 2.13 compares the development of the contact angle hysteresis and the Gibbs free energy for an ideal surface and a real surface.

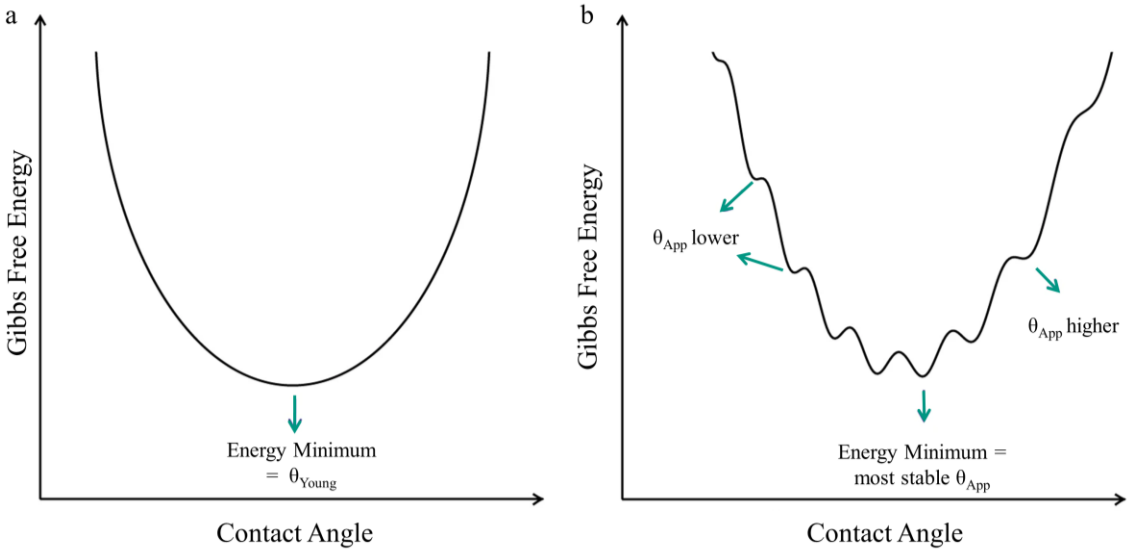

Figure 2.13: Schematic illustration of the Gibbs free energy development and hysteresis of a contact angle for a droplet on (a) an ideal (b) a heterogenous (real) surface (modified from Huhtamäki et al. [137,165]).

This is fundamental for understanding and investigating contact angles, as values may differ in samples and have to be validated through multiple measurements. Other solutions to avoid said local energy minima for an θ_{App} to be formed include the use of slight vibrations of the sample holder, as shown by Decker et al.. [166] This allows to eclipse the small energy required to go for the global minimum of energy creating a stable contact angle more closely resembling $\theta_{Young.}$

2.4.3 Application of the OWRK theory

The distinction of the SFE into the different contributions is necessary to calculate interactions and the correlating affinities of various materials. Van Oss et al. [158] further explored the interactions and expanded the equations based on OWRK. [158] This allows for the explanation of certain distinct boundaries or limitations the OWRK is subject to. Nevertheless, applying van Oss methods comes with the main drawback of only generating relative values compared to water. The OWRK method is more applicable and also used in most commercial goniometers. This leads to the OWRK method still being more applied in research in comparison to the van Oss method. While characterising individual samples via OWRK the final interpretation and calculations of the free energy of interfacial interaction ΔG^{IF} should be done considering van Oss. [167] Finally, the SFE of a material is divided into dispersive and polar contributions considering the OWRK model. For the dispersive component γ^d the value arises from the London dispersion forces (or van der Waals forces), while the polar component γ^p is considered a combination of the dipole-dipole, hydrogen bonding, and acid-base interactions of the investigated material. [154] For an improved understanding, the relative influences of the intermolecular and intramolecular interactions on the dispersive γ^d and polar component γ^pusing OWRK, are summarised in Table 2.1. [152-155]

Table 2.1: Relative influence of different interactions on the dispersive and polar component of a material.

Interaction	Effect on	
	dispersive component γ^d	polar component γ^p
van der Waals (Dispersion) Forces	High (main contributor)	Low or negligible
Hydrogen Bonding	Moderate	High (major contributor)
Metallic Bonding	High (due to delocalized electrons)	Low (unless oxidation occurs)
Ionic Interactions	Low	High (for strong electrostatic forces)
Covalent Bonding	Low to Moderate	Low (unless polar functional groups are present)

This leads to the conclusion, that nonpolar surfaces show a high dispersive component γ^d with a low γ^p. Polar surfaces on the other hand have a low to moderate dispersive component γ^d, while polar component γ^p is high.

3 Methodology

The following chapter establishes the less conventional methods used in this work and aims to provide a foundation to understand those methods. It intentionally focuses on methods that use unique set-ups and are less likely to be known. The chapter purposely excludes commonly used techniques such as scanning electron microscopy (SEM), energy-dispersive X-ray spectroscopy (EDS), nuclear magnetic resonance (NMR) spectroscopy as a separate method, and standard resistance measurements, all of which are extensively documented in the literature. [168-171]

The methods highlighted in this chapter are tailored to address the less commonly used approaches, which provide new analysis methods for active materials, electrodes and cells. These techniques complement conventional analyses by offering deeper insights into the interactions, impacts of various binders, and electrode properties that directly influence the cell performance.

First the contact angle determination via the sessile drop and Washburn method is introduced, which is necessary to calculate the SFE and connected key figures. Following, the water content is analysed using Karl Fischer titration. This precise technique is complemented by the oven method, which allows for the direct measurement of electrodes rather than only implementing other liquids. Finally, a method investigating the electrolyte stability is shown. It is observed using nuclear magnetic resonance (NMR) spectroscopy, which in this case focuses on detecting electrolyte decomposition products rather than structural characterisation. This application of NMR allows for insights into chemical changes that occur during the formation, contributing to a better understanding of degradation pathways.

3.1 Contact Angle Determination

Depending on if it is possible to create a dense sample surface or not, two different contact angle methods are required. For dense surface areas, the contact angle is determined via the sessile drop method, while powders are characterised via the Washburn method. While both give the contact angle of a sample liquid with known properties depending on a sample, the methods are fundamentally different in the determination of the contact angle and are highlighted in the following.

3.1.1 Sessile Drop Method

As described by Young, by adding a droplet on top of a dense surface, a droplet is forming. [139] The drop shape analysis (DSA) method creates images with a camera of said droplet and aligns a tangent at the three-phase interface. Figure 3.1 illustrates the setup of the method, while schematically showing the characterisation of the droplet.

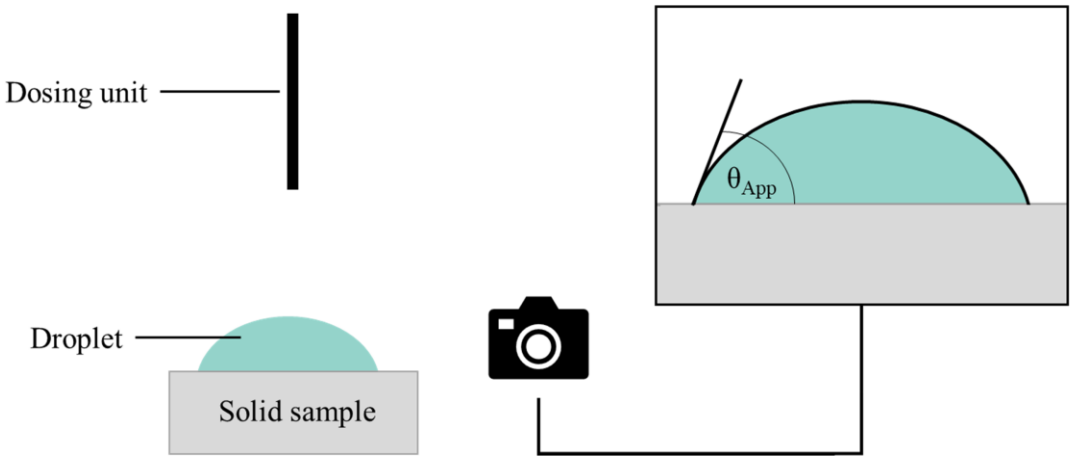

Figure 3.1: Schematic representation of the sessile drop method. Left the measurement setup is shown, while the right side shows the outline of a droplet being detected in the software, including the corresponding contact angle θ_{App}.

After the camera creates an image of the droplet, the outline of the droplet is automatically detected and fitted with a geometrical shape. Depending on the contact angle, different shapes are considered more favourable. For contact angles smaller than 10 ° a circular shape and for contact angles larger than 10 ° the shape of an ellipsis is more precise. As shown in Figure 2.13, the solid surface of samples is heterogenous creating the possibility of varying contact angles for the same surface. Therefore, multiple measurements were performed to allow for reproducibility.

3.1.2 Washburn Method

Some solids cannot form a sufficiently dense and continuous surface for an observable contact angle measurement. This leads to another method to be required to characterise these porous systems or powders and to determine the contact angles. The Washburn method accompanies that

need, by allowing the determination of the contact angle of powders. [172] Instead of directly determining the contact angle by applying a small amount of sample liquid on top of the surface, the Washburn method determines the contact angle by measuring the increase of reference liquid inside of a cylindrical test tube filled with the sample powder, thereby determining wettability. There are two further distinctions in the method, with the direct measurement of the height of the liquid front or the time dependent increase of weight with a tensiometer. Due to the measurement using a force tensiometer being more precise, it is typically used and shown in the schematic illustration of the Washburn method, see Figure 3.2. It includes the measurement apparatus, while showing the time dependent weight increase, detected via the tensiometer.

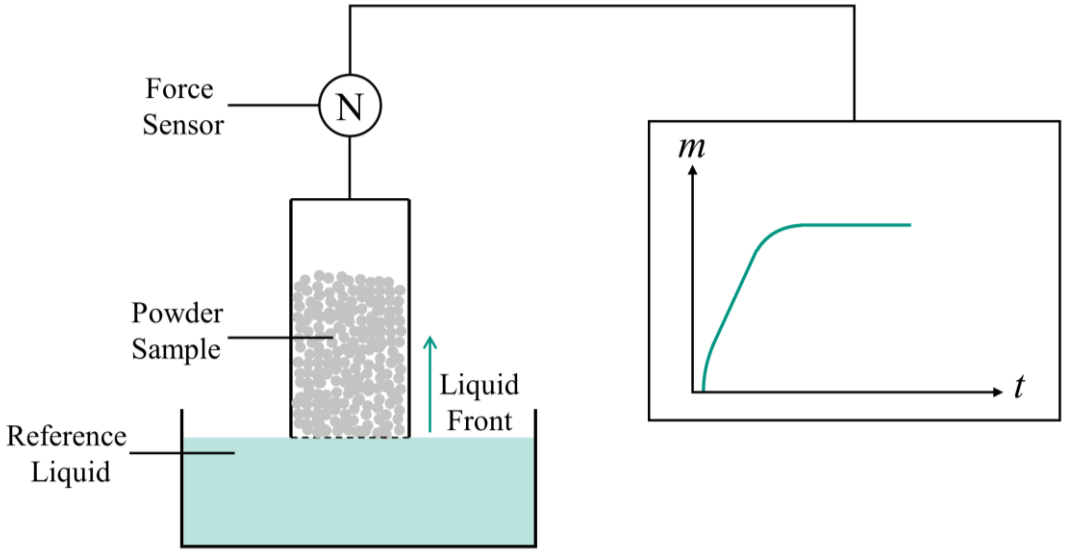

Figure 3.2: Schematic representation of Washburn method. Left the measurement setup is shown, while the right side shows the weight gain depicted over time.

Here the cylindrical sample holder contacts the reference liquid from above, leading to the weight gain of the sample, which is measured by the force tensiometer. To convert the rise of the liquid in the powder into a contact angle, the Washburn method needs some further theoretical introduction. [172] First it is necessary to approximate that the rise of the liquid is happening in parallel capillaries to use the Hagen-Poiseuille equation.

$$h^2(t) = \frac{r\,\gamma_L \cos(\theta_{adv})}{2\eta} \cdot t \tag{3.1}$$

h describes the height of the liquid front, t equals the elapsed time, r the inner radius of the capillary, γ_L the surface free energy of the reference liquid, θ_{adv} the advancing contact angle and η the viscosity of the probing reference liquid. [172] This allows to determine the flow rate inside the approximated capillaries. When using the force tensiometer it is necessary to further couple the increase in weight m of the capillary with the liquid front height h.

$$m = \rho \cdot \phi \cdot V = \rho \cdot \phi \cdot \pi R^2 h \tag{3.2}$$

With ρ being the density, ϕ being the porosity of the sample powder, and *R* being the radius of the liquid capillary. Combining both (3.1) and (3.2) results in the modified Washburn equation:

$$m^2(t) = r\phi^2(\pi R^2)^2 \cdot \frac{\rho^2 \gamma_L \cos(\theta_{adv})}{2\eta} \cdot t \tag{3.3}$$

This equation can be further simplified by summarizing $r\phi^2(\pi R^2)^2$ as the capillary constant *C*. To solve the equation for the contact angle, it is necessary to determine this constant. When using a reference liquid with a contact angle of (almost) 0 °, which equals perfect wetting conditions, it is possible to experimentally approximate this constant. [173,174] Due to the porosity ϕ and the approximated radius of the capillaries r contributing to the capillary constant *C*, having the same sample preparation and tap density is of utmost importance for creating reproduceable results. The Washburn method directly depends on the wetting of the sample powders with the reference liquids. This leads to the limitation, that no contact angle above 90 ° is detectable, as the reference liquid will not wet the surface of the sample.

3.2 Karl-Fischer Titration

To determine the water content different techniques are applied, which include drying and titration methods. In comparison to drying, using titration as a method is faster and is more selective in detecting water instead of volatile compounds. [175,176] Especially the Karl-Fischer (KF) titration shows exceptional selectivity for water, which allows it to be a very precise technique. The selectivity for water stems from the Bunsen-reaction it was based on:

$$SO_2 + I_2 + 2\,H_2O \rightarrow H_2SO_4 + 2\,HI \tag{3.4}$$

Fischer further refined the reagent to be composed of methanol and pyridine (Py) as solvents including iodine and sulphur dioxide. He postulated the reaction to be as followed:

$$2\,Py{\cdot}SO_2 + I_2 + 2\,Py + 2\,H_2O \rightarrow 2\,Py{\cdot}H_2SO_4 + 2\,Py{\cdot}HI \tag{3.5}$$

Since then, the method and reaction got understood in more detail and the technique of measuring the residual water was further modified. At this time, there are two different techniques to analyse water residue, which are coulometric and volumetric. [176,177] As volumetric implies, the technique determines the water content by measuring the volume of titrant added to the sample. This is possible, because the water content in the sample is proportional to the volume of titrant consumed. In comparison the iodine is created *in situ* for the coulometric KF titration, instead of being constantly added as for the volumetric technique. The coulometric titration cell combines sulphur dioxide, an organic base, iodide, and an alcohol as solvent. The iodine necessary to allow for the titration of the water is created through the anodic reaction of iodide: [178]

$$2\,I^- \rightarrow 2\,e^- + I_2 \tag{3.6}$$

This allows for the residual water amount to be directly correlated to the current required to create the iodine. By using the current instead of the volume, the amount of residual water inside of a sample can be drastically lower. As shown previously, the amount of water can directly correlate

with cell performance, which led to researches being interested in applying the method in the battery field. With the direct setup of measuring a sample dissolvable in the titrant, the electrolyte was the first part of the cell, being investigated thoroughly. Nevertheless, due to water only being detected in traces, some other electrolyte components led to side reactions with the apparatus, like hydrofluoric acid (HF), or lithium bis(oxalato)borate (LiBOB). [179] Parallel to resolving the challenges of other electrolyte component, the technique was refined even further to allow for the detection of residual water in electrodes. [180-182] This was possible by further expanding the KF setup, by including a separate heating chamber, which was interconnected with the KF titration. While heating, the residual water is vaporised. The dried gas then carries the gaseous water into the KF titration where it reacts with the iodine. The indirect coulometric KF titration, or KF oven technique is illustrated in Figure 3.3.

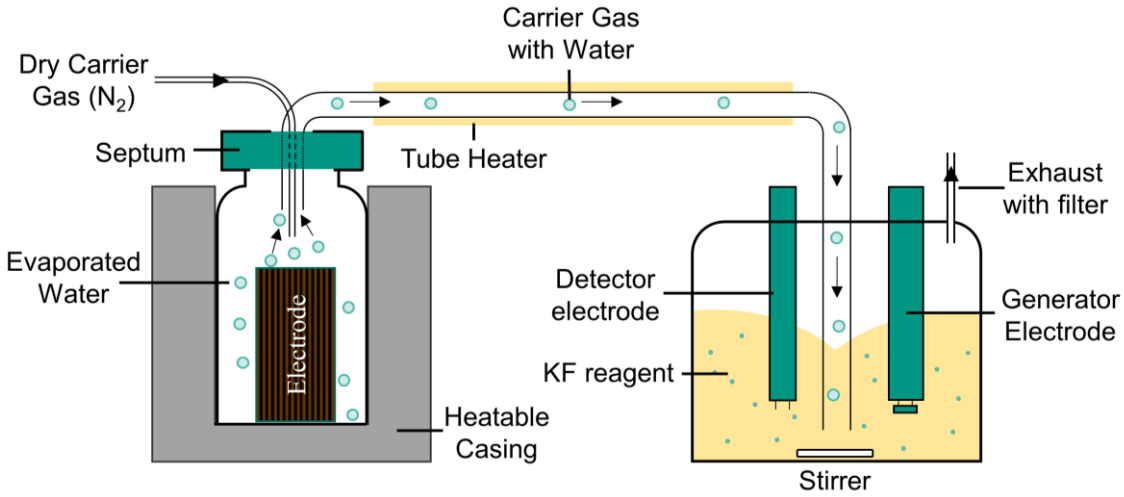

Figure 3.3: Schematic representation of the indirect coulometric Karl-Fischer titration, including the heat able casing for evaporating the water on the left and the schematic coulometric KF titration chamber on the right (modified from Kosfeld et al. [182]).

3.3 Electrolyte decomposition via NMR

There are various spectroscopic methods, e.g. energy dispersive X-ray spectroscopy (EDS) and X-ray photoelectron spectroscopy (XPS), to understand the electrolyte degradation pathways of the carbonates and the dissolved salt. The most prominent technique to investigate the surface of the SEI is XPS, with its main focus being the investigation of the precipitated components on top of the electrode. [183,184] While both EDS and XPS are necessary and irreplaceable in understanding the composition of the SEI, one of the major drawbacks for both is the requirement of high vacuum conditions, rendering the detection of volatile components hardly possible. Another drawback of said method is the possible degradation of the SEI components as well as the variation of etching time, depending whether the component is either inorganic or organic. [184] Furthermore, while the products of the electrolyte degradation become apparent with XPS, the pathway of reactions still is unknown.

Liquid NMR in comparison is a method solely focused on the measurement of different nuclei in a magnetic field. This allows for the investigation of the soluble decomposition products of the electrolyte, and understanding underlying reaction mechanisms. [185,186] The NMR measurement allows for different strategies to further distinct which component influences the degradation mechanism. As shown previously in Figure 2.9, different carbonates result in the same degradation products. By interchanging selected atoms with their corresponding isotope, for example substituting ^{16}O with ^{17}O, it is possible to mark individual reactants. By marking them, the degradation pathways can become traceable and be understood in more detail. Further separating the electrode degradation products, means the cross-talk between anode and cathode has to be prohibited, or prevented. Prohibiting the cross-talk equals prohibiting the diffusion between the cathode and anode, effectively hindering the electrolyte to bridge the anode and cathode. Using a lithium-ion conducting glass ceramic in between the liquid electrolyte allows for the separation of both electrolyte compartments, as it only allows lithium ions to pass. [185] Degradation products are hindered to migrate into the other compartment, and are only detected at the electrode where they were produced.

While separating the two electrode compartments is working, it is expensive and cycle rates have to be slow to accommodate the lithium ion diffusion through the dense ceramic separator. Alternatively, the creation of side products on the cathode side could be prohibited, so cross-talk is not interfering with the investigations of the SEI. [186] The used cathode material has to show a voltage plateau, while being stable in the carbonate electrolyte to not initiate any degradation. With a $LiFePO_4$ based electrode this is possible, as the voltage plateau is at approximately 3.45 V which leads to no degradation in the system. [186-189] Therefore, only the anode initiates degradation of the electrolyte. By prohibiting the CEI formation, detected products are reasoned to be caused by degradation on the anode side. The used electrolyte is then further diluted in deuterated solvent and measured via the NMR technique. With NMR investigating different nuclei, the ones of most interest usually are hydrogen ^{1}H, carbon ^{13}C, oxygen ^{17}O, fluorine ^{19}F, and phosphorous ^{31}P.

4 Experimental

4.1 Materials

The focus of this PhD thesis is on the influence of the various NaCMC polymer properties on anodes and their cell performance. If not stated differently, the following composition was used for all electrodes, see Table 4.1.

Table 4.1: Materials with corresponding manufacturer and the final composition in the dry anode.

Reference	Name	Manufacturer	Final anode in wt.-%
Graphite (natural)	MechanoCap 1P1	H.C. CARBON, Germany	96.0
CB	C-NERGY Super C65	Imerys Graphite & Carbon, Switzerland	1.5
SBR	TRD 2001	JSR Micro, Belgium	1.25
NaCMC	Various	IFF Speciality Products, Germany	1.25

The main polymer properties of NaCMC, which got varied were degree of substitution (DS), molecular weight (MW), and the absolute amount of gel particles. A summary of all NaCMCs used and their corresponding properties is given in Table 4.2. [190] To acquire the gel particle count, a pure NaCMC coating was applied on surface treated sample holder of 25 cm^2 and counted via optical microscope. The gel particle amount for the high molecular weight was not included by the supplier. Additionally, not all molecular weights were included to every experimental batch of NaCMC. It is important to note, that NaCMC is produced based on viscosity specifications rather than molecular weight. The viscosity is dependent on both the molecular weight and the DS of each NaCMC. NaCMCs fulfilling a higher viscosity threshold are considered to show a higher molecular weight in comparison to NaCMCs with the same DS, which create lower viscosity solutions. The same classification was therefore used in this work. NaCMCs with a viscosity threshold of 2000 mPa s are going to be labelled low molecular weight, while NaCMCs with a viscosity threshold of 20000 mPa s are going to be labelled high molecular weight.

4.2 Electrode manufacturing

To manufacture electrodes wet-processing through slurry coating with a doctor blade was used. The slurry was dispersed using a dissolver (Dispermat CA60, VMA Getzmann, Germany) with a 50 mm toothed disk in a batch container with a volume of 250 mL, while placed in a casing which was cooled by 20 °C water. A 2 wt.-% NaCMC solution was created prior to the mixing, by dissolving NaCMC in deionised water. A powder mixture of graphite and CB was added

continuously into the NaCMC solution in 15 minutes, while stirring with a tip speed of 1.5 m s^{-1}. After completely adding the powder mixture, the tip speed was increased to 5 m s^{-1} and kept constant for 45 minutes. Following this long dispersion step, the shear-sensitive SBR latex was added, which was combined with degassing (100 to 200 hPa) and a reduced stirring speed of 1 m s^{-1}. The final water content was adjusted to create a slurry with a solid content of 56 wt.-%. The created slurry then was poured onto a 10 µm copper foil for roll-to-roll coating (KTFS, Mathis AG, Switzerland) with a doctor blade and a wet-film thickness of 75 µm. The two corresponding drying chambers had of 25 °C and 30 °C, while the coating was limited to a web speed of 0.2 m min^{-1}. The areal capacity was set at 2.1 ± 0.1 mAh cm^{-2}.

Table 4.2: Summary of the variation of NaCMCs used in the subsequent work and the NaCMCs corresponding properties. The abbreviation depicts the DS and the molecular weight of the NaCMC. The last abbreviation for gel particles depicts the amount of different gel particles in a NaCMC with the same polymer properties.

Abbreviation	DS	MW in kDa	No. of Gel particles [a)]	Viscosity [b)] in mPa s
$CMC_{0.34,\ low\ MW}$	0.34	170		
$CMC_{0.42,\ low\ MW}$	0.42	210		
$CMC_{0.47,\ low\ MW}$	0.47	310		
$CMC_{0.51,\ low\ MW}$	0.51	320		
$CMC_{0.55,\ low\ MW}$	0.55	---		
$CMC_{0.58,\ low\ MW}$	0.58	---	< 25	2000
$CMC_{0.67,\ low\ MW}$	0.67	350		
$CMC_{0.75,\ low\ MW}$	0.75	360		
$CMC_{0.85,\ low\ MW}$	0.85	360		
$CMC_{0.95,\ low\ MW}$	0.95	340		
$CMC_{1.23,\ low\ MW}$	1.23	370		
$CMC_{0.5,\ high\ MW}$	0.5	450	---	
$CMC_{0.7,\ high\ MW}$	0.7	500	---	20000
$CMC_{0.9,\ high\ MW}$	0.9	630	---	
Gel_{10}	0.7	320	10	
Gel_{60}	0.7	320	60	2000
Gel_{100}	0.7	320	100	
Gel_{250}	0.7	320	250	

[a)] Determined via visual assessment of a 25 cm^2 wet film. [190]

[b)] Viscosity of an aqueous 2-wt.% NaCMC-solution

To increase comparability all coatings were calendared to a density of 1.1 g cm^{-3} equalling a porosity of 50 %. (GKL200, Saueressig, Germany). For the investigations of the influence of gel particle content a new batch of copper foil was used. During roll-to-roll coating it was possible to additionally add a corona treatment for the copper foil. The corona treatment applied had 500 W of power to treat the copper foil, resulting in 0.24 W min cm^{-2} or 14.4 J cm^{-2}. To transform the introduced power into Watt density *E*, following equation was used:

$$E = \frac{W}{b \cdot v \cdot N} \tag{4.1}$$

With *W* being the total power output, *b* the corona electrode width, *v* the line speed in m min^{-1}, and *N* the total number of treat sides.

4.3 Surface Free Energy / Contact Angle

To determine the surface free energy and the contact angle of various solid and porous materials, individual samples had to be prepared. For all NaCMCs, SBR and graphite the preparation of a solid non-swellable surface was possible. The NaCMCs and the SBR, were coated onto a glass sample holder via doctor blade with an approximate thickness of the dried polymer sample of 20 µm. The graphite powder was pressed into a 14 mm pellet by uniaxially applying a pressure of 1 MPa. For CB it was not possible to create a dense surface. Therefore, the Washburn method was used, which requires a reference sample liquid to determine the capillary constant. The reference liquid being used was n-hexane. For every sample liquid, there were three separate measurements performed equalling three different contact angles per sample liquid. The three sample liquids used varied depending on the samples. Due to NaCMC being dissolvable in water, ethylene glycol (EG) was used as a the mainly polar solvent, with dimethyl sulfoxide (DMSO) showing both contributions and diiodomethane serving as purely dispersive reference liquid. A summary of all relevant properties for the reference solvents is given in Table 4.3.

Table 4.3: Summary of relevant reference solvent properties for contact angle measurements. [67]

Probing liquid	ρ in g mL^{-1}	η in mPa·s	γ_L	γ_L^d	γ_L^p
			in mJ m^{-2}		
n-Hexane	0.661	0.33	18.4	18.4	0.0
Water	0.998	1.00	72.8	21.8	51.0
Diiodomethane (DIM)	3.325	2.76	50.8	50.8	0.0
Dimethyl Sulfoxide (DMSO)	1.100	2.00	44.0	36.0	8.0
Ethylene glycol (EG)	1.109	21.81	48.0	29.0	19.0

4.4 Electrode properties

Different electrode properties were determined. The ones of most interest were the adhesion strength, electrical resistivity and the residual water content of the prepared electrodes.

4.4.1 Adhesion strength

Three electrode stripes of each sample with dimensions of 17 mm in width and 60 mm in length were prepared and underwent a 90 ° peel-off test. To increase comparability each sample was pressed onto an adhesive with a constant force of 0.3 MPa for ten seconds. Each individual sample was then placed in a zwickiLine Z2.5/TN (ZwickRoell, Germany), pulling the sample at 600 mm min^{-1} while moving the sample holder at the same rate to always maintain a 90 ° angle. The average force needed, excluding the first and last ten mm, throughout the sample length is the adhesion force and was considered to represent the adhesion strength of each electrode sample. [191]

4.4.2 Electrical resistance

Various electrical resistance properties were directly determined via the DC 4-terminal method of the RM2610 (Electrode Resistance Measurement System, HIOKI, Japan). The aforementioned method allowed for the determination of the volume resistivity, surface resistance, and interfacial resistance in parallel. The volume resistivity is the specific bulk resistance of the electrode, excluding the current collector, and the interfacial resistance equalling the electrical resistance in between the electrode and the current collector. To determine statistics, measurements were repeated multiple times with the locations of the measurements selected at random.

4.4.3 Residual water content determined via Karl-Fischer-Oven

The Karl-Fischer titration, via the Karl-Fischer oven, was used to determine the residual water content of sample electrodes by the coulometric technique. To prevent possible water contamination, the work was conducted in a dry room with a dew point of -60 °C. Additionally, the carrier gas used in the measurement was dried via a molecular sieve before introduction to the titration setup (see Figure 3.3 in methods). Finally, the sample vials were heated for 16 hours under vacuum at 130 °C to reduce the possibility of residual water. Sample electrodes were prepared as if used in a pouch cell, i.e. they were dried for 16 hours at 130 °C under vacuum conditions. The dried electrode sheets were cut into 30 mm wide and 170 mm long samples amounting to approximately 300 mg of anode material and transferred into the vials. Finally, the sample chamber was heated to 160 °C for twelve minutes for the residual water to be extracted.

4.5 Electrochemical characterisation

4.5.1 Laboratory pouch cells

To allow for investigations regarding the industrial applications, pouch cells were built for better comparability. This was especially of interest regarding the investigations of various DS and molecular weight. The corresponding electrodes for laboratory pouch cells were dried for 16 hours under vacuum at 130 °C. Afterwards, the cells were assembled in a dry room with a dew point of – 60 °C. A commercial NMC(622) cathode with a mass loading of 12 mg cm^{-2}, which was densified to create a constant mass loading of 2.7 g cm^{-3} was used. The final area of the cathode in the pouch cell was set at 25 cm^2. To determine the capacity of the cell, the theoretical capacity of 175 mAh g^{-1} for the active material was used. The anode was overbalanced leading to a N/P ratio of 1.2. The N/P ratio refers to the relative electrode capacity of the negative (N) and positive (P) electrode in comparison to each other. In the pouch cell, the electrodes were bridged by using 500 µL EC:DMC (1:1, Vol/Vol) electrolyte with 1 M of $LiPF_6$ dissolved (LP30, SigmaAldrich, USA) while being separated by a ceramic separator (SEPARION, Degussa AG, Germany). For every electrode composition, a minimum of three pouch cells were built. To investigate the cycling behaviour, the cells were connected to a BaSyTec (CTS-LAB, BaSyTec, Germany) system and stored in a climate chamber at 20 °C. Both formation and cycling were based on the theoretical capacity of the cathode (175 mAh g^{-1}). The cycling protocol is summarised in Table 4.4. Discharge steps were using a constant current (CC) protocol, while charging steps charged to 4.2 V with CC, followed by a consecutive constant voltage (CV) step with a cut-off current of 0.05 C. Two 0.05 C steps were included every 200 cycles to investigate the reversible and irreversible capacity loss during cycling. Displayed discharge capacities regarding the DS and molecular weight are the mean average of those three pouch cells.

Table 4.4: Cycling protocol for full cell laboratory pouch cells including C-rate capability test with long-term cycling at 3C for 1000 cycles. The last three steps repeat until 1100 full cycles are completed.

Cycle Number	Discharge C-Rate [c)]	Charge C-Rate [d)]
1-2	0.05	0.05
3-12	0.5	0.5
13-52	1, 2, 3, 5 (10 cycles each)	1
53-62	1	1
63-98	3	1
99	0.05	1
100	0.05	0.05
101-1100	3	1
299, 499, 699, 899, 1099	0.05	1
300, 500, 700, 900, 1100	0.05	0.05

[c)] Discharge steps followed a constant current (CC) protocol.

[d)] Charge steps had a CC CV protocol, cut-off current of 0.05 C

4.5.2 Coin cells

While pouch cells show superior long-term results, the timely electrochemical investigation of samples necessitates the use of cell formats available more quickly. Investigations regarding the gel particle content and influence on the cell performance were built in coin cells. While the same NMC(622) cathodes and the same N/P ratio were used, the preparation slightly differed. For one, the cathode area in the final coin cell is reduced to 1.13 cm^2. Additionally, secondary drying of all electrodes equalled 16 hours under vacuum at 120 °C, before they were flushed with nitrogen gas and transferred into a glove box (200B, M.Braun Inertgas-Systeme GmbH, Germany) filled with argon gas (H_2O: <0.1 ppm, O_2: <0.1 ppm). In the coin cells, the electrodes were separated by a glass fibre separator (Whatman GF/C, SigmaAldrich, USA) while again using LP30 as electrolyte but at a higher ratio of electrolyte per active material of 200 µL per coin cell. The formation and cycling protocols were again aligned with the active material's theoretical capacity of 175 mAh g^{-1}. The discharge rate capability test mirrored that of the pouch cells in Table 4.4, while the C-rate capability test was extended with a 10C step. Additionally, the long-term tests were limited to 200 cycles, with a 3C CC discharge and a 1C CC CV charge. The cut-off current for the CV step again was set to 0.05 C. To ensure comparability, three-coin cells were constructed per sample, and the discharge capacities shown represent the average of these three cells. Additionally, a charge test was conducted with a protocol after one formation cycle of (0.1 C / 0.1 C, 0.5 C / 0.5 C, 1 C / 1 C, 2 C / 1 C, 3 C / 1 C, 5 C / 1 C, 0.05 C / 0.05 C, 2 C / 1 C, CC charge / CC discharge), to further strain the anode. Secondary drying was also modified for selected samples. First drying was extended to 24 hours under vacuum at 120 °C, with an additional 24 hours vacuum under ambient atmosphere. The second modification was reducing secondary drying to 0 hours and directly building cells.

4.5.3 Post-mortem preparation of cells

When the cycling protocol was finished, for either coin cells or laboratory pouches, the cells were reintroduced into the glove box. The cells then were opened, washed multiple times with DMC (3 x 500 µL) and stored in DMC for at least four hours. After storing in DMC, the electrodes were dried under an argon atmosphere and finally transferred to be prepared as SEM samples.

4.6 Electrolyte Degradation via NMR

NMR measurements were conducted for the previously manufactured NaCMC electrodes. To investigate the electrolyte degradation, a commercially available LFP ($LiFePO_4$, Pi-KEM, 12 mg cm^{-2}) electrode was used. Due to the stable potential plateau of LFP at approx. 3.45 V, it is inside the electrochemical stability window of carbonate-based electrolytes. [187-189] Therefore, LFP supposedly shows no significant CEI formation. [186] To ensure that the LFP cells reside in the voltage plateau they were significantly oversized, with an N/P ratio of 0.5. The secondary drying of the electrodes and assembly of the built coin cells were the same compared to the previous ones. To further reduce possible side reactions the separator was changed to a polypropylene-based separator (Celgard3501, Asahi Kasei, Japan). The amount of electrolyte was drastically reduced to 50 µL per coin cell to not dilute side reactions for the following NMR investigations.

To induce the SEI formation cells were subjected to three cycles of 0.05C of charging and 0.05 C discharging. The cells were disassembled inside a glove box after cycling was completed and only the separator was submerged in deuterated DMSO (DMSO-d_6, 99.9 atom%(D), SigmaAldrich, USA) for 15 minutes. The solution was transferred to an airtight NMR tube fitted with a Young's tap to seal off the sample. Every separate batch of DMSO was measured individually to ensure which side products resided from the solvent and which from the degradation. One dimensional ^{1}H, $^{19}F\{^{1}H\}$, and $^{31}P\{^{1}H\}$ solution NMR spectra were conducted on an Avance III HD 9.6 T (ω_{1H} = 400 MHz, Bruker, Germany) using a Smart probe. ^{1}H spectra were internally referenced to the DMSO-d_6 2.50 ppm ($\delta^{1}H$). ^{19}F and ^{31}P both were internally referenced to the electrolyte salt in LP30, which is $LiPF_6$ at -74.5 ppm ($\delta^{19}F$) and -145 ppm ($\delta^{31}P$) respectively.

4.7 SEM / EDS

Scanning electron microscopy (SEM) was conducted at an acceleration voltage of 2 kV using a Gemini system (Carl Zeiss, Germany). Elemental analysis was performed via energy-dispersive spectroscopy (EDS) with an Ultim Extreme Detector (Oxford Instruments, United Kingdom) at 4 kV acceleration voltage. The cross sections of electrode samples were prepared using broad ion beam milling with a TIC3X (Leica Microsystems, Germany).

4.8 Colouring of NaCMC

To detect the NaCMC different staining agents were used to selectively react with different active sites in the polymer. Different staining agents were used to enhance the visibility of the NaCMC in the EDS. The three different staining agents were Potassium hexahydroxoantimonate(V) ($KSb(OH)_6$, SigmaAldrich, USA), the Lucas Reagent, which is zinc chloride ($ZnCl_2$, SigmaAldrich, USA) in concentrated hydrochloric acid (37 wt.-% solution in water, ThermoScientific, Germany), and (Heptadecafluorodecyl)-trimethoxysilane (HDF-TMS, ABCR, Germany).

4.8.1 Potassium hexahydroxoantimonate(V) for sodium ions

A 2 wt.-% $KSb(OH)_6$ solution was made by adding 1 g of $KSb(OH)_6$ into 50 mL of deionised water. The $KSb(OH)_6$ was dissolved after adding 0.5 mL of 1 M KOH and stirring at an elevated temperature of 70 °C for 12 hours. The agent then was applied either by adding it to a NaCMC solution or by applying 50 µL of the $KSb(OH)_6$ solution onto the dried electrode. The size of the sample equalling a 12 mm circular electrode. $KSb(OH)_6$ is a known detection agent for sodium ions, with the schematic reaction shown in Figure 4.1.

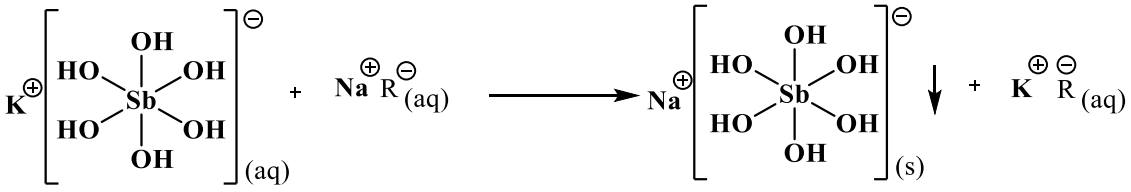

Figure 4.1: Schematic reaction of $KSb(OH)_6$ with sodium ions of another undisclosed residue.

Afterwards, the electrode was washed with deionised water to get rid of excessive staining agent. After the washing step was completed, the dried electrode was prepared as a SEM sample.

4.8.2 Lucas Reagent (Zinc chloride in concentrated HCl) for alcohols

A solution of $ZnCl_2$ (SigmaAldrich, USA) in conc. HCl (conc. HCl, 37wt.-% solution in water, ThermoScientific, Germany) was prepared by continuously adding the $ZnCl_2$ to the HCl. The solution then was applied either by adding the Lucas reagent to a NaCMC solution or by applying 70 µL of the solution onto the dried electrode. The Lucas agent is known to react with secondary alcohols by substituting the hydroxy group with chlorine, as shown for NaCMC in Figure 4.2.

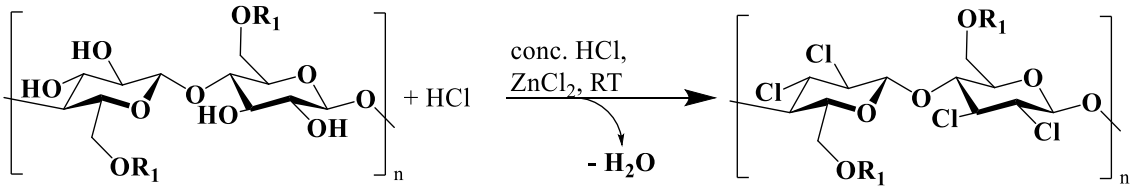

Figure 4.2: Schematic reaction Lucas reagent with secondary alcohols of NaCMC, R_1 is being used as the carboxy methyl moieties of the NaCMC.

Afterwards, the electrode was washed with deionised water to get rid of excessive staining agent. After the washing step was completed, the dried electrode was prepared as a SEM sample and investigated via EDS.

4.8.3 (Heptadecafluorodecyl)-trimethoxysilane for carboxylates

(Heptadecafluorodecyl)-trimethoxysilane (HDF-TMS) is a liquid and thereby only had to be diluted with ethanol (absolute, VWR, USA) to create a 0.2 % (Vol/Vol) solution. To activate the HDF-TMS as a staining agent, it needs to hydrolyse with water to create its active species, illustrated in the following reaction scheme, see Figure 4.3.

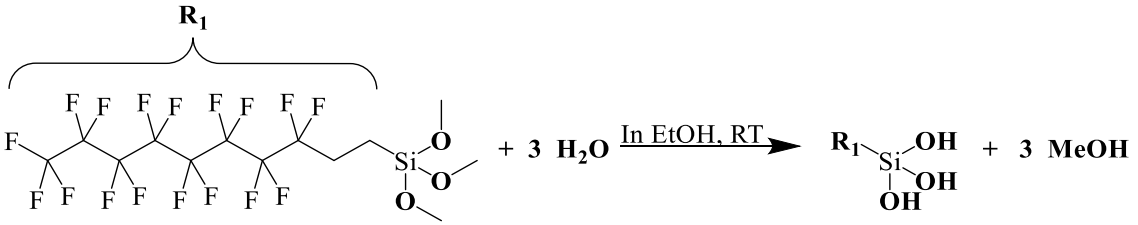

Figure 4.3: Activation of the HDF-TMS via hydrolysation with water. Ethanol and Methanol are abbreviated with EtOH and MeOH (reproduced from Keim et al. [192]).

Therefore, for a successful hydrolysation, the same amount of water was added, volume-wise compared to HDF-TMS. Using 1 cm^2 electrode equalled 0.98 mL of ethanol, with 20 µL of HDF-TMS, resulting in 20 µL of water being used for the activation. The dried anode then was

submerged in the solution and stored at 60 °C for varying periods of time for the condensation reaction of the silane with the cellulose binder to take place. Finally, the electrode was taken out of the staining agent and submerged in ethanol for a minimum of two hours. After storing it in ethanol, the sample was washed multiple times with ethanol to extract any excess staining agent. The sample then was dried at room temperature under atmospheric conditions and then prepared as a SEM sample. Investigations of the storing duration included increasing the storing time from four to eight, 16, and 60 hours. Additionally, the reaction mechanism was investigated by using three different anodes containing NaCMCs with different DS.

5 Results and Discussion

This chapter presents the results and discusses key findings related to the role of NaCMC in influencing the electrodes, which is published in parts. [106,157,192] NaCMC has been investigated as a dispersion and processing additive and is already used in industry for a multitude of years. While some key figures like the degree of substitution (DS) and molecular weight (MW) are known, there is yet systematic investigation to be performed for a broad spectrum of polymer properties to address which property influences the electrodes and how. This chapter therefore focuses on NaCMCs' interactions with other electrode components and the resulting impact on the cell performance.

The first section focuses on the interaction of NaCMC with electrode components, investigating how changes in the NaCMC influence the characteristics of the electrode. The impact of these interactions is explored in detail based on surface free energy (SFE) measurements, and the resulting calculation of the free energy of adhesion, for systems submerged in a liquid. The discussion reviews these findings to the corresponding electrode properties, such as adhesion, and electrical resistance investigating how NaCMC impacts the electrode overall. To end the first section, some boundaries of the SFE method are presented to allow for the proper understanding of the chances and limitations this approach presents. The second part of the chapter shifts focus to cell performance, where the influence of NaCMC properties, specifically DS, and MW is evaluated. Furthermore, the presence of gel particle impurities in NaCMC is analysed, revealing how these residuals impact cell efficiency and stability, potentially leading to changes in the cell performance. The final section addresses the development of a method to selectively stain NaCMC, providing a novel approach for visualising its distribution within the electrode. The main focus of the final chapter is on the methods development and understanding what challenges to overcome to selectively stain NaCMC.

Together, these results provide a complete view of NaCMCs role in LIB electrodes, highlighting the importance of tailoring binder properties to achieve optimal performance. Through detailed analysis and novel methods, this chapter offers contributions to the understanding and optimisation of key NaCMC properties to ensure the highest cell performance, by understanding the NaCMCs influence on electrodes.

5.1 NaCMC Interaction with Electrode Components

5.1.1 Investigations of NaCMC with SFE

5.1.1.1 NaCMC interaction with other electrode components

One of the key factors that influence the performance of electrodes is the interaction between all the electrode materials. Understanding the properties and impact of electrode components is therefore critical. One key figure is the SFE, a measure of the energy required to create a new surface, which can be used to understand the interaction between the electrode components. [157] A strong affinity between components, often achieved through surface energy compatibility, ensures a uniform distribution within the electrode. For instance, when a material and binder exhibit complementary surface energies, the binder is more likely to interact with the active material, forming a stable interface. Hence, mismatched surface energies lead to poor binder coverage, and weak interfacial bonding leading to worse electrical resistance and adhesion.

The total SFE energies, as well as the polar contribution of NaCMCs with different DS for low molecular weight, graphite, CB, and SBR, two batches of copper foil, CC and CC_{New} and copper foil after corona treatment, $CC_{New,500W}$, are illustrated in Figure 5.1. Corresponding contact angles and the detailed SFE contributions are catalogued in Appendix A 1.

The results for the active materials and the copper collector show a high dispersive contribution and a small polar contribution to the SFE. Graphite and CB are both carbon-based. The differences in polarity could be attributed to the various number of surface reactions taking place. CB has a higher specific surface area in comparison to graphite, allowing for more side reactions in atmospheric conditions with especially oxygen. This increases the number of polar groups on the surface, and explain the increased polar contribution. When focussing on the two different copper foil batches CC and CC_{New} it becomes apparent, that changing the copper foil batch impacts the surface properties significantly. The CC being exposed to atmospheric conditions and oxygen for an extended period of time, result in the higher polar contribution of 1.2 mJ m^{-2} for CC in comparison to 0.1 mJ m^{-2} for CC_{New}. While atmospheric conditions could be a possible explanation, other factors like a change in the used alloy metals for the current collector, or different amount of residual rolling oil from manufacturing could also impact the SFE. By applying the corona treatment to the copper foil, the generated ozone should clean the surface of any organic residue while also creating new polar groups on the surface, correlating with the SFE results. $CC_{New,500W}$ experienced a Watt density of 0.24 W min cm^{-2} or 14.4 J cm^{-2} before being measured via sessile drop method, leading to a drastic increase of the polar SFE contribution to 8.2 mJ m^{-2}. By applying corona treatment, the SFE therefore can be adjusted by changing the polar distribution through an increase in polar groups on the surface of the related current collector foil.

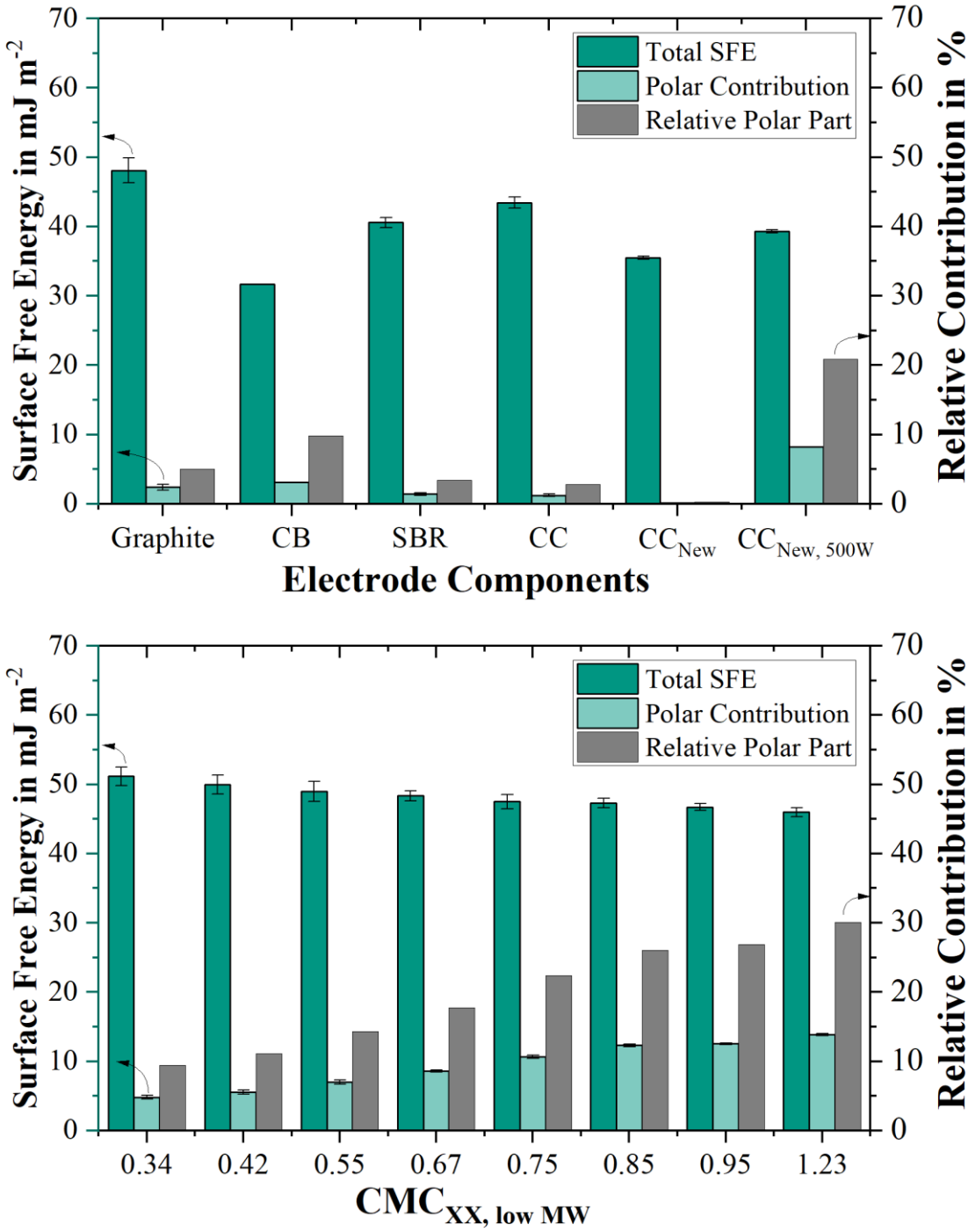

Figure 5.1: Total SFE and polar contribution for electrode components (top) and a variety of low molecular weight NaCMCs (bottom). The abbreviation for the NaCMCs is shown, with XX functioning as a place holder for the corresponding DS on the x-axis. The relative polar contribution is depicted as well, with a separate y-axis.

$CMC_{0.34,\ low\ MW}$ shows a polar contribution of 4.8 mJ m^{-2} equalling a relative polarity of 9.4 %, while having the highest total SFE with 51.1 mJ m^{-2}. The polar contribution steadily increases for

a higher DS, resulting in the highest polar contribution for $CMC_{1.23,\ low\ MW}$ with 13.8 mJ m^{-2}. The results for NaCMC show that there is a significant dependency of the polar contribution based on the absolute amount of carboxymethyl moieties in the NaCMC. The different components each are evaluated concerning their SFE. To calculate the Gibbs free energy equation (2.24) is applied. Equation (2.24) allows for a better understanding of which interface is more favourable to form when the different components are submerged in water. The results of the previously shown binders with all electrode components are summarised in Table 5.1.

Table 5.1: Summary of the Gibbs free energy for interfacial interaction ΔG_{132}^{IF} for two different materials submerged in water. The electrode components in every column depict material 1, NaCMC row material 2, with all calculations approximating the system submerged in water. Most right column shows interaction of the respective NaCMC with itself.

$CMC_{XX.\ low\ MW}$	Graphite	CB	SBR	CC	NaCMC
	$\Delta G_{S-H2O-CMC}^{IF}$ in mJ m^{-2}				
0.34	-64.3 ± 1.1	-56.1 ± 0.7	-65.9 ± 1.2	-67.5 ± 1.5	-58.1 ± 0.8
0.42	-61.9 ± 1.3	-54.2 ± 0.7	-63.5 ± 1.2	-65.0 ± 1.5	-53.8 ± 0.7
0.55	-55.5 ± 0.7	-47.8 ± 0.1	-57.0 ± 0.6	-58.6 ± 0.8	-46.9 ± 0.2
0.67	-54.0 ± 1.0	-47.6 ± 0.3	-55.5 ± 0.6	-56.8 ± 1.0	-40.9 ± 0.1
0.75	-49.3 ± 0.8	-43.7 ± 0.2	-50.8 ± 0.7	-51.9 ± 0.8	-34.0 ± 0.3
0.85	-45.9 ± 0.8	-40.8 ± 0.3	-47.4 ± 0.6	-48.4 ± 0.9	-29.5 ± 0.2
0.95	-45.2 ± 0.8	-40.4 ± 0.1	-46.7 ± 0.6	-47.7 ± 0.8	-28.7 ± 0.1
1.23	-42.5 ± 0.5	-38.2 ± 0.1	-44.0 ± 0.4	-44.9 ± 0.6	-25.4 ± 0.1

It becomes apparent, that $CMC_{1.23,\ low\ MW}$ has the highest Gibbs free energy for interfacial interaction, while $CMC_{0.34,\ low\ MW}$ shows the lowest for each solid material. The lower the calculated energy, the more energy is released when forming an interface between the various materials, making the different components have higher affinities to each other. Therefore, the favoured solid of each NaCMC can be derived by arranging results from the highest $\Delta G_{S-H2O-CMC}^{IF}$ to the lowest. The order of affinity for all different NaCMCs is the same with the highest to lowest affinity being: CC > SBR > Graphite> CB. While the relative order of affinity stays the same, the absolute variation between the electrode materials shows drastic variation. When comparing the Gibbs free energy of CC, SBR, Graphite and CB for $CMC_{1.23,\ low\ MW,}$ the absolute variation of $\Delta G_{S-H2O-CMC}^{IF}$ is 6.7 mJ m^{-2} for the highest and lowest valued Gibbs free energy for interfacial interaction. This gap steadily increases when the polar contribution in the corresponding NaCMCs decreases, as it rises to 9.2 mJ m^{-2} for $CMC_{0.67,\ low\ MW}$ and reaches its biggest difference for $CMC_{0.34,\ low\ MW}$ where the variation between highest and lowest $\Delta G_{S-H2O-CMC}^{IF}$ is 11.4 mJ m^{-2}.

This consequently leads to the following impact on electrode properties. For the electrical conductivity or resistance of an electrode, the main materials being involved are the graphite and CB,

whereas the absolute difference of $\Delta G_{S-H2O-CMC}^{IF}$ depends on the DS of the corresponding NaCMC. For $CMC_{1.23,\ low\ MW}$ the Gibbs free energy of interfacial interaction of graphite and CB in water only varies by 4.3 mJ m^{-2}. This makes it more likely for $CMC_{1.23,\ low\ MW}$ to interact with both graphite and CB in parallel, when stirred in a slurry. When the DS decreases, this gap in $\Delta G_{S-H2O-CMC}^{IF}$ between carbonaceous materials increases further with the highest difference for $CMC_{0.34,\ low\ MW}$ with a difference of the two $\Delta G_{S-H2O-CMC}^{IF}$ of 8.2 mJ m^{-2} which is a 90 % increase. The further the energy difference increases, the less likely the NaCMC is going to interact with both the graphite and CB and is going to favour to create an interface with the graphite. The results of the SFE investigations therefore indicate, that the resistivity is going to be directly dependent on the DS of the NaCMCs. This leads to the interpretation that the higher DS has lower resistivity, because it is going to be more likely to interact with both carbons in the slurry. By creating possible interfaces with both, a proper distribution and deagglomeration of CB, while connecting with the graphite is feasible for the NaCMC. On the other hand, by decreasing the DS the NaCMCs affinity to CB is decreasing in comparison to graphite. Even more, when decreasing the DS, the interaction of the NaCMC with itself becomes more and more favourable. While for high DS systems like $CMC_{1.23,\ low\ MW}$ and $CMC_{0.95,\ low\ MW}$ the NaCMC shows higher affinity to the CB in comparison to itself with a difference of $\Delta G_{S-H2O-CMC}^{IF}$ of 12.8 mJ m^{-2} and 11.7 mJ m^{-2} respectively. This again shows, that while slightly preferring the interface with graphite, the creation of interfaces with both carbon surfaces is more likely than to itself. This difference in affinities decreases further and further with the affinities for $CMC_{0.42,\ low\ MW}$ being almost equal to itself or CB, while $CMC_{0.34,\ low\ MW}$ even shows higher preference to itself than to CB. This indicates, that more interfaces of NaCMC are going to be formed with the graphite in comparison, which should result in a worsened CB distribution and therefore increased resistance. If there is more free binder available, the binder should also migrate to the copper collector during coating, as the interface with the copper foil is more favourable than NaCMC interacting with itself or CB for low DS.

When investigating the adhesion strength, another component becomes of more relevance which is the adhesive additive SBR. There is also a difference in the Gibbs free energy of interaction depending on the DS of the NaCMC with the SBR, with the relative affinity towards the SBR constantly being very favourable. Although the NaCMC shows high affinity to the SBR independent of the DS, the SBR is added very late in the slurry process during electrode processing. While $\Delta G_{S-H2O-CMC}^{IF}$ is a thermodynamic key figure, creating interfaces between the NaCMC and SBR is kinetically hindered, due to already occupied NaCMC binder and limited mixing time. When comparing said differences, there is a similar trend noticeable, with the lowest differences being at $CMC_{1.23,\ low\ MW}$. NaCMC has already created surfaces with graphite and CB before the SBR was added, therefore the difference in $\Delta G_{S-H2O-CMC}^{IF}$ for graphite and CB are compared with SBR. For graphite and SBR, the difference is only 1.5 mJ m^{-2}, while the difference of $\Delta G_{S-H2O-CMC}^{IF}$ for SBR and CB is 5.8 mJ m^{-2}. For NaCMC which already created a surface with both CB and graphite, the increase in energy by creating a new surface is low in comparison. This low drive in creating a new surface indicates, that high DS NaCMC creates some interfaces with the SBR, while the difference in $\Delta G_{S-H2O-CMC}^{IF}$ is not increasing drastically. When lowering the DS, the difference in $\Delta G_{S-H2O-CMC}^{IF}$ when comparing graphite and SBR is almost constant and is the highest for $CMC_{0.34,\ low\ MW}$ with 1.5 mJ m^{-2}. By staying almost constant, the difference between SBR and CB therefore increases steadily when decreasing the DS. The difference between CB and SBR reaches its highest value for $CMC_{0.34,\ low\ MW}$ with 9.8 mJ m^{-2}. This equals a 69 % increase

in absolute Gibbs free energy of interaction and a significant increase of affinity towards SBR in comparison to CB. The change in affinity indicates that in the same time span, a higher amount of NaCMC could create interfaces with SBR as it is significantly more favourable in comparison to CB. Additionally, due to the low DS NaCMCs even favouring interfaces with itself, it could be possible, that less NaCMC is permanently adhering to CB and therefore more binder is available to create the interfaces with SBR. With respect to the high DS NaCMCs, a decrease in DS should foster an increase in adhesion strength facilitated by better interaction of the co-binder NaCMC with the SBR and because the interface creation between NaCMC and CB is less favoured than for high DS NaCMCs.

5.1.1.2 NaCMC interaction with water

By applying equation (2.23) it becomes possible to evaluate the hydrophilicity of the various binders through calculating $\Delta G^{IF}_{CMC-H2O}$. The results for the calculations for the different NaCMCs depicted in Table 5.1 are illustrated in Figure 5.2. Please note the inverse y-axis.

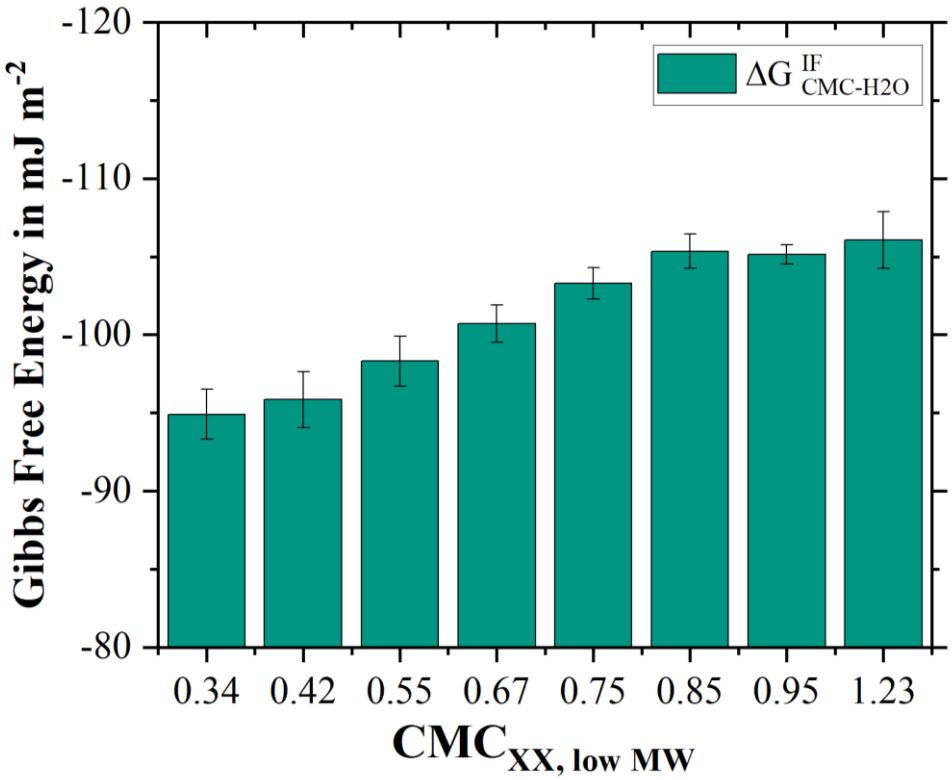

Figure 5.2: Results for the calculation of the direct interaction of water for NaCMCs with different DS. The abbreviation for the NaCMCs is shown, with XX functioning as a place holder for the corresponding DS on the x-axis. Note the inverted scale on the y-axis.

This allows to only consider the interaction of the different binders with water. If the solvent water, and the binder exhibit more complementary surface energies $\Delta G^{IF}_{CMC-H2O}$ is going to be more negative, indicating a higher hydrophilicity. The interpretation of the result is more straightforward. $CMC_{0.34,\ low\ MW}$ has the least hydrophilicity and least complementary SFE in comparison

to water, leading to a $\Delta G^{IF}_{CMC-H2O}$ of -94.9 mJ m^{-2}. Conversely, the lowest $\Delta G^{IF}_{CMC-H2O}$ and therefore highest hydrophilicity is calculated for CMC$_{1.23,\ low\ MW}$. As suggested by literature, by increasing the amount of the carboxymethyl moieties, the hydrophilicity increases. [16,193,194] Translating this into electrodes, it indicates a higher affinity to water for the NaCMCs. This implicates, that when the same amount of energy is used per NaCMC during drying, that the highest DS has more residual water left. If the NaCMC or electrode experience a surplus of energy during drying, it could lead to levelled water retention.

5.1.1.3 Resistance and adhesion strength

Important properties for electrodes are for one the electrical resistance of the electrode, and the mechanical stability. Figure 5.3 depicts the volume resistivity (green) and the interfacial resistance (grey) for all low molecular weight NaCMC with different DS.

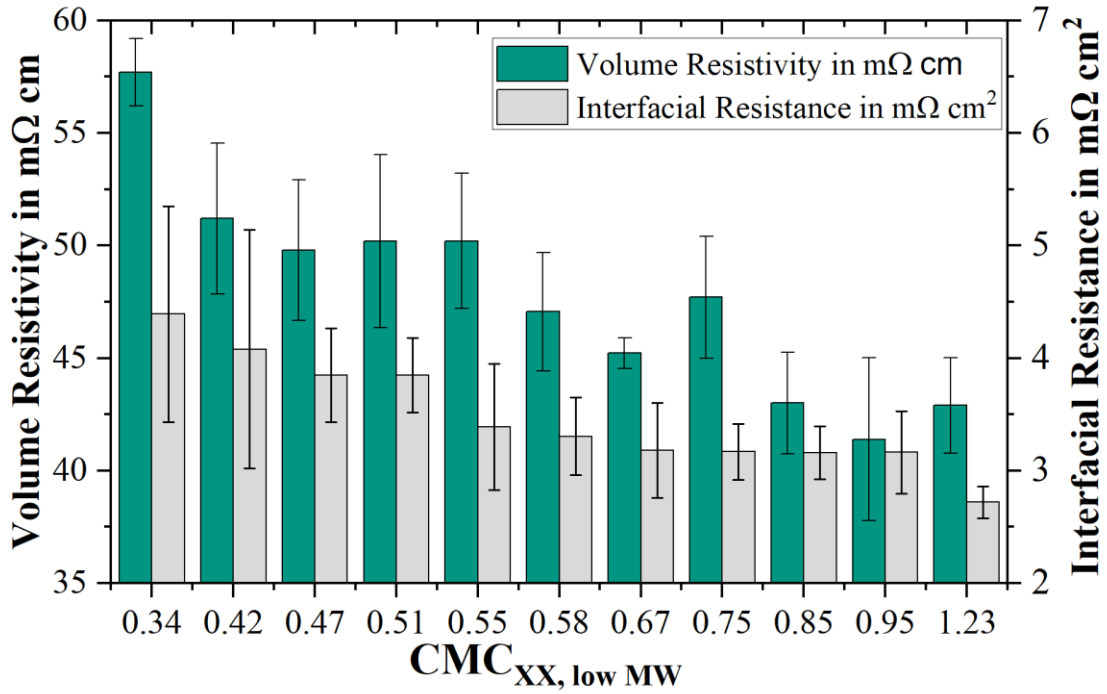

Figure 5.3: Summary of the resistance measurements including the volume resistivity and interfacial resistance for electrodes using different NaCMCs with different DS. The abbreviation for the NaCMCs is shown, with XX functioning as a place holder for the corresponding DS on the x-axis. Note the different scales on the two y-axes.

The NaCMC with the lowest DS CMC$_{0.34,\ low\ MW}$ shows both the highest volume resistivity with 57.7 ± 1.5 mΩ cm and the highest interfacial resistance with 4.4 ± 1.0 mΩ cm^2. By increasing the DS, the volume resistivity and interfacial resistance steadily decrease and reach values of 42.9 ± 2.2 mΩ cm and 2.7 ± 0.2 mΩ cm^2 for CMC$_{1.23,\ low\ MW}$, respectively. As previously stated, mechanical strength of the electrode, and therefore the adhesion strength is another crucial key figure. The results for the investigations of the adhesive properties of the electrodes for low molecular weight NaCMC with different DS are summarised in Figure 5.4.

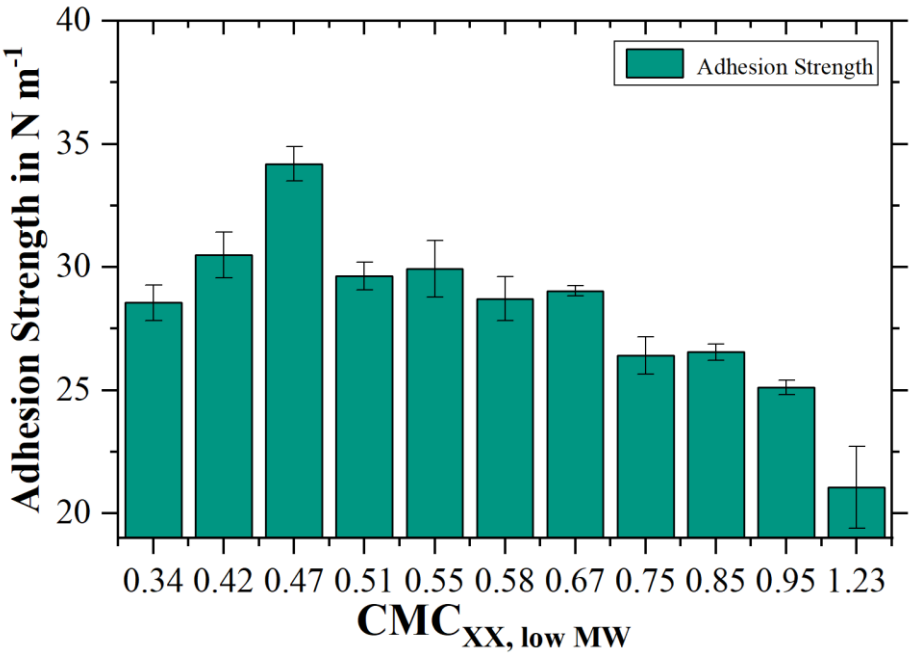

Figure 5.4: Summary of the adhesion results for electrodes using different NaCMCs with different DS. The abbreviation for the NaCMCs is shown, with XX functioning as a place holder for the corresponding DS on the x-axis. Note the different scales on the two y-axes.

The mechanical properties regarding the adhesive strength are the lowest for $CMC_{1.23,\ low\ MW}$ with a total of 21.1 ± 1.7 N m^{-1}. When decreasing the DS, the adhesive strength slightly increases and almost plateaus between $CMC_{0.67,\ low\ MW}$ and $CMC_{0.51,\ low\ MW}$. The adhesive strength then peaks for $CMC_{0.47,\ low\ MW}$ creating a maximum of 34. ± 0.7 N m^{-1}. A further decrease in DS, decreases the adhesive strength with $CMC_{0.42,\ low\ MW}$ showing only 30.5 ± 0.9 N m^{-1}, and becoming even lower with $CMC_{0.34,\ low\ MW}$ exhibiting 28.6 ± 0.7 N m^{-1} of adhesive strength.

The calculations based on the SFE for the different NaCMCs deducted, that lower DS NaCMCs should show higher volume resistivity and interface resistance based on the decrease in affinity of the NaCMC to CB, and increase of affinity to itself. For the adhesive properties, the same steady increase was suggested by the SFE results, as the affinity towards the SBR increases and more free binder should be available because the interaction of $CMC_{0.34,\ low\ MW}$ becomes more favourable with SBR than with the CB. While the interface resistance actually increases for the lower DS, the adhesive strength reaches a maximum not for $CMC_{0.34,\ low\ MW}$ but $CMC_{0.47,\ low\ MW}$. This difference in adhesion is attributed to the molecular weight of the corresponding NaCMC. Due to intermolecular interactions between NaCMC polymer chains increasing for lower DS, the corresponding molecular weight can be lower to reach the viscosity threshold in comparison to higher DS NaCMCs. [16,106] While the molecular weight stays almost constant for a DS higher than 0.5, there is a significant drop in MW for $CMC_{0.42,\ low\ MW}$ to 210 kDa and even more drastic for $CMC_{0.34,\ low\ MW}$ to 170 kDa, which is only 55 % of the MW of $CMC_{0.47,\ low\ MW}$ with 310 kDa (see Table 4.2). This reduction in the molecular weight has a significant impact on the mechanical integrity. It decreases the number of entanglements and therefore reduces the absolute number of

interlacing polymer chains. While this difference between the NaCMCs had negligible impact on the processability, it becomes apparent in the resistance and adhesion strength. Especially considering, that the interfacial resistance is higher indicating that a higher fraction of $CMC_{0.34,\ low\ MW}$ is covering the current collector without being directly connected to the carbon-binder domain (CBD). [106] The lack of entanglements leads to a decrease in interacting polymer chains and therefore reduced adhesive properties. [106]

5.1.1.4 Residual water in electrodes determined with Karl-Fischer

The water retention of graphite anodes containing different NaCMCs, after they were dried according to the cell manufacturing procedure for pouch cells, are summarised in Figure 5.5.

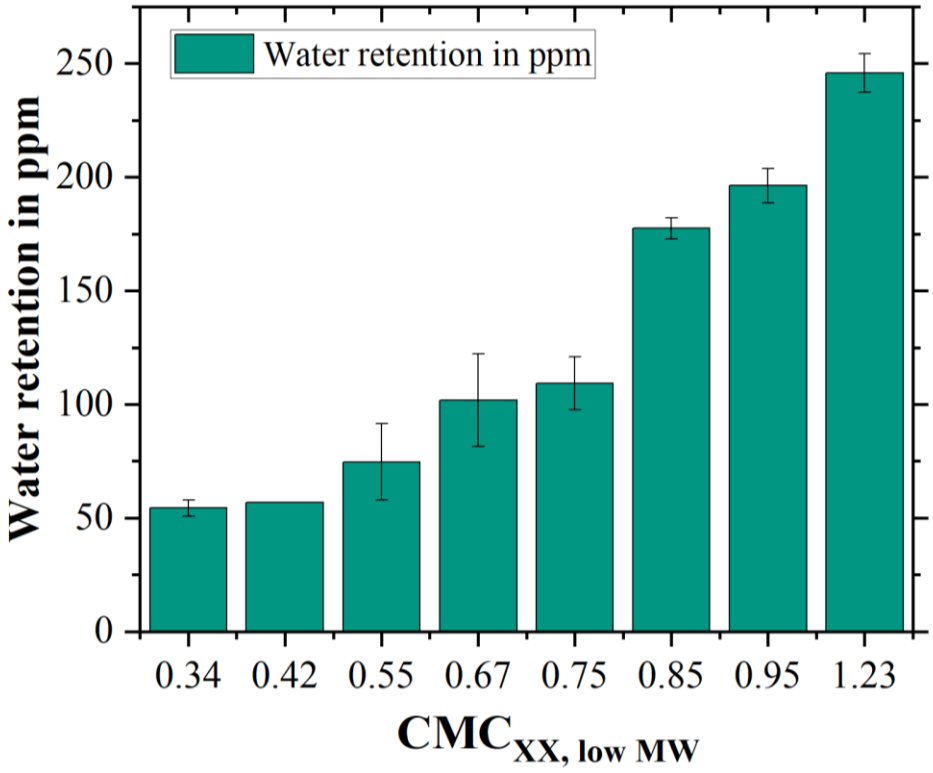

Figure 5.5: Karl-Fischer measurements for dried (130 °C for 16 hours) electrodes using NaCMCs with different DS. The abbreviation for the NaCMCs is shown, with XX functioning as a place holder for the corresponding DS on the x-axis.

Anodes containing $CMC_{0.34,\ low\ MW}$ showed the lowest amount of residual water containing only 54 ± 4 ppm(H_2O). The amount of residual water increased with the DS, leading to the highest amount of residual water for $CMC_{1.23,\ low\ MW}$ with 246 ± 9 ppm(H_2O), which was the highest DS investigated. As already postulated multiple times in various publications, the increase of the DS equals a higher hydrophilicity, supported by the calculations based on the SFE. [16,157,193,194] It further shows, that the drying duration for pouch cells leads to a variation in residual water, based on which binder is used. As water is known to have a negative impact on the battery performance, the increase in hydrophilicity could negatively impact the cell performance. The results underline that the deducted results of the SFE calculations help to understand the influences on the electrode

properties, as the deductions were in good accordance with the results observed experimentally, but limitations have to be considered in more detail.

5.1.2 Limitations of the SFE method

For the investigations of the adhesive strength, the change in molecular weight already showed some limitations for the use of the SFE method. Hence, there is the need to further investigate the limitations of the method. This includes changing selected properties of a few NaCMCs like the polymer chain length and gel particle content, see Table 4.2. Changing those polymer properties is not affecting the SFE (see Appendix A 1), as it was predominantly influenced by the DS. Furthermore, the challenge in changing more than one component and the impact on the interaction is going to be highlighted by the use of a new batch of copper current collector.

5.1.2.1 Influence of Molecular Weight on Electrode Properties

The comparison of electrical resistance and adhesion strength for high MW NaCMCs with the corresponding low MW NaCMCs is illustrated in Figure 5.6.

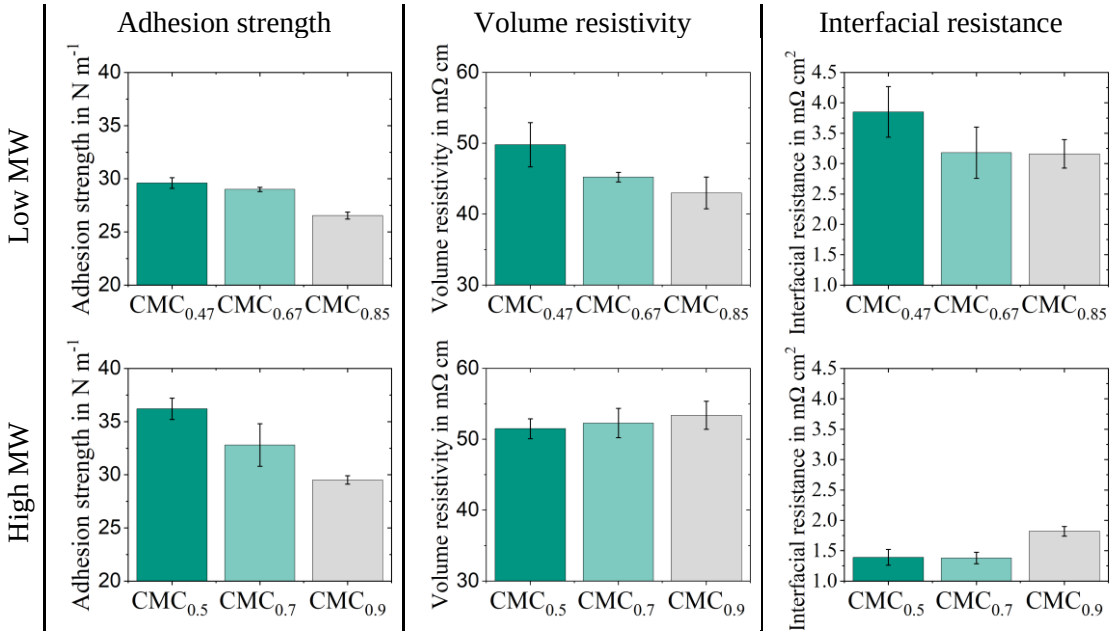

Figure 5.6: Comparison of electrical resistance and adhesion strength for NaCMCs with different molecular weights. Low molecular weights are depicted in the upper row, high MWs are depicted in the lower row. Corresponding DS of NaCMCs are colour coded and have the same colour for the high and low MWs. (Modified from Keim et al. [106])

The increase in molecular weight leads to a significant impact on the electrode properties. First off, every high molecular NaCMC, independent of the DS, shows an increase in adhesive strength. Nevertheless, the same increase in adhesion strength is noticeable when reducing the DS, showing an increase of 22 % from 29.5 N m^{-1} for $CMC_{0.9,\ high\ MW}$ to 36.2 N m^{-1} $CMC_{0.5,\ high\ MW}$. All high molecular weight NaCMCs also show a higher volume resistivity in comparison to their low MW counterpart. The increase in volume resistivity is the highest for the high DS with an increase of

almost 30 % from 41.4 Ω cm for $CMC_{0.85,\ low\ MW}$ to 53.4 Ω cm for $CMC_{0.9,\ high\ MW}$. Finally, the interfacial resistance for all high MW samples is significantly reduced in comparison to their low MW counterpart electrodes. When characterising the residual water of the electrodes, a drastic increase in the water retention for all high MW NaCMCs is apparent, see Figure 5.7.

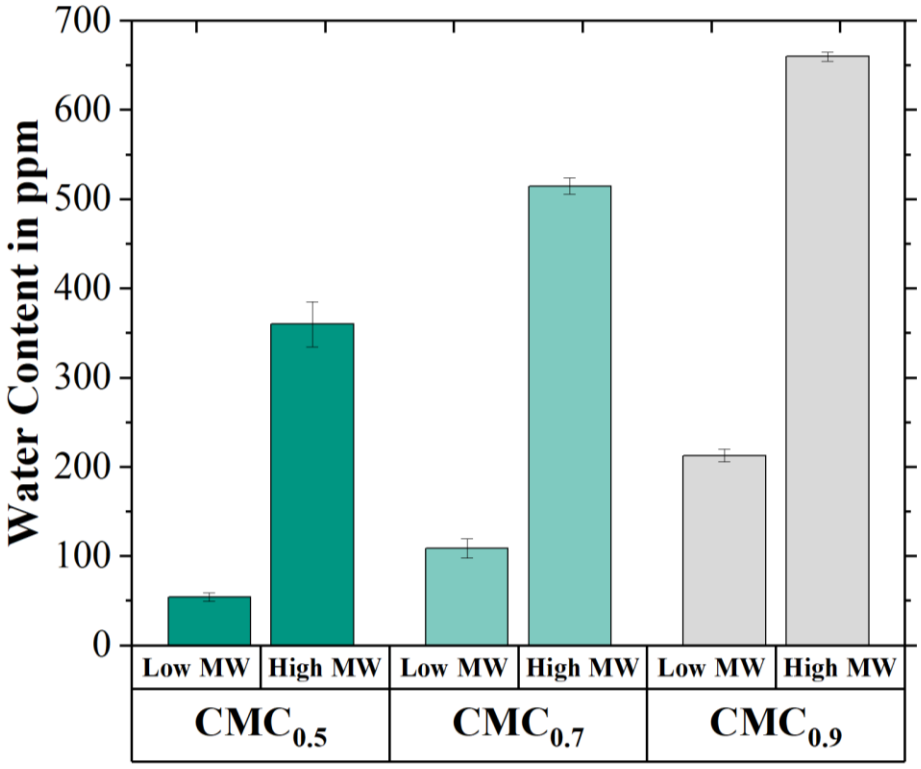

Figure 5.7: Comparison of water retention for NaCMCs with different molecular weights. For easy comparison, the DS of the NaCMCs with low MW got rounded up (Modified from Keim et al. [106]).

While again showing, that a higher DS leads to a higher water retention, all high MW NaCMC shows a minimum off 300% increase in water retention in comparison. The largest increase is observed for $CMC_{0.47,\ low\ MW}$ with 54 ppm(H_2O) increasing by 660 % to now amount to a total of 360 ppm(H_2O) for $CMC_{0.5,\ high\ MW}$. Those changes in the polymer properties led to other impact factors besides the affinity of the different NaCMCs to each component to significantly alter the electrode properties. Those changes are not properly covered or portrayed when applying the SFE method, as the surface energy for different molecular weights should stay constant and therefore the observed implications on the interactions as well. Nevertheless, due to the approximations needed to allow for the derivation of the equations, some other interactions for polymers like e.g. entanglements are neglected. Some of the trends like increasing hydrophilicity for increasing DS are still true, but other interactions have to be considered as well to explain results for a complex system like slurries.

The impact on the electrode properties observed for the high MW NaCMCs has to be attributed to other effects than changing affinities based on the SFE. The two main influences gaining more impact by increasing the molecular weight are less mobile binder, due to increased chain length

and more entanglements, which are both not considered in the SFE calculations. High molecular weight leads to lower fraction of shorter and mobile NaCMC polymer chains. As higher molecular weights are more likely to adsorb at the surface of carbonaceous materials, this leads to less free binder or polymer chains, in comparison to lower molecular weights. [195] A decrease in the fraction of short chain NaCMC also causes less accumulation of NaCMC at the current collector. As previously shown, considering SFE, the CC is a highly favourable material to interact with all NaCMCs. The short chains are less likely to interact with the carbon, and therefore improve the adhesive properties, while increasing interface resistance. [196] The increase in chain length, however, allows for more entanglements and more interactions with the carbon binder domain (CBD). Free high MW NaCMC results in an increasing number of contact points with the CC, which also interact with the CBD and therefore reducing the interfacial resistance. This is also in agreement with the adhesion results, where the active material for all high MWs better adheres to the CC independent of their correlated low MW counterpart. Additionally, the drastic increase in water retention is also connected to the growing number of entanglements. Those entanglements lead to water being trapped in between the interacting polymer chains, which in term allows for a better water retention. [197]

5.1.2.2 Impact of changing gel particle content on electrode properties

Controlling the synthesis of the NaCMC allows for the reduction of the gel particles. The aforementioned changes in NaCMC polymer properties significantly alter the NaCMCs properties and therefore impact the electrodes. Gel particles are only considered to make up a fraction of 0.1 wt.-% or less in the NaCMC, resulting in less than 0.01 wt.-% in the electrodes. Still, the variation in gel particles evidently influences the electrode properties, with the adhesion and electrical resistance illustrated in Figure 5.8. This is despite the SFE not changing, as the gel particles are negligible in contributing to the SFE. For the investigations of the gel particles on the electrode properties, a new copper foil from a different supplier was used, with absolute values therefore not being comparable to previous results.

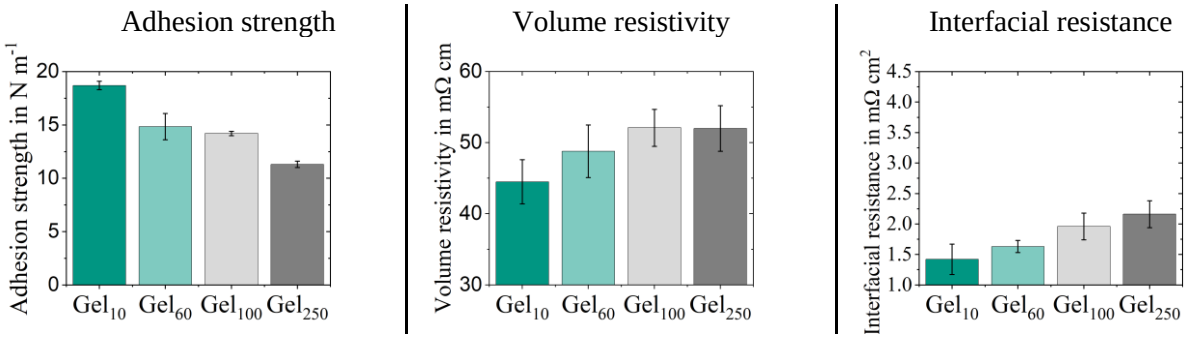

Figure 5.8: Summary of electrode properties for anodes containing different amounts of gel particles, with the DS of all NaCMCs being 0.7. (Modified from Keim et al. [106]).

Changing the copper collector to a new batch from CC to CC_{New} led to a change in the surface, and therefore influences the SFE. When comparing the adhesion of Gel_{10} to $CMC_{0.67,\ low\ MW}$, which the same polymer properties, it becomes apparent that Gel_{10} shows a significantly lower adhesion strength, which is accompanied by a decrease in interfacial resistance. Considering the results

from Table 5.1 one would deduct, that the NaCMC shows higher affinity to CC_{New} than CC. This should lead to an increase in adhesion and interfacial resistance similar to what was observed for $CMC_{0.34,\ low\ MW}$. This change does not simply only affect the interactions of the NaCMC, but also influences the interaction of all other components of the slurry with the current collector. As the SBR is mainly an additive for adhesion, the change in affinities for the latex is of more relevance. Similar to the NaCMC, which prefers CC_{New} (-62 mJ m^{-2}) over CC (-56 mJ m^{-2}), the latex shows an increase in interaction. The increase for SBR is 7 mJ m^{-2} from CC (-78 mJ m^{-2}) to CC_{New} (-85 mJ m^{-2}). While the affinity of the SBR to the CC_{New} increases in water, the adhesion strength is measured with air as surrounding medium. This change leads to an inversed affinity of the SBR, with the work of adhesion required to separate the interface for CC being higher with 83.9 mJ m^{-2} in comparison to CC_{New} with 75.2 mJ m^{-2} explaining the decrease in adhesion strength.

Reducing the amount of gel particles changes the adhesion strength and electrical resistance. Anodes containing Gel_{10} have an adhesion strength of 18.7 ± 0.4 N m^{-1} which is an 65 % increase when compared to Gel_{250} with an adhesion strength of 11.3 ± 0.3 N m^{-1}. Additionally, the electrical resistance for Gel_{10} is the lowest as well, when compared with higher gel particle contents. The volume resistivity is at 44.5 ± 3.1 mΩ cm for Gel_{10}, which is a decrease of 8 % when compared to the next lowest volume resistivity of Gel_{60} with 48.8 ± 3.3 mΩ cm . In contrast to both the investigations of the molecular weight and the DS, the increase in adhesion is not accompanied by an increase in interfacial resistance. Gel_{250} which shows the lowest adhesion strength also has the highest interfacial resistance with 2.16 ± 0.22 mΩ cm^2. The lowest interfacial tension is observed for Gel_{10} with 1.42 ± 0.25 mΩ cm^2, resulting in the most promising electrode properties considering other gel contents, as the mechanical integrity is the highest, while also presenting low electrical resistance.

While the copper collector influences the adhesion and interfacial resistance, it is also evident that the small fraction of gel particles has a significant impact on the electrode properties. The decrease in gel particles leads to a better dispersion of the CB, reasoning the lowest volume resistivity for Gel_{10}. Both the increase in adhesion and lower interfacial resistance lead to the conclusion that there are decreasing contacts between the copper collector and the active material for an increasing amount of gel particles. Due to gel particles being non-soluble but swellable impurities, they compete with the SBR rubber for adhesion on the copper foil during coating, which reduces the adhesion of the overall electrode.

The results of the absolute water residue in the electrode are summarized in Figure 5.9. These results reveal a substantial difference depending on the gel particle content within the already dried electrodes. For instance, Gel_{10} contains 73 ppm(H_2O) and is thereby in significant contrast to Gel_{250}, which contains 528 ppm(H_2O). This represents a seven-fold increase in water content as gel particle concentration increases. Therefore, the incline in impurities in NaCMC allows for higher water retention resulting in more residual water in the electrode after secondary drying and, therefore, the cell. Again, this increase in water content is not depicted by SFE, as the gel particles are only contributing a small fraction of the NaCMC and are, therefore, not influencing the contributions to the SFE of the NaCMC.

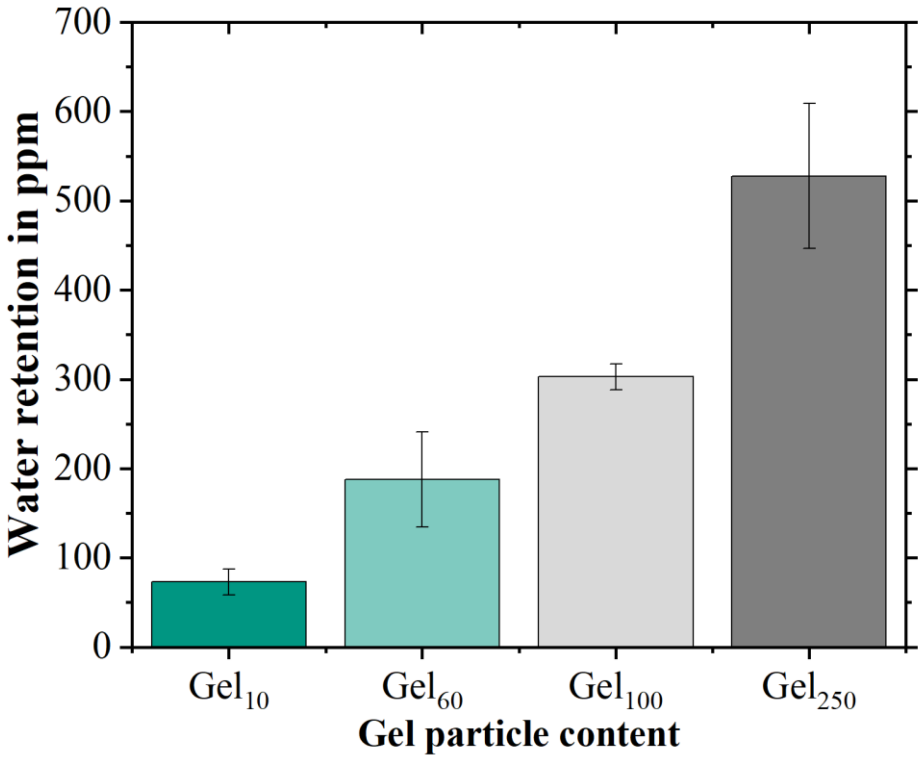

Figure 5.9: Residual water in anodes with different gel particle content after secondary drying for 16 hours at 130 °C. (Expanded from Keim et al. [106]).

To conclude, while the SFE calculations help further understand the implications of changing selected binder properties, or those of other components on electrodes, it is limited in portraying or predicting the influence of a change in material properties like molecular weight or impurities. Furthermore, the slurry is a multicomponent system, in contrast to two- or three-component system. When changing one component it has implications on every interaction in the system and not just the one maybe in focus, as demonstrated by the change in the copper collector. It can be very useful, but its limitations have to be considered when using it to correctly interpret changes in electrode properties.

5.2 Influence of NaCMC properties on Cell Performance

5.2.1 Impact of different DS

It has been found, based on SFE, that changing the DS has a drastic impact on the interactions inside slurries, leading to different electrode properties. Due to the multitude of NaCMCs used, the cell results are split. First, the rate capability tests of electrodes containing higher DS NaCMCs ranging from 0.67 up to 1.23 and low molecular weight are shown in Figure 5.10.

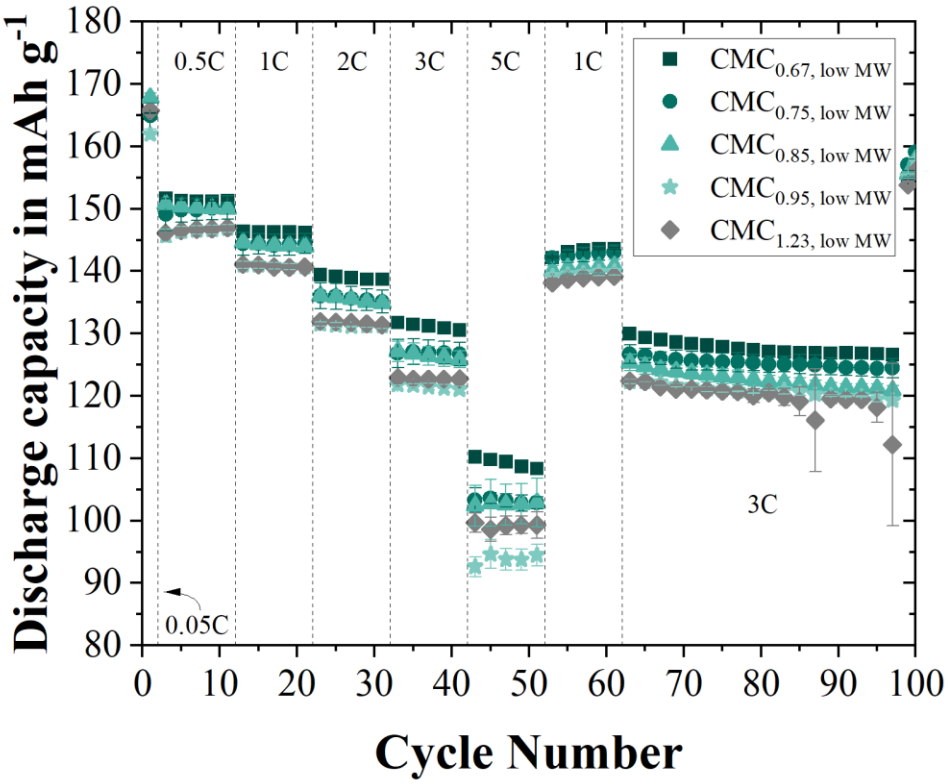

Figure 5.10: Rate capability test for electrodes containing NaCMC with low molecular weight and different DS from 0.67 to 1.23. For better visibility, only every second value is shown in the rate capability test (Modified from Keim et al. [106]).

All electrodes show similar performance, during formation. Nevertheless, electrodes containing the highest DS NaCMCs, $CMC_{1.23,\ low\ MW}$ and $CMC_{0.95,\ low\ MW}$, already show comparably lower capacities at 0.5 C. Cells containing electrodes with $CMC_{1.23,\ low\ MW}$ and $CMC_{0.95,\ low\ MW}$ provide on average 146.5 ± 0.4 mAh g^{-1} and 146.7 ± 0.3 mAh g^{-1} respectively. When compared to the highest capacities of electrodes containing $CMC_{0.67,\ low\ MW}$, which cells provide 151.3 ± 0.2 mAh g^{-1} on average for 0.5 C, this equals a 3 % decrease in capacity. This disparity further increases for higher discharging rates, when the electrodes are strained stronger.

At 5 C, electrodes containing $CMC_{1.23,\ low\ MW}$ (99.0 ± 0.3 mAh g^{-1}) and $CMC_{0.95,\ low\ MW}$ (94.1 ± 0.6 mAh g^{-1}) repeat as the two lowest capacities. $CMC_{0.67,\ low\ MW}$ is showing the best performance with 109.2 ± 0.7 mAh g^{-1}. $CMC_{0.67,\ low\ MW}$ therefore has a 10 % higher capacity in comparison to $CMC_{1.23,\ low\ MW}$ and even more than 16 % higher performance than $CMC_{0.95,\ low\ MW}$. When beginning the repeated 3 C cycling, the sequence from best to worst in regards of capacity depending on the DS is 0.67 > 0.75 > 0.85 > 0.95 > 1.23. The rate capability test reveals, that an increase in DS is accompanied by a decrease in capacity. The adjoining long-term investigations are illustrated in Figure 5.11.

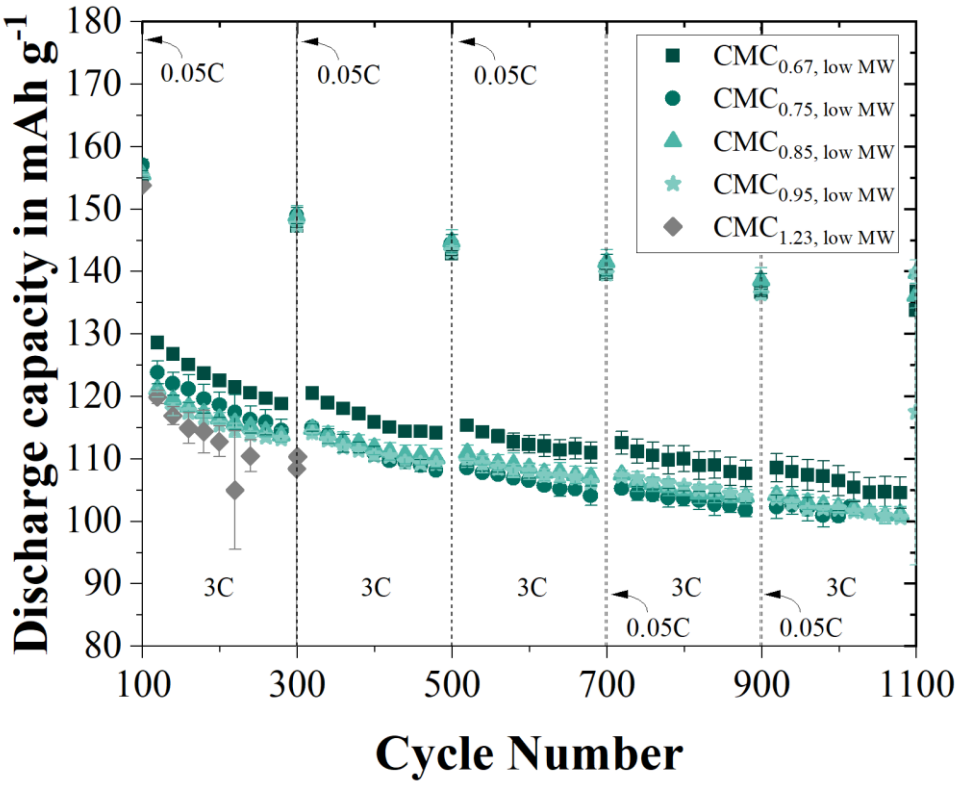

Figure 5.11: Long-term test following previous rate capability test for electrodes containing NaCMC with low molecular weight and changing the DS from 0.67 to 1.23. For better visibility, only every 20th value is shown in the long-term investigations (Modified from Keim et al. [106]).

The adjoining long-term investigations reveal, that the degradation in the beginning is higher for $CMC_{0.67,\ low\ MW}$, but levelling out, with the overall order of the cell capacity being almost equal in comparison to the rate capability test, even after 1100 cycles. Cells containing $CMC_{1.23,\ low\ MW}$ showed malfunctioning cycling behaviour. The highest cycle count for the cells was reaching 300 cycles, before showing drastic variations in capacity. $CMC_{1.23,\ low\ MW}$ cells are therefore displayed up until cycle 300. Cells with electrodes containing $CMC_{0.75,\ low\ MW}$ experienced higher degradation in comparison to electrodes containing other NaCMCs, which could be due to slightly higher volume resistivity.

When combining the results of both the rate capability test and the long-term investigations for the DS range of 0.67 up to 1.23 it becomes apparent that a decrease in DS is accompanied by an increase in discharge capacity. Both $CMC_{1.23,\ low\ MW}$ and $CMC_{0.95,\ low\ MW}$ exhibited poor rate performance and the worst absolute capacity in the long-term investigations. Anodes using $CMC_{0.85,\ low\ MW}$ and $CMC_{0.75,\ low\ MW}$ leads to further increasing performance, with anodes containing $CMC_{0.67,\ low\ MW}$ having both the best rate performance and absolute long-term capacity. This sequence in capacity is directly connected to the residual water content, in the respective electrodes. While the order for the highest capacity during the rate capability test (with exceptions of 5 C) in regards of DS is 0.67 > 0.75 > 0.85 > 0.95 > 1.23, the same is true for the residual water. The decrease in performance for higher DS is attributed to an increased water content. This increase in water retention leads to parasitic side reactions. These side reactions consume electrolyte and lithium ions, decreasing the lithium inventory in the full cell and impact the cell performance negatively. This is also in line with previous research, demonstrating that higher amounts of residual water lead to an increase in parasitic side reactions. [198-200]

The rate capability test of low DS NaCMCs ranging from 0.42 up to 0.58 is summarised in Figure 5.12. The best performing cell result containing $CMC_{0.67,\ low\ MW}$ was added as reference. For low discharging rates of 0.5 C, all electrodes independent of the DS show similar discharging capacities, being inside their respective error bars.

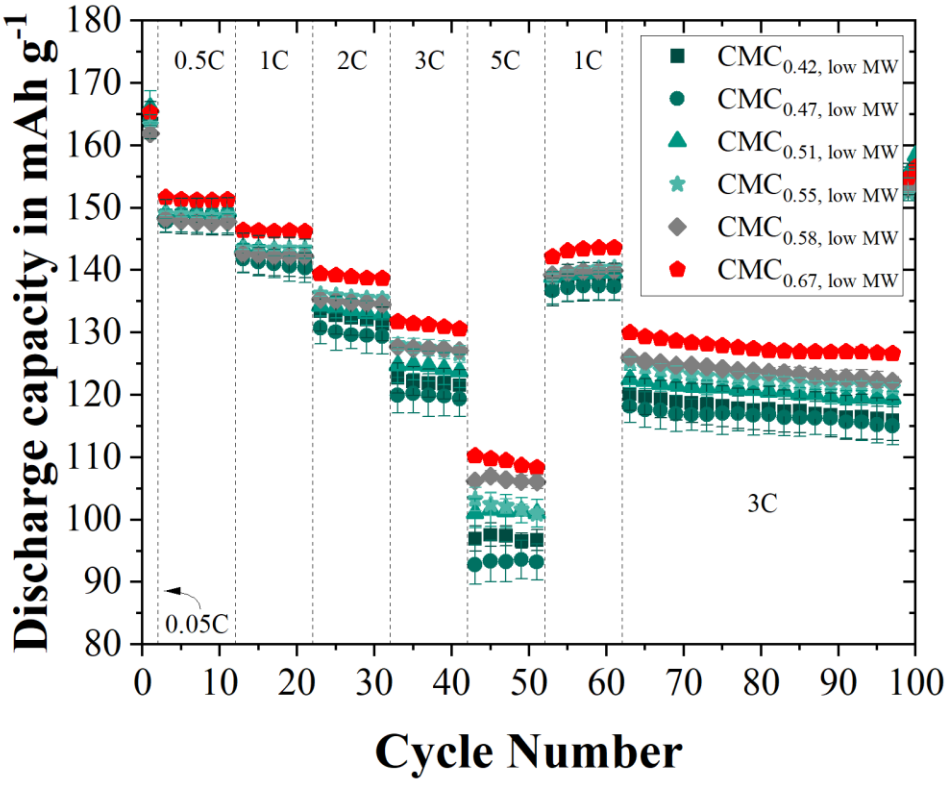

Figure 5.12: Rate capability test for electrodes containing NaCMC with low molecular weight and different DS from 0.42 to 0.67. For better visibility, only every second value is shown in the rate capability test (Modified from Keim et al. [106]).

When increasing the discharging rate, a difference between the various cells becomes apparent. At the highest discharging rate of 5 C the biggest difference is observed. $CMC_{0.47,\ low\ MW}$ has the lowest performance at 5 C only resulting in 93.3 ± 3.2 mAh g^{-1}. The highest performance is observed for electrodes containing $CMC_{0.58,\ low\ MW}$ with 106.3 ± 0.8 mAh g^{-1}. Still, $CMC_{0.58,\ low\ MW}$ shows a lower performance in comparison to the reference $CMC_{0.67,\ low\ MW}$. When the protocol reaches the repeated 3 C discharging during the rate capability test, the sequence from best to worst regarding capacity depending on the DS observed is 0.67 > 0.58 > 0.55 > 0.51 > 0.47 = 0.42.

The adjacent long-term investigations of the cells are illustrated in Figure 5.13, with $CMC_{0.67,\ low\ MW}$ again added as reference. The cells showing the highest initial capacities, namely $CMC_{0.58,\ low\ MW,}$ and $CMC_{0.55,\ low\ MW}$, show the highest capacity fade during the initial cycles. Independent of the cycle count, the highest to lowest capacity order stays the same.

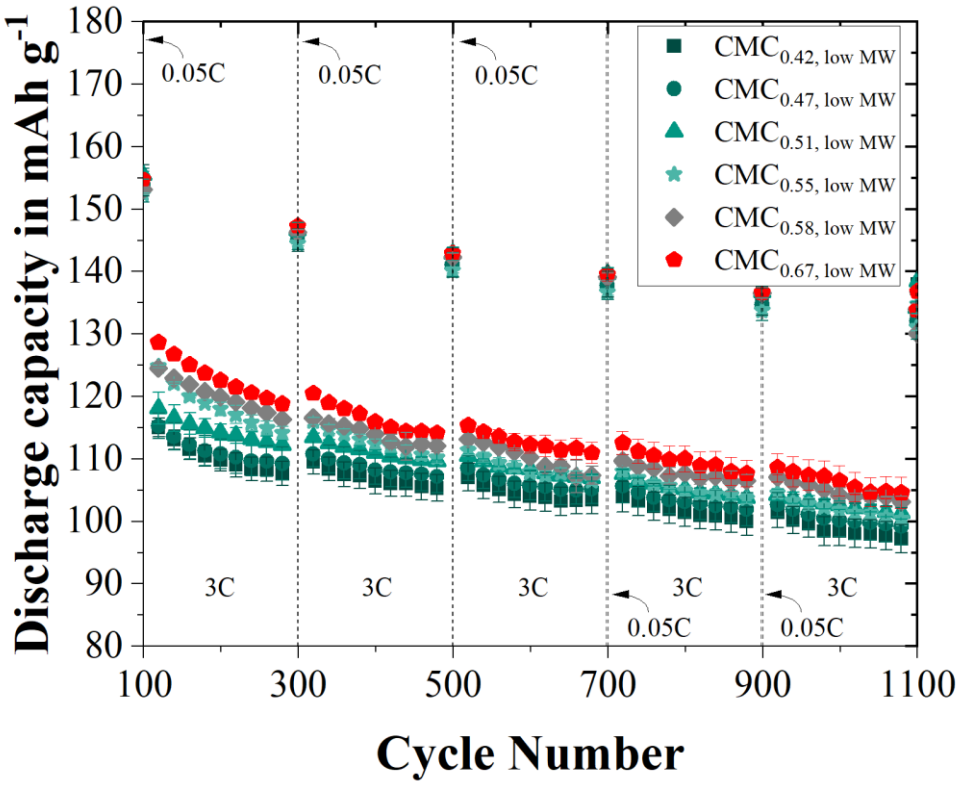

Figure 5.13: Long-term test following previous rate capability test for electrodes containing NaCMC with low molecular weight and different DS from 0.42 to 0.67. For better visibility, only every 20th value is shown in the long-term investigations (Modified from Keim et al. [106]).

Both $CMC_{0.42,\ low\ MW,}$ and $CMC_{0.47,\ low\ MW}$ show the highest relative capacity retention throughout the 1000 cycles with 82.6 % and 84.4 % respectively. Furthermore, during the 0.05 C step after 1100 cycles both $CMC_{0.42,\ low\ MW,}$ and $CMC_{0.47,\ low\ MW}$ display the highest capacity. This indicates that both $CMC_{0.42,\ low\ MW,}$ and $CMC_{0.47,\ low\ MW}$ have the highest lithium inventory left. Based on the

previous deduction, a further decrease in water retention explains the higher absolute capacity. Therefore, an increase in capacity for a DS lower than 0.67 was expected. In contrast, anodes containing NaCMCs with a lower DS displayed a similar capacity to $CMC_{0.67,\ low\ MW}$ only for 0.5 C discharging rates. When increasing the discharging rate, the different NaCMCs split up and are segregated by larger margins. The water retention, therefore, is not the only key parameter affecting the cell performance based on different NaCMCs. The other key influence on the cell performance is the electrical resistance of the cells. For NaCMCs with a DS of 0.67 to 1.23 the volume resistivity and interfacial resistance are similar, except $CMC_{0.75,\ low\ MW}$ showing a slightly higher value, see Figure 5.3. NaCMCs with a DS lower than 0.67 all show increasing volume resistivity and interfacial resistance. Therefore, the performance of the NaCMCs with a DS lower than 0.67 is increasingly more negatively impacted by their electrical resistance. This incremental growth in electrical resistance for decreasing DS leads to higher polarisation, resulting in an overall worsened cell performance. [67] The higher electrical resistance is especially apparent at high discharging rates and can be observed during the rate capability test in Figure 5.12. This is further supported by the high lithium inventory left for both $CMC_{0.42,\ low\ MW,}$ and $CMC_{0.47,\ low\ MW}$, suggesting another reason then a significantly lower lithium inventory for the lower capacity. Furthermore, it was observed that there is a sharp decline in capacity retention when the discharge rate is increased during the long-term cycling for all electrodes. This could suggest a kinetic problem, e.g. diffusion limitations, reversibly reducing the capacity retention. The resulting kinetic limitations impair the ability of the cell to sustain high-rate performance, resulting in a quick but reversible drop in capacity. As it was observed in all electrodes, said limitation was attributed to the limitations of the cathode and not related to the anode side. Finally, all different cell results of the different DS are illustrated for selected cycle numbers, see Figure 5.14. As $CMC_{1.23,\ low\ MW}$ cells were not working without malfunction after cycle 300, $CMC_{1.23,\ low\ MW}$ is only included in the graph regarding cycle 101.

Observing all different discharge capacities for the whole investigated DS range, $CMC_{0.67,\ low\ MW}$ provides the highest cell performance in every observed step. It, thereby, shows a local maximum in capacity in the investigated DS range. The results strongly suggest that electrodes containing $CMC_{0.67,\ low\ MW}$ provide the best properties for the electrodes. $CMC_{0.67,\ low\ MW}$ provides sufficient dispersion to allow for a comparable resistance similar to higher DS systems like $CMC_{0.85,\ low\ MW,}$ or $CMC_{0.95,\ low\ MW}$. Instead of detecting high amounts of water, electrodes using $CMC_{0.67,\ low\ MW}$ show less than 100 ppm(H_2O). While the water retention of lower DS systems like $CMC_{0.42,\ low\ MW}$, $CMC_{0.47,\ low\ MW,}$ and $CMC_{0.55,\ low\ MW}$ is further reduced, the cell results demonstrate the importance of the electrical resistance. $CMC_{0.67,\ low\ MW}$ provides both comparably low water retention and comparably low resistance. Considering both key properties and the cell performance, the results strongly indicate, that the SEI formation is almost not strongly negatively impacted the small amounts of water retained. Additionally, the resistance is supposedly small enough to not entail strong polarisation effects. Thus, $CMC_{0.67,\ low\ MW}$ results in the overall best anode performance, as it affects the anode performance the least in any negative way.

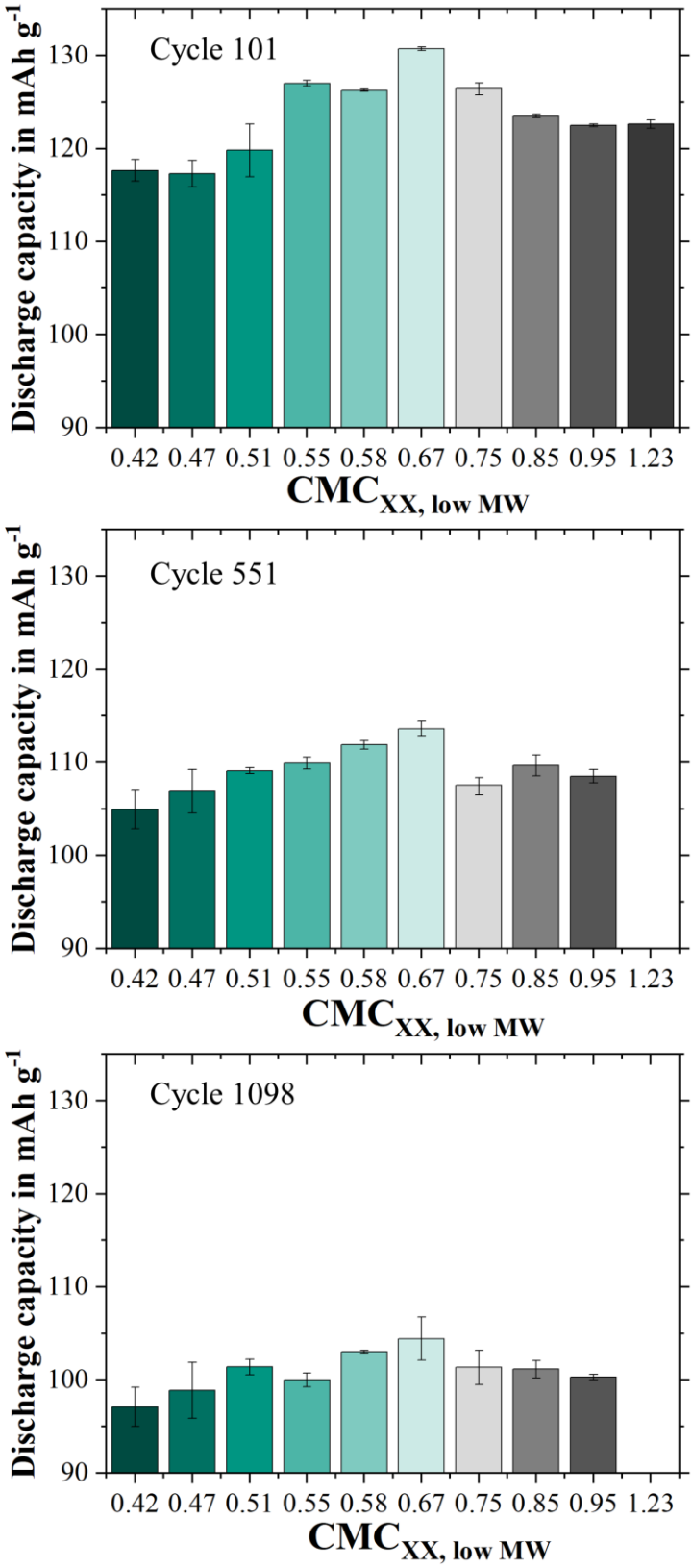

Figure 5.14: Comparison of discharge capacity for varying cycles of cells using electrodes containing different NaCMCs with different DS. The abbreviation for the NaCMCs is shown, with XX functioning as a placeholder for the corresponding DS on the x-axis.

5.2.2 Electrolyte decomposition via NMR

Changing the DS of the NaCMC leads to a significant variation in the cell performance. Whilst the impacts and the results were connected to electrode properties, which were able to be explained through the SFE, it could also be possible, that the changing DS of the NaCMC influences the degradation pathways during SEI formation. By using NMR, it allows for deeper insights into the electrolyte degradation and thereby explore, if the different DS impacts the degradation pathway of the SEI formation. The results of the ^{1}H-NMR for post-mortem electrodes containing different NaCMCs, namely $CMC_{0.42,\ low\ MW}$, $CMC_{0.67,\ low\ MW}$, and $CMC_{0.95,\ low\ MW}$, are summarised in Figure 5.15. Note, that the focus of Figure 5.15 is on the electrolyte decomposition products, which is the reason why an enhanced view of the results is shown. A detailed analysis of the individual peaks is given in Appendix A 2, as well as the impurities in the deuterated DMSO in Appendix A 3.

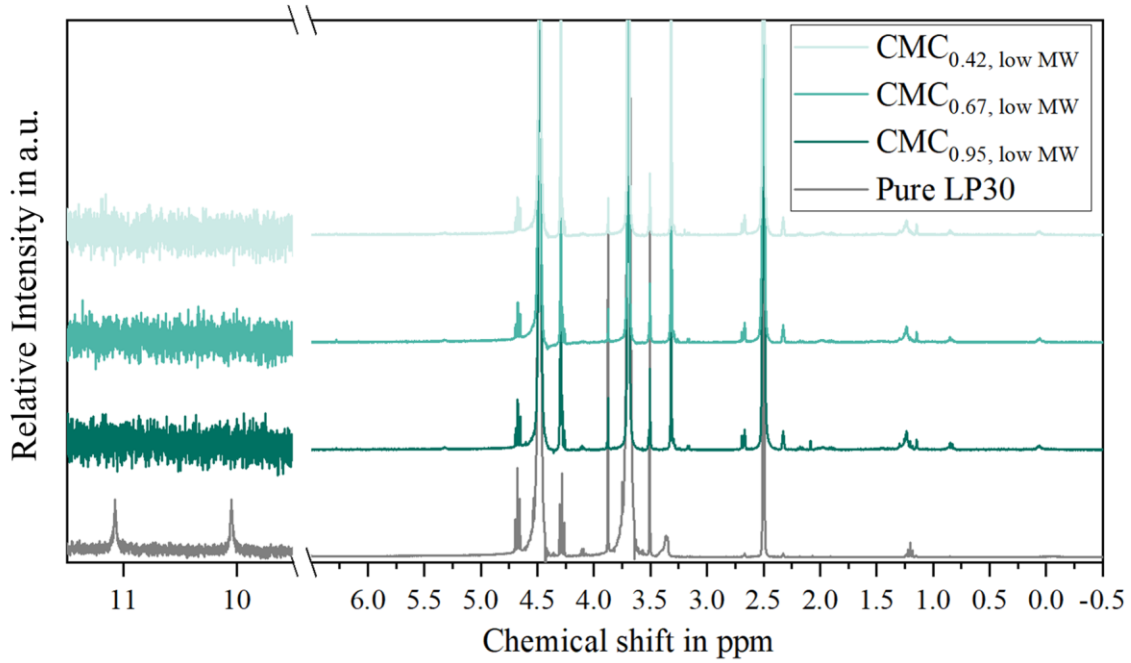

Figure 5.15: ^{1}H-NMR results for different anodes after formation with LFP and pure electrolyte LP30 as reference. To focus on the degradation products, the results were enhanced in size by 50 times, with the results for the chemical shift of 10 ppm to 11 ppm being enhanced by 500 times.

After formation, the main components of the liquid electrolyte still are considered to be EC and DMC, which are also present in the NMR most dominantly. [185,186] Hydrofluoric acid (HF), which is an impurity created during water-based electrolyte salt decomposition, is only found in the pure LP30. Traces of the HF which could impact the resulting SEI, are either already used up or not detectable. Due to the high signal-to-noise ratio of the used electrolytes, some of the traces detectable in the pure electrolyte may be overshadowed by the noise.

All samples showed various degradation products including the main degradation products of EC and DMC. The main degradation products LMC and LEDC, as well as signals for ethylene oxide

oligomers, are visible. The signals of both LMC and LEDC are most notable and pronounced in sample anodes using $CMC_{0.95,\ low\ MW}$. Despite not detecting any residual HF, this could hint at $CMC_{0.95,\ low\ MW,}$ and other high DS NaCMCs to create more of said species. An increasing amount of electrolyte degradation products suggests, that high DS NaCMCs promote the degradation of the electrolyte due to higher amounts of residual water. This is in line with the previous electrode properties, and cell results. The increase in polarity leads to a higher water retention. As described in chapter 2.3, water catalyses the degradation of electrolyte components. The cell results, which showed inferior cell performance are also attributed to the decreased performance due to the higher residual water of high DS NaCMCs.

Nevertheless, the detected electrolyte degradation products are all of the same species and show almost no differences, besides changing amounts of impurities from the used deuterated solvent d^6-DMSO. Despite the significant influence of the DS on the cell performance there is no difference in degradation products found in the liquid NMR measurements. Whilst there is no significant difference in degradation products for different DS, another difference was observed, which is highlighted in Figure 5.16. To focus on the main components of the electrolytes, an excerpt of the ^{1}H-spectra is shown.

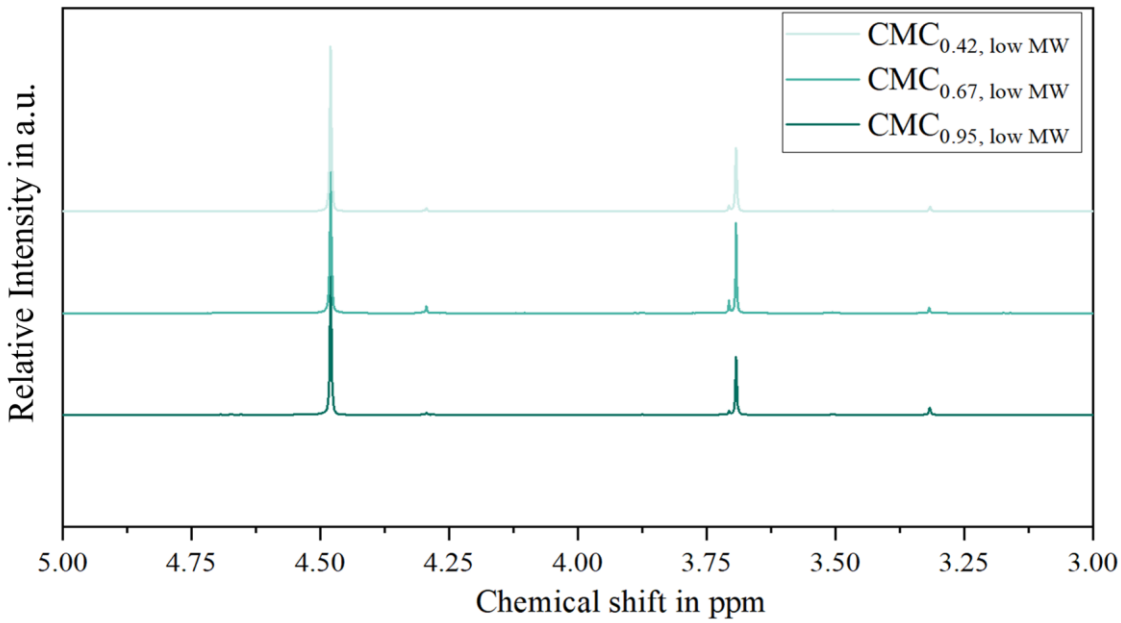

Figure 5.16: ^{1}H-NMR results for various anodes after formation with LFP. To focus on the main electrolyte components EC and DMC the results are not enhanced but an excerpt from the 3 ppm to 5 ppm chemical shift is shown.

$CMC_{0.95,\ low\ MW,}$ despite not showing a drastic difference in new degradation products, affects the peaks at 4.48 ppm which is attributed to EC and 3.69 ppm which is attributed to DMC. This is in line with the cell results and the amount of residual water, already suggesting a higher electrolyte uptake during formation, due to increased SEI formation. This increase in electrolyte degradation would indicate a thicker SEI, explaining a lesser performance of NaCMCs with increased water

retention based on their polarity. Decreasing the total amount of EC and or DMC in the electrolyte would also be accompanied by a decreasing electrolyte conductivity. Both would result in a worsened cell performance, as it negatively impacts the electrolyte.

The results for the degradation products led to the conclusion, that NaCMC is not actively influencing the degradation pathways of the SEI formation. Different degradation product species were not identified, and without using a reference, a quantitative differentiation of electrolyte degradation products is not possible. Therefore, due to not using a reference liquid to calibrate the integers, insights regarding changing peak heights have to be considered with care. Additionally, both $^{19}F\{^{1}H\}$ and $^{31}P\{^{1}H\}$ solution NMR spectra did not yield any further insights.

5.2.3 Impact of increasing MW of NaCMC on cell performance

The DS showed a significant impact on cell performance. Changing other polymer properties is also influencing electrodes, which could influence the performance of the cells. The molecular weight of the NaCMCs being one of the properties of most interest. The classification of NaCMCs, to be considered either low or high molecular weight, is dependent on the viscosity threshold of the NaCMCs used (see chapter 4.1). The results for the rate capability test and long-term cycling are illustrated in Figure 5.17. For comparison, the best performing low molecular weight NaCMC anode ($CMC_{0.67,\ low\ MW}$) is added as reference.

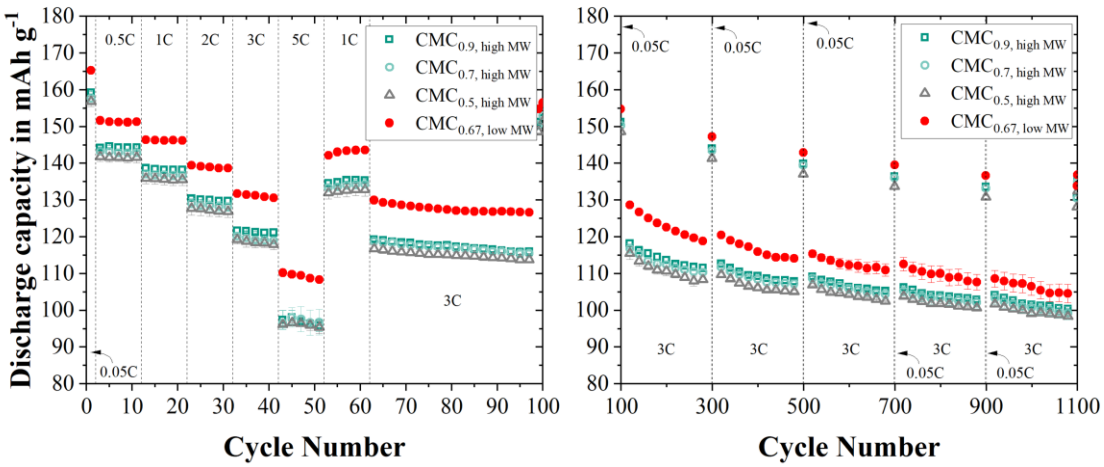

Figure 5.17: Rate capability test and long-term cycling results for electrodes containing NaCMC with high molecular weight and different DS. $CMC_{0.67,\ low\ MW}$ is added as a reference. For better visibility, only every second value is shown in the rate test and every 20th in the long-term cycling. (Modified from Keim et al. [106]).

In contrast to the low molecular weight cell performance, the results of the cells using high molecular weight NaCMCs are almost not able to be distinguished. $CMC_{0.5,\ high\ MW}$ is showing similar results to $CMC_{0.7,\ high\ MW}$ and $CMC_{0.9,\ high\ MW}$. When comparing the cell results to the added reference of $CMC_{0.67,\ low\ MW}$ it becomes apparent, that all high molecular weight NaCMCs show worse performance. This is also true when comparing the results to the respective low MW, with all low

MW NaCMCs outperforming their higher MW counterparts. This significant drop-off in performance is attributed to the increase in water retention, coupled with the increase in molecular weight. This increase leads to more parasitic side reactions decreasing the amount of available lithium ions and worsening the ionic conductivity of the electrolyte, while negatively impacting the SEI. [198-200] The benefit of decreasing the residual water for lower DS is still apparent for $CMC_{0.5,\ high\ MW}$, as shown in Figure 5.7. Although the decrease in water retention is close to 300 ppm(H_2O) there is almost no positive impact on the cell performance. It is possible, that the increase in performance is not noticeable in comparison to low molecular weight NaCMCs, as it still is significantly higher than for all low MW NaCMCs. To sum it up, despite equal volume resistivity and lowest water content in dried anodes containing $CMC_{0.5,\ high\ MW}$ for high molecular weights, the results compare to $CMC_{0.7,\ high\ MW}$ and $CMC_{0.9,\ high\ MW.}$ The negative impact of water on the cell performance overshadows the relatively lower water content in the dry electrode.

5.2.4 Influence of NaCMC impurities on cell performance

Interchanging various polymer properties of the NaCMC was shown to drastically alter the cell performance. A changing amount of gel particles unexpectedly imposed significant changes on the electrode properties. The discharging rate capability test is summarised in Figure 5.18.

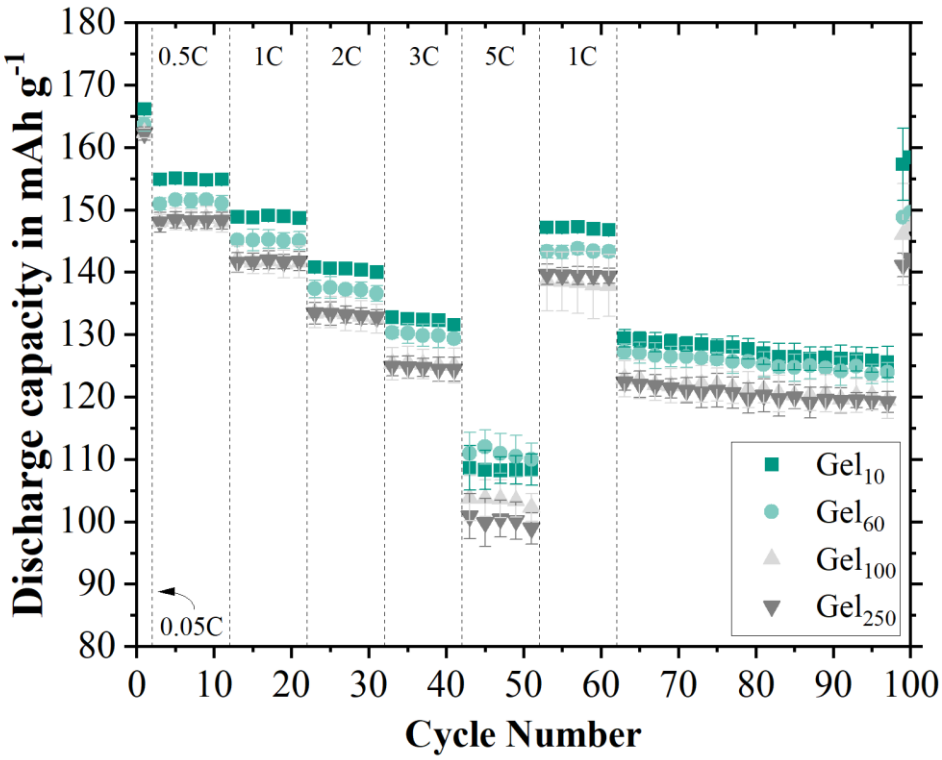

Figure 5.18: Discharge rate capability test for anodes with changing gel particle content (Modified from Keim et al. [106]). For better visibility, only every second value is shown in the rate capability test.

By comparing the various gel particle content in the electrodes, it becomes apparent that cells with anodes containing lower amounts of gel particles lead to better performance in cells. Already after formation, there is a significant difference between the different levels of gel particle content. After formation, cells containing anodes with Gel_{10} show an average discharge capacity of 155.0 ± 1.0 mAh g^{-1}, while cells containing Gel_{250} only exhibit an average discharge capacity of 148.2 ± 1.5 mAh g^{-1}. This difference equals an increase of more than four percent in cell performance by using Gel_{10}. The disparity between the cells increases as the discharging rate increases as well. At 5 C Gel_{10} shows an eight percent higher performance in comparison to Gel_{250}. This further underlines the previously observed influence of the electrical resistance on the rate performance, as Gel_{10} shows comparably lower electrical resistance in comparison to Gel_{60}, Gel_{100}, and Gel_{250}. The cell format used was coin cells. While coin cells are available in a shorter time, the limited stability of the format overshadows the impact of the gel particles on long-term cycling. Observing longer cycling durations was not able to provide any further insights into the anodes' influence on cell performance. [201] This is due to the inherent risk of the coin cell format becoming less sealed, making long-term cycling results of limited use.

While the differences are clearly apparent, it is of special interest how the influence impacts the anode's charging performance, when the anode is strained even further than the usual 1 C charging rate with the added CC CV step. The corresponding charge rate capability step for anodes with different gel particle content is shown in Figure 5.19.

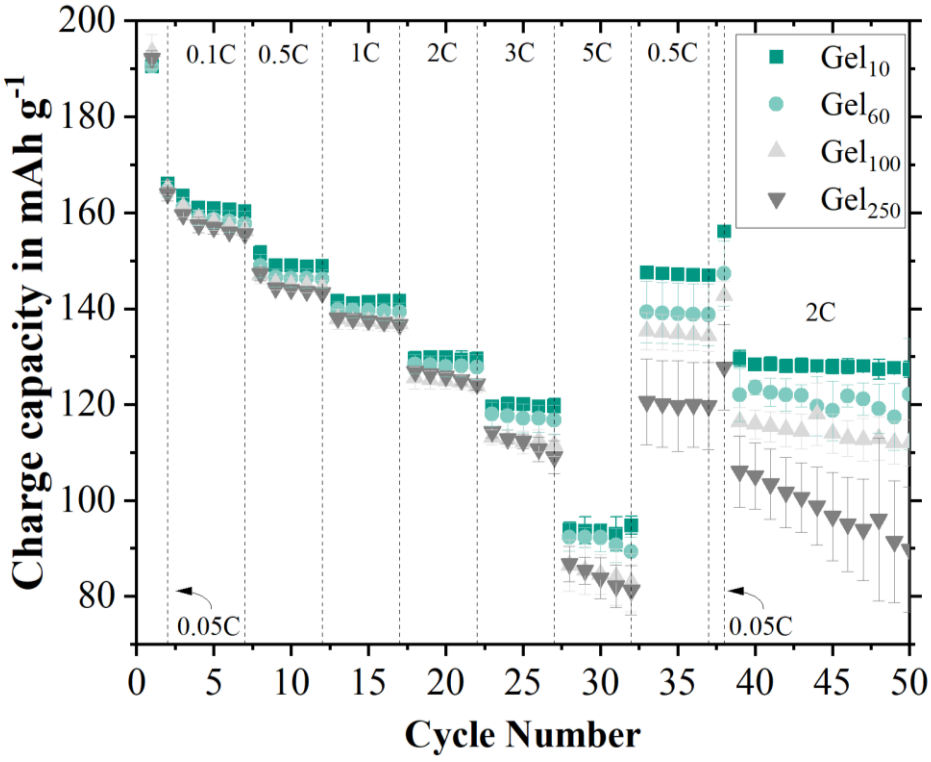

Figure 5.19: Charge rate capability test for anodes containing NaCMCs with different gel particle content.

When stressing the anode even further with the charging rate capability test, the same order in performance is observed, with Gel_{10} delivering the highest charge capacity. When the strain is the

highest for the anodes at 5 C Gel_{10} and Gel_{60} stay almost constant, while Gel_{250} shows a significant drop off in capacity from 87 mAh g^{-1} to 81 mAh g^{-1}. After the rate capability test was finished, the retaining capacity at a lower charging rate of 0.5 C was detected. Again, Gel_{10} showed the highest capacity retention with 99.0 % of the initial capacity at 0.5 C, with retention declining for Gel_{60} with 95.8 %, further lowering for Gel_{100} with 93.1 %, with the lowest being Gel_{250} with 82.8 %. The amount of gel particles is directly coupled to the performance of the cell. The increase in rate capability is attributed to the better overall volume resistivity shown by electrodes with lower gel particles as Gel_{10} shows a decrease of 14 % in comparison to Gel_{250}. Nevertheless, the steady increase in water content directly correlated with the amount of gel particles and was suspected to negatively impact the SEI formation, the lithium inventory, and therefore the capacity. [198-200] This led to a post-mortem analysis of the cells, with the EDS results for the corresponding electrodes displayed in Figure 5.20.

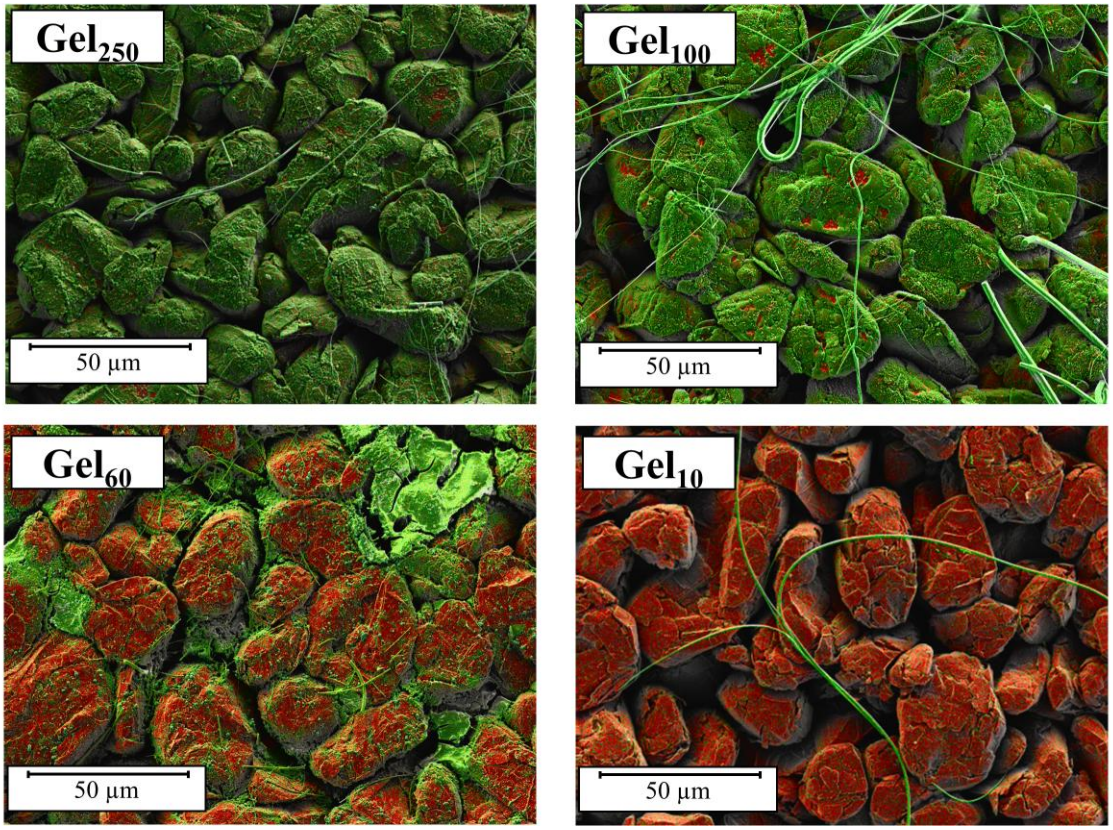

Figure 5.20: Post-mortem EDS analysis of four anodes containing different amounts of gel particles, with different amounts displayed in the top left corner. EDS measurements were conducted after the discharge rate capability test. Green: Oxygen, Red: Carbon.

For the highest amount of gel particles Gel_{250}, a continuous layer of high oxygen-containing species is detected via EDS totalling 48 atom%(O). Reducing the gel particle content in the electrodes correlates with a reduction in visible oxygen-containing species, as well as a reduced total amount of oxygen detected with Gel_{100} only totalling 40 atom%(O), Gel_{60} reducing the oxygen content to 11 atom%(O), while Gel_{10} shows the lowest total oxygen with only 9 atom%(O). This decrease in oxygen content is in line with the previously observed cell performance results. A higher

absolute content of oxygen adds to the suggestion, that water increases the SEI thickness by negatively impacting the electrolyte degradation due to catalysing side reactions. [10,116] The oxygen content of the EDS is used as an indication for the SEI layer. Gel_{250} therefore shows the thickest SEI layer. This difference in SEI is in line with the cell results and allows to further explain the differences in rate capability performance for the different gel particle contents in the anodes. When decreasing the amount of gel particles, the amount of remaining water significantly decreases (see Figure 5.9). This allows for a thinner SEI, with less electrolyte salt reacting with the water impurity. To control the SEI thickness, the residual water content in the electrodes therefore needs to be controlled or further reduced to increase the performance.

Instead of creating a framework to increase the energy requirement for the anodes as a higher energy requirement would decrease the beneficial aspects of water-based processing, it is of more interest to reduce the drying time. To further increase the efficiency of water-based processing it would be of great interest to further reduce the amount of time needed to dry the electrodes. As shown before, anodes containing Gel_{10} already showed the best performance for 16 hours of secondary drying at 120 °C under vacuum. This suggests a further reduction of the drying duration to skipping secondary drying altogether, to investigate if residual water uptake of the low gel content electrodes becomes a noticeable issue for the cell performance. The comparison of the rate capability test for anodes dried for zero hours and 16 hours under vacuum is shown in Figure 5.21.

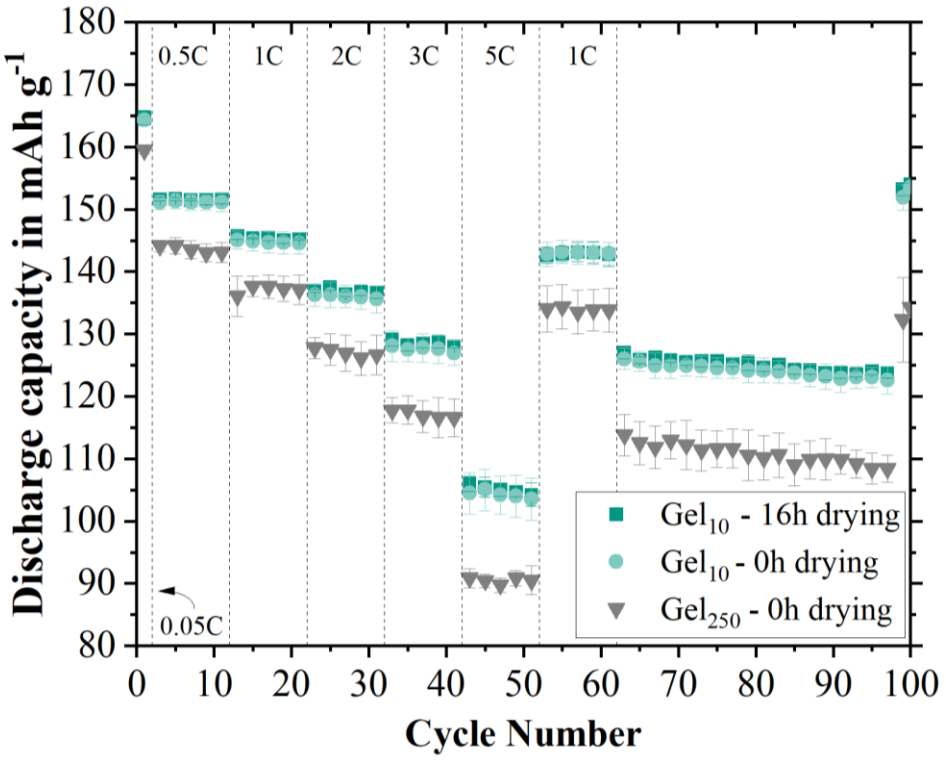

Figure 5.21: Comparison of discharge rate capability tests for anodes containing different NaCMCs with changing secondary drying conditions, either the usual drying protocol with 120 °C for 16 hours under vacuum (labelled 16h drying) or no secondary drying (labelled 0h drying). For better visibility, only every second value is shown in the rate capability test.

When comparing Gel_{10}, decreasing the drying intensity had a negligible negative impact on the cell performance. There is a small difference between no drying and 16 hours under vacuum at 120 °C. In contrast, using anodes containing Gel_{250} without any further drying leads to a drastic decrease in capacity retention in the initial discharge. This is further amplified by increasing discharging rates again. Finally, when observing the 0.05 C step after 100 cycles, Gel_{250} shows a significantly lower capacity, again indicating a lower residual lithium inventory in comparison to Gel_{10}.

This indicates, that electrodes containing Gel_{10} as NaCMC show very low residual water making secondary drying obsolete. Using low gel NaCMCs not only allows to avoid thick SEI formation, which is likely for high gel particle contents due to high contents of residual water but further reduces the need for time-intensive secondary drying altogether. This drastically reduces the time required for anodes to be available in cell manufacturing. On the other hand, when using high gel particle content NaCMCs, drying is essential to avoid introducing excessive amounts of residual water into the cell. As observed in the post-mortem analysis, this leads to a drastic decrease in SEI formation and therefore increases the capacity, due to less lithium inventory loss.

5.3 Selective staining of NaCMC

As of today, no method enables the localisation of the NaCMC within the anode by selectively staining the binder in the prepared electrode. As NaCMC is shown in Figure 2.5, there are various reactive groups which are readily usable. When creating a cross-section of a graphite electrode using NaCMC, the EDS is not able to detect the sodium ions as their concentration throughout the electrode is too low. This leads to an inaccurate display of its distribution via the EDS, as depicted in Figure 5.22.

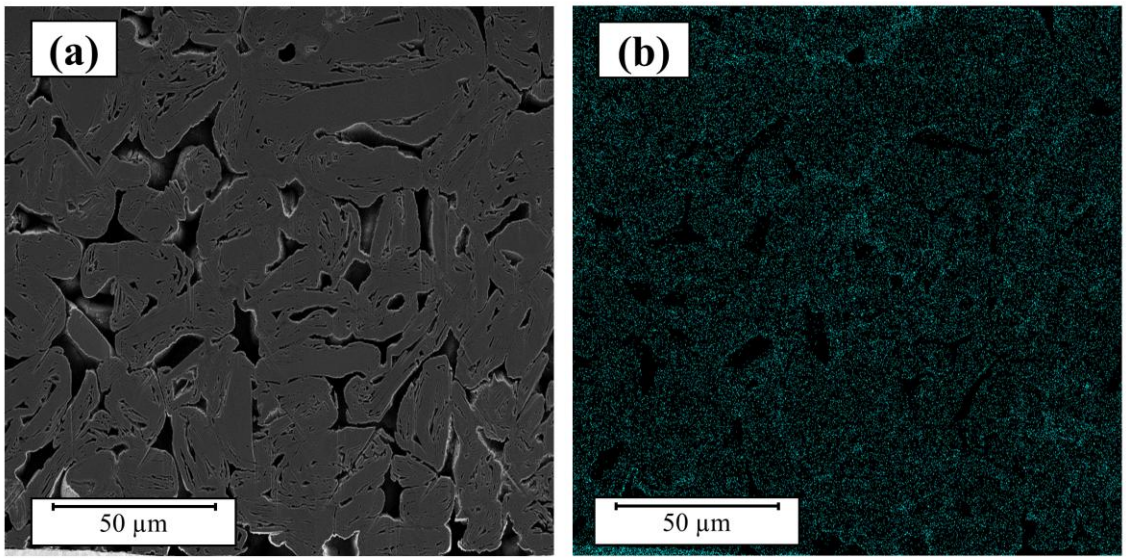

Figure 5.22: SEM micrographs of a graphite electrode cross-section containing $CMC_{0.67,\ low\ MW}$. (a) SEM micrograph of the cross-section. (b) Corresponding sodium (light blue) EDS mapping result.

Despite the sodium ions being present throughout the electrode, it is not possible to properly locate the NaCMC, as there is no detectable, local increase in signal strength. It is, therefore, necessary to selectively stain the NaCMC to allow for the binder to be accurately displayed and to gain further knowledge about binder migration, distribution and therefore processing.

To investigate the applicability for the use in electrodes, three different reagents were combined with pure NaCMC of $CMC_{0.67,\ low\ MW,}$ while either in solution or as a dried coating depending on the agent. The first staining agent is an aqueous $KSb(OH)_6$ solution, which reacts with sodium to form an insoluble sodium salt, which precipitates in water and leads to antimuonium being detectable via EDS. Another staining agent is the Lucas reagent, substituting the secondary alcohols of the NaCMC with chlorine. There are more secondary alcohols in comparison to the amount of sodium, leading to a higher number of chlorine atoms, which could be detected spectroscopically. The third staining agent is a silane, (heptadecafluorodecyl)-trimethoxysilane (HDF-TMS). All the exact procedures for both the preliminary investigations and the staining in electrodes are summarised in chapter 4.8.

All three approaches showed usable reactions with the pure NaCMC in the preliminary tests. Regarding a pure NaCMC solution, the $KSb(OH)_6$ agent creates small crystallites with the sodium ions present in the NaCMC. When adding the Lucas reagent to a pure NaCMC solution, it creates a white, opaque dispersion, showing that the reaction with the secondary alcohols of the NaCMC is possible. Finally, when allowing the HDF-TMS to react with a dried NaCMC coating, the EDS showed a significant increase of fluorine content at the NaCMC sites.

5.3.1 Staining with $KSb(OH)_6$

The different staining agents then are applied to stain the NaCMC in the corresponding electrode layers. Sample preparation with an aqueous $KSb(OH)_6$ solution showed further challenges. Despite a saturated environment, some electrodes disintegrate, due to the NaCMC dissolving in water again. Additionally, using a water-soluble salt comes with the inherent risk of creating crystallites after drying on top of the active material, from excess staining agent. This led to either excess $KSb(OH)_6$ forming on top of the electrode, see Figure 5.23, or the disintegration of the electrode, when properly washing with water.

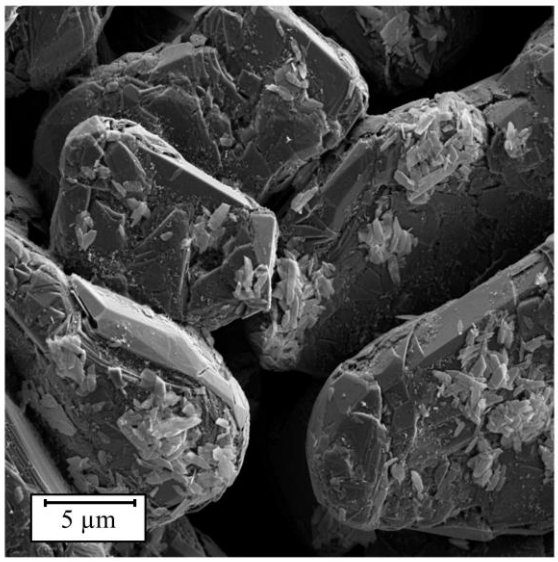

Figure 5.23: SEM micrographs of a graphite electrode containing $CMC_{0.67,\ low\ MW}$ and stained with a $KSb(OH)_6$ solution, with $KSb(OH)_6$ crystallites visible on top of the graphite.

An aqueous $KSb(OH)_6$ solution therefore is an improper staining agent for being used in electrodes containing NaCMC.

5.3.2 Staining with the Lucas reagent

The Lucas reagent also showed a positive result in the preliminary investigations and is also based on water-soluble zinc chloride salts and concentrated hydrochloric acid. Nevertheless, sample preparation is without similar challenges compared to aqueous $KSb(OH)_6$. When storing the electrodes, either with or without a copper CC inside the aqueous solution, the electrode is not disintegrating. One possible reason for the higher cohesion of the electrode could be the cross-linking of sodium via the multivalent zinc ions, locking the NaCMC in place and hindering the dissolution of the NaCMC. Washing the electrodes after staining therefore was possible without negative impact on the stability of the electrode. SEM micrographs of an electrode coated onto a copper CC and one free-standing electrode without copper CC, stained with the Lucas reagent, are illustrated in Figure 5.24.

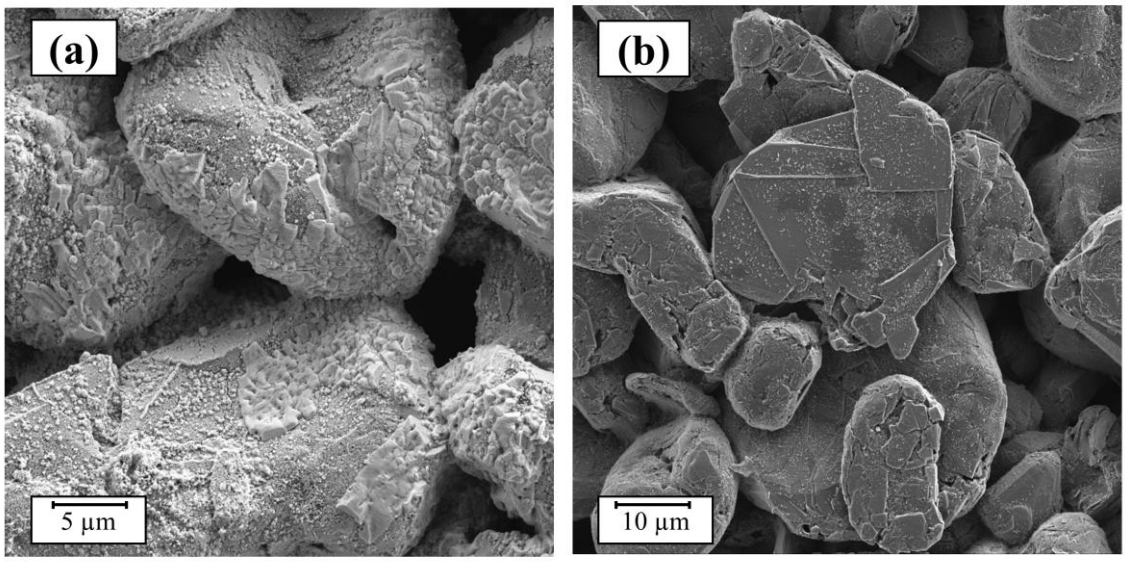

Figure 5.24: SEM micrographs of two different samples with the Lucas reagent. (a) Graphite anode on top of copper. (b) Free-standing graphite electrode without a copper current collector.

For the electrode, the dissolution of NaCMC is not the main drawback, but the strongly acidic environment of hydrochloric acid. It leads to the dissolution of copper, which precipitates throughout the whole electrode as copper chloride. This overshadows any possible substitution of the hydroxyl groups with the Lucas reagent and the detection of chlorine in the EDS as a hetero atom. In comparison, the free-standing electrode was free of any copper during the staining. However, despite overcoming the formation of copper chloride during the staining process, there was no chlorine detectable on the free-standing electrode sample, rendering the method impractical. This could be due to the Lucas reagent not reacting sufficiently with the NaCMC, leaving too small amounts of chlorine at the NaCMC sites. Therefore, both the use of an aqueous $KSb(OH)_6$ solution and the Lucas reagent lead to a reaction with a pure NaCMC sample but are unable to trace the NaCMC in the electrode.

5.3.3 Staining with HDF-TMS

When choosing HDF-TMS, the previous limitations of the other staining agents were considered. HDF-TMS itself is not a salt, it is liquid by itself and has to be applied via another organic solvent like ethanol. Diluting HDF-TMS with another solvent hinders self-condensation and allows for the activated HDF-TMS to be available for reaction with active sites in the NaCMC. Furthermore, HDF-TMS introduces multiple fluorine atoms, when reacting with the NaCMC polymer. This allows amplification of the signal for the NaCMC, as only a few reaction sides are available for the HDF-TMS to react with the polymer. When considering the application, side reactions with other components of the electrode have to be examined. The EDS mapping results for fluorine of the individual components used in the slurry are shown in Figure 5.25 after HDR-TMS staining. All were stained with HDF-TMS according to chapter 4.8.

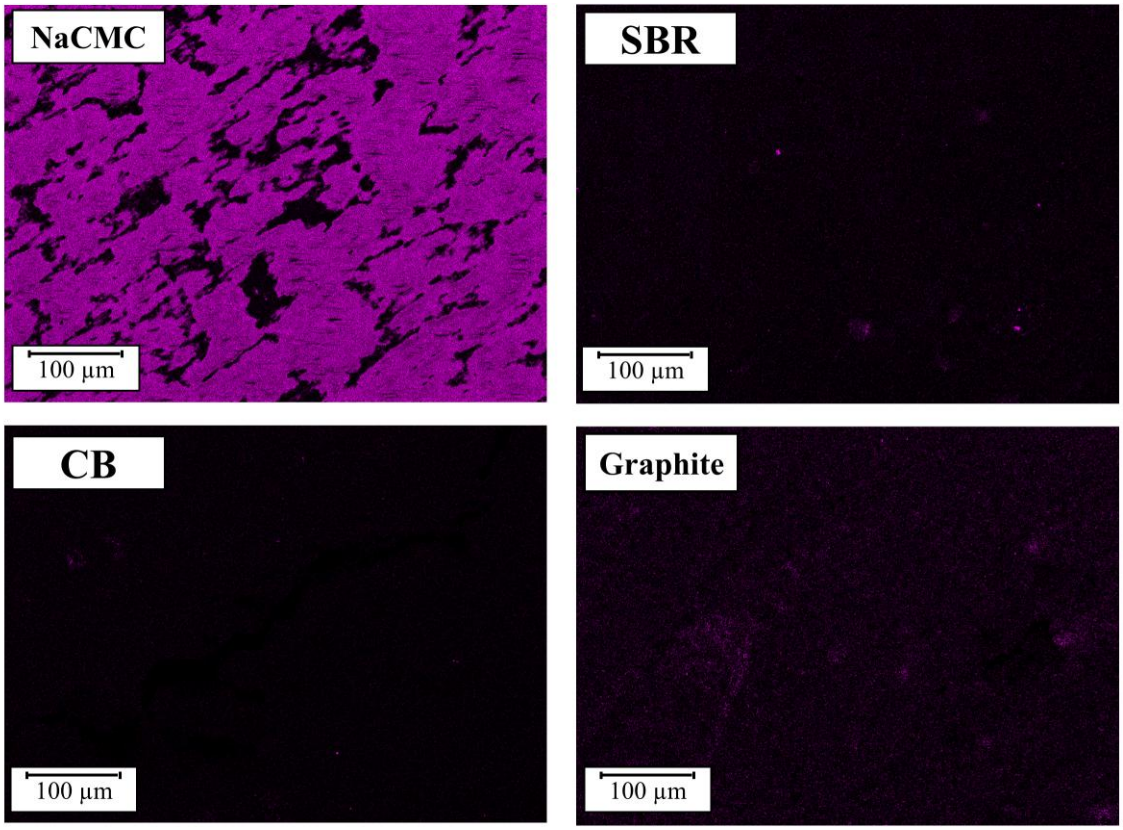

Figure 5.25: EDS mapping results of fluorine (magenta) for corresponding components of graphite electrodes after staining with HDF-TMS. (Reproduced from Keim et al. [192])

To apply HDF-TMS to the porous electrodes the staining agent needs to selectively react with the NaCMC when used in a graphite anode. Only NaCMC shows significant amounts of fluorine via EDS, with a total of 44.4 atom% of fluorine. In comparison, the second highest amount is graphite with only 0.4 atom% of fluorine, suggesting that only NaCMC is reacting with the HDF-TMS and serves as a proof of concept. The corresponding EDS mapping results of a graphite electrode containing $CMC_{0.67,\ low\ MW}$ are illustrated in Figure 5.26.

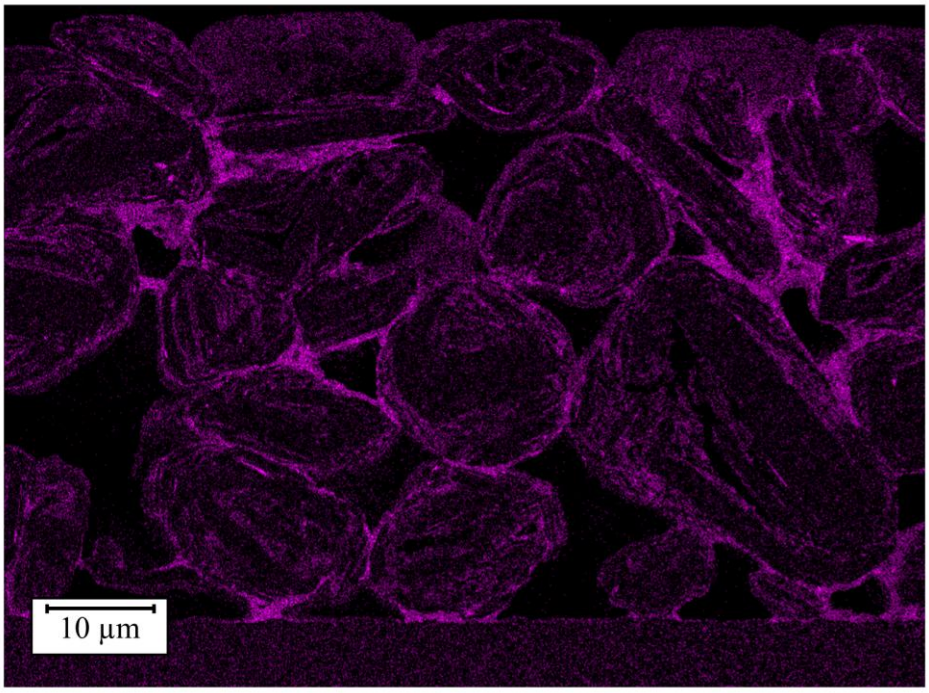

Figure 5.26: EDS mapping results after staining with HDF-TMS of fluorine (magenta) graphite anode cross-section, containing $CMC_{0.67,\ low\ MW}$. (Reproduced from Keim et al. [192])

Fluorine is detected via EDS in between particles and sometimes even inside particles. Additionally, neither the graphite surface nor the copper current collector displays high amounts of fluorine. The EDS results therefore suggest, that HDF-TMS reacts with NaCMC inside of the porous electrode structure and not only with a pure NaCMC sample. Fluorine is observed in places where the polymer binder is expected, like in between particles. Additionally, the binder is detected at other locations for instance inside the active material particles. It is, therefore, of further importance to clarify, if the fluorine introduced by the staining agent is accurately portraying the NaCMC distribution.

Accurately displaying the NaCMC includes excess staining agent being properly removed when the staining is done. Therefore, the staining agent that has not reacted with NaCMC is not supposed to stay in the porous electrode. Otherwise, excess staining agent could lead to false positive results and would lead to misinterpretation of the data as NaCMC, despite only showing the staining agent. To investigate this, the condensation reaction which occurs at elevated temperatures (here at 60 °C) should be less favoured, with the temperature of the staining being lower. Therefore, a graphite anode is submerged in the staining agent for 16 hours in ambient conditions. This allows the staining agent to properly wet the electrode and the proper distribution of the activated HDF-TMS throughout the porous structure, without enhancing the condensation reaction to take place between the staining agent and NaCMC. Afterwards, the sample was washed with ethanol according to chapter 4.8.3. After residual ethanol is fully evaporated, cross-sections are measured via EDS, see Figure 5.27.

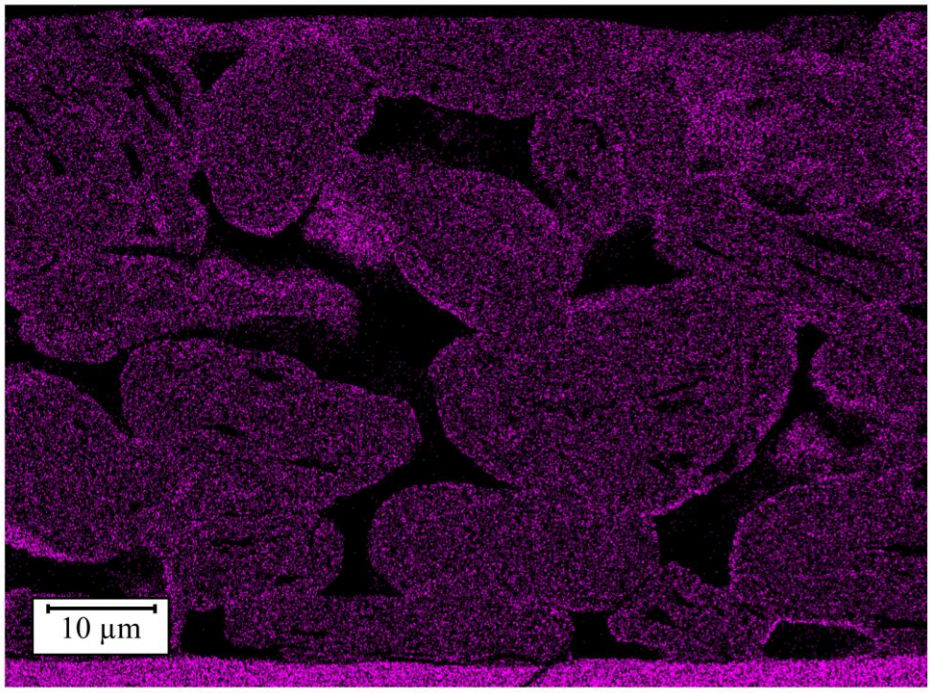

Figure 5.27: EDS mapping results of fluorine (magenta) after storing the electrode in HDF-TMS at ambient conditions for 16 hours. (Reproduced from Keim et al. [192]).

With only 0.11 atom% of fluorine being detected, the resulting fluorine distribution rather displays measurement artefacts instead of a factual fluorine distribution. While the investigations of the raw material CB show no reaction with fluorine, HDF-TMS could possibly adhere in the porous anode. This would be reasoned with the increase in surface available in comparison to the compressed sample, which was submerged in the staining agent. Nevertheless, even when enhancing the focus on those areas with high amounts of CB, there is not more fluorine detectable via EDS (see Appendix A 5). Even when comparing the CB fluorine content with other parts of the porous electrode, the detectable fluorine concentration stays similar to the average of the cross-section. This further indicates that the HDF-TMS is not adhering or reacting with other components when stored in ambient conditions. This includes the high surface area of conductive additives such as CB.

Increasing storage time, when allowing for the condensation reaction to take place at elevated temperatures, is coupled with an increase in fluorine concentration, see Figure 5.28. While four hours show 0.46 ± 0.03 atom% fluorine, it steadily increased. Eight hours lead to 1.1 ± 0.1 atom%, with 16 hours reaching 1.5 ± 0.1 atom%, and 60 hours showing the highest measured value of 4.4 ± 0.2 atom% of fluorine. [192] This demonstrates, that the staining process is time dependent. A storage time of 16 hours creates sufficient staining of the NaCMC, as already shown with the aforementioned sample. Increasing the temperature is therefore necessary to allow for a reaction to take place between the NaCMC and the HDF-TMS. By changing the storing duration of the samples in the staining agent, it was possible to identify conditions of sufficient staining of the NaCMC.

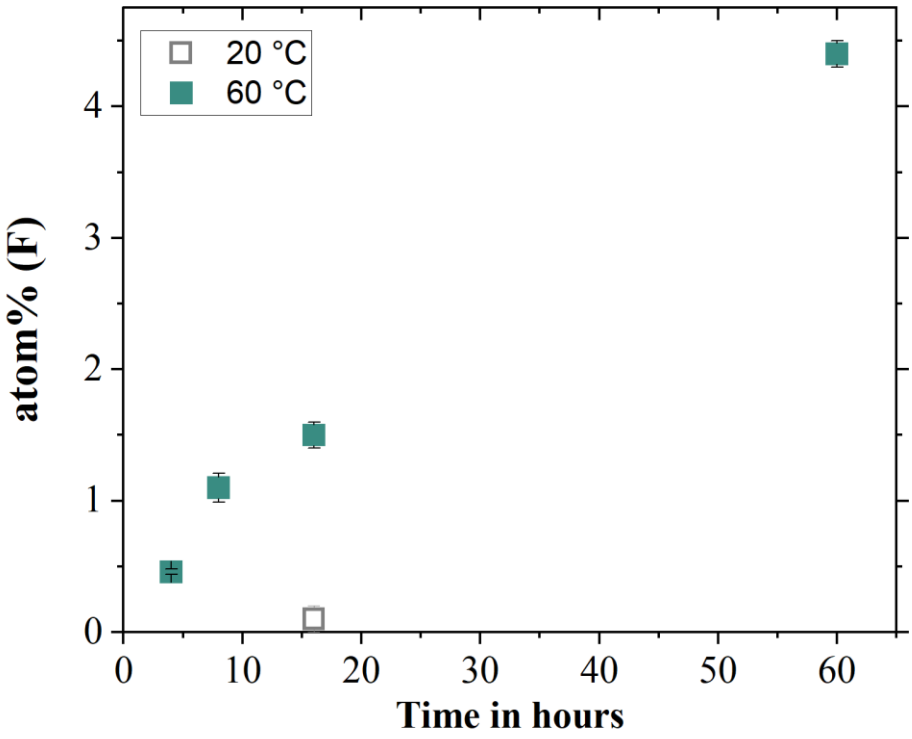

Figure 5.28: Time-dependent fluorine concentration detected per cross section, after HDF-TMS staining. The result of staining at ambient conditions is shown as well. All anodes contained $CMC_{0.67,\ low\ MW}$ and the fluorine content was detected via EDS.

Shortening the exposure times leads to less pronounced staining. By decreasing the contrast and reducing the amount of reacted staining agent, the binder distribution could be portrayed as less accurate, as the signal-to-noise ratio decreases. Further extending the storing duration leads to a higher amount of fluorine being observed. Higher fluorine content being detectable creates a better contrast in comparison to lower amounts of fluorine. This becomes especially apparent when comparing the mapping results for 16 hours and 60 hours of storing time, as shown in Figure 5.29. Two possibilities are potentially explaining the steady increase in fluorine concentration. For one, HDF-TMS could continuously react with the NaCMC. Nevertheless, the long duration combined with the steady increase in fluorine detectable rather reasons for the self-condensation reaction of the HDF-TMS. [202] The silane then reacts with itself creating a multitude of silicon-oxygen bonds leading to a high concentration of fluorine. If the self-condensation occurs, the staining agent would then not depict the NaCMC on its own, but even further enhance the visibility, as observed in Figure 5.29. Nevertheless, 16 hours of storing at elevated temperature creates a sufficient contrast to detect the NaCMC.

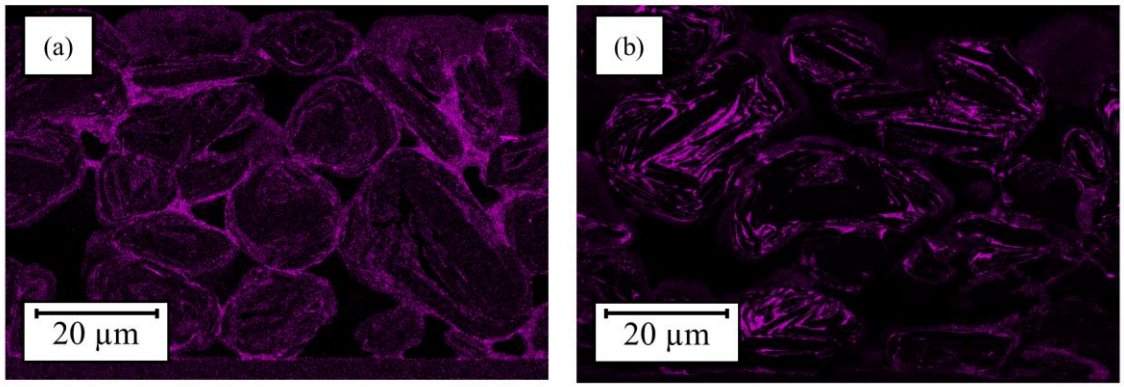

Figure 5.29: Time-dependent fluorine (magenta) concentration detected via EDS per cross section (a) 16 hours (b) 60 hours of staining with HDF-TMS. The difference in fluorine content did not lead to an improved localisation of NaCMC. All anodes contained $CMC_{0.67,\ low\ MW}$ (Reproduced from Keim et al. [192]).

To finalise the understanding of whether the HDF-TMS reacts with the NaCMC carboxyl or hydroxy moieties, different DS of NaCMCs were investigated to compare changes in the reaction sites. The results of various anodes containing different NaCMCs, with lower ($CMC_{0.42,\ low\ MW}$), middle ($CMC_{0.67,\ low\ MW}$) and high ($CMC_{0.95,\ low\ MW}$) DS are illustrated in Figure 5.30.

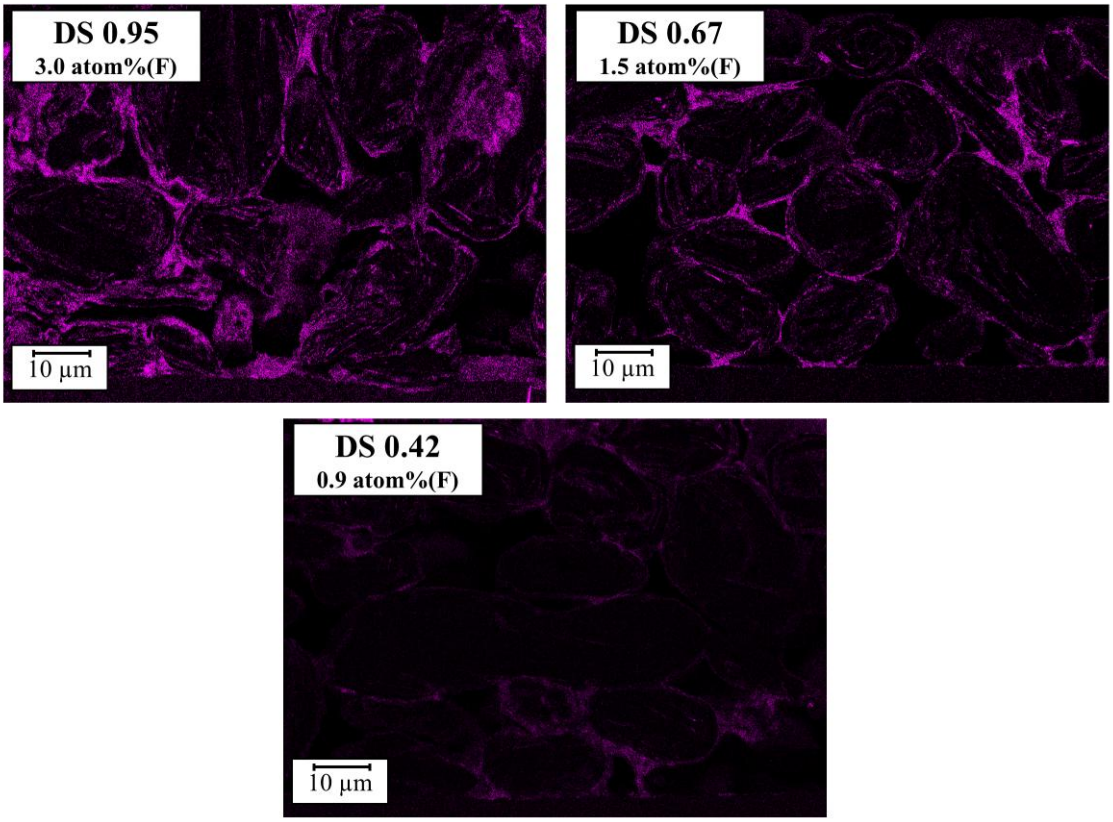

Figure 5.30: Fluorine (magenta) concentration detected via EDS for cross sections of electrodes containing NaCMCs with different DS after staining with HDF-TMS (Reproduced from Keim et al. [192]).

The respective amount of fluorine detected in each cross-section is displayed as well. The electrode containing $CMC_{0.42,\ low\ MW}$ leads to 0.9 ± 0.1 atom%, while it increases for $CMC_{0.67,\ low\ MW}$ to 1.5 ± 0.1 atom%. The highest fluorine content is detected for $CMC_{0.95,\ low\ MW}$ with 3.0 ± 0.1 atom%. Increasing the DS therefore is accompanied by a higher amount of observable fluorine. Another positive implication of the higher DS is the higher water retention. When more water is stored inside the NaCMC, if there is any leftover HDF-TMS which was not previously hydrolysed, it could directly form at the reaction site, further reducing the risk of side reactions. The staining duration could therefore be adjusted depending on the DS to allow for equal contrast.

Gadhave et al. suggest, that silanes reacting with pure cellulose are coupled with the polymer backbone through the hydroxyl groups. [203] The results strongly indicate that the silane is reacting with the carboxyl moieties in the NaCMC, reasoning the following reaction mechanism illustrated in Figure 5.31. [192]

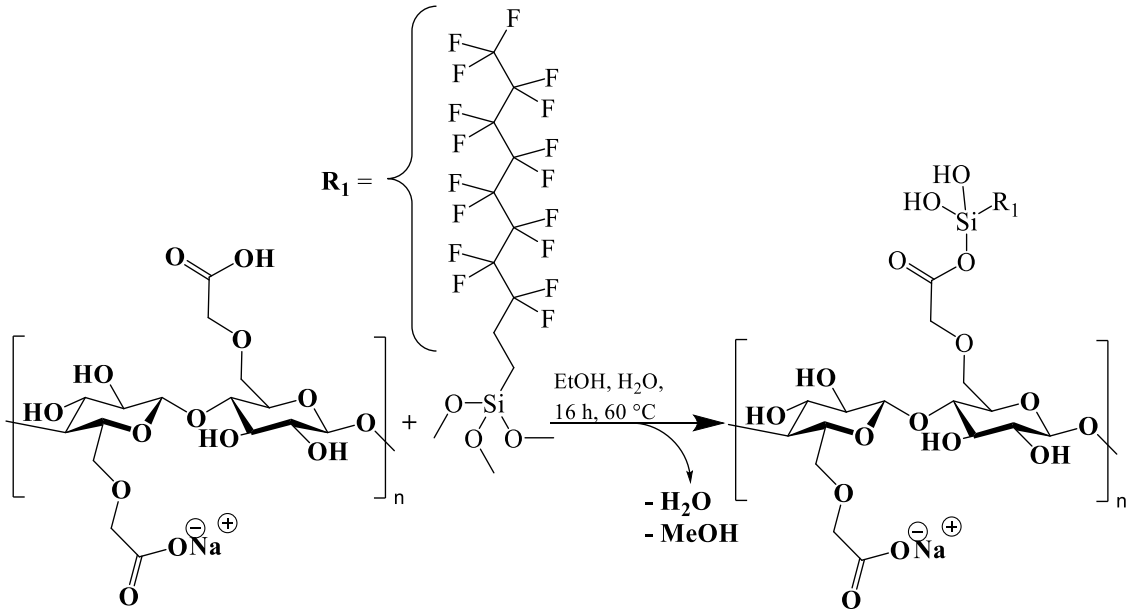

Figure 5.31: Possible reaction mechanism of HDF-TMS with NaCMC, without prior activation. MeOH and EtOH are used as abbreviations for Methanol and Ethanol respectively (Reproduced from Keim et al. [192]).

The complete activation of the HDF-TMS to the silane, due to using excess water, allows for the silane to further be reactive after bonding to the NaCMC. This would create new reaction sites for the self-condensation reaction of the silane with a further activated staining molecule.

6 Summary

The main focus of this dissertation is on creating a deeper understanding of the influence of sodium carboxymethyl cellulose (NaCMC) on the properties of negative electrodes for lithium-ion batteries and how those translate into cell performance. The main emphasis is given to the degree of substitution (DS) and gel particles.

Using the surface free energy (SFE) method and the connected theoretical concepts allows for understanding the driving forces behind the interactions for NaCMCs with different DS and how those changes affect the final electrode properties. This is especially apparent for the adhesion, electrical resistance, and residual water content, where the investigations lead to a proper understanding of interactions and electrode properties. The method shows how an increasing DS leads to decreasing electrical resistance as the interaction with the conductive additive becomes more likely. Additionally, a decrease in DS also enhances the adhesion strength of the electrode, as the interaction of NaCMC with carbon black becomes less likely, while the interaction with SBR and the current collector increases. Finally, the SFE method allows for the correlation that the higher hydrophilicity of NaCMCs translates into higher residual water content in dried anodes.

It was also recognised that the SFE method shows some boundaries regarding its applicability. Polymer properties, like the molecular weight and impurities, are not expressed by a change in SFE, therefore leading to the same interpretations while impacting the electrode properties.

The observed influence of NaCMC on electrode properties directly translates into the cell performance. It was found that NaCMC with a low molecular weight and a DS of 0.67 provided the best electrochemical results in comparison to all other NaCMCs used. Various factors lead to this NaCMC to provide the best environment for the active material. When the DS is increased beyond 0.67, the residual water content also increases. The higher the amount of residual water in the electrodes, the worse the capacity retention, which is both in line with the literature and the observations of the cell performance. When decreasing the DS below 0.67, the capacity retention also decreases. While the water retention is lower in comparison to higher DS NaCMCs, the electrical resistance increases. The higher the discharging rates, the more apparent the disparity becomes, suggesting that the differences in capacity retention are due to the gradual increase in electrical resistance. While higher molecular weight NaCMCs show decreasing interfacial resistance, which could positively impact the rate capability performance, the high amount of residual water overshadows any benefits, decreasing the cell performance significantly. All investigated high molecular weight NaCMCs, therefore, show lower capacity retention and cell performance than their respective low molecular weight counterpart.

The influence of water on the cell performance becomes especially apparent when using the same polymer properties while increasing the gel particle content gradually. The higher amount of residual water led to a decrease in capacity retention and cell performance, with the anode containing the lowest gel content showing both the highest cell performance and lowest residual water content. This was in line with the observed post-mortem results showing a correlation between SEI formation on the anode and residual water content in the dried electrodes. The SEI was most

pronounced for the highest residual water content. Therefore, one of the most important findings in this work is to control the gel particle amount in the electrode to ensure optimal performance.

Finally, a novel staining approach using HDF-TMS for the visualisation of NaCMC via EDS was shown. While other staining agents were insufficient in properly staining the NaCMC, HDF-TMS showed positive results. It only reacts with the NaCMC, without adhering or reacting with other species in the electrode. Additionally, a reaction mechanism was proposed based on the results, which suggest that the carboxyl moieties of the NaCMC are the ones responsible for the reaction with the NaCMC.

7 Outlook

The SFE method offers great potential, but the limitations regarding changing polymer properties and the increasing number of interactions being affected by interchanging one component have to be considered. Nevertheless, it is of exceptional value in understanding and exploring the differences in polymer properties influencing the electrodes. This leads to a multitude of possible future applications not only limited to the processing side of the electrodes. It could help further understand the wetting behaviour of electrolytes on electrodes, designing specific surface behaviours to increase adhesive properties (e.g. via corona treatment) or used as a tool to further explore interactions in dry processing. Future work could also expand on these findings by applying the SFE method and theory on other binder systems, i.e. sodium alginates, to further understand and explore the impact different polymer properties have on the electrode properties.

Secondly, when combining all results, it showed that NaCMC is significantly impacting the cell performance through its influence on the electrodes. The systematic investigation of different NaCMC polymer properties further allowed us to identify the best-performing NaCMC, a NaCMC with a low molecular weight and a DS of 0.67. The proposition of said NaCMC being the best NaCMC for every application is not factual. It rather identifies two very important key figures influencing the cell performance, which are the residual water content and electrical resistance. The gained understanding of influences of increased water retention based on the respective binder and its impact on the cell performance could also be applied to other water-based anode formulations. Furthermore, the high molecular weight NaCMCs showed higher adhesion strength in comparison to the lower molecular weight NaCMCs. Future investigations should focus on whether the high molecular weight systems provide enough mechanical stability to allow formulations disregarding SBR binder. Another focus of interest could be reducing the high molecular weight fraction, which could lead to a higher active material loading, with the water retention being lower, as the decrease in NaCMC could lead to a lower number of entanglements.

Allowing for the selective staining of NaCMC also leads to a multitude of applications. Firstly, it provides a method which is easily applicable and can significantly improve the understanding of the NaCMC distribution. By using the staining method with other binders containing carboxylates, i.e. sodium alginates and poly (acrylic acid), the scope of application could be further expanded while better understanding the underlying reaction mechanism of the staining agent with the polymers.

Most notable is the significant influence of the small impurity of the gel particles on the cell performance and SEI formation. Gel particles were completely unaddressed in literature before, but showed drastic influence. Especially considering that by using low gel particle anodes, the secondary drying becomes obsolete. This could be investigated in large scale application, which would lead to a significant decrease in energy consumption while providing an increase in efficiency. Future work should therefore give the amount of gel particles in NaCMC, as the high impact of the impurity should not be disregarded considering cell performance.

8 Appendix

Regarding Chapter 5.1: Contact angles and SFE values for all electrode components.

Sample	Ethylene glycol	DMSO	Diiodo methane
	Contact angle in degrees		
CC	52.5 ± 2.0	22.2 ± 0.6	34.7 ± 0.7
CC_{New}	72.7 ± 0.8	49.8 ± 1.3	42.4 ± 0.2
$CC_{New,500W}$	42.2 ± 2.5	17.5 ± 0.6	57.5 ± 1.1
Graphite	30.9 ± 0.9	23.8 ± 1.9	17.9 ± 0.6
SBR	52.2 ± 1.7	29.7 ± 3.3	41.0 ± 3.4
$CMC_{1.23,\ low\ MW}$	13.5 ± 2.8	16.6 ± 2.3	50.7 ± 0.5
$CMC_{0.95,\ low\ MW}$	8.0 ± 1.6	12.4 ± 1.3	46.0 ± 2.4
$CMC_{0.85,\ low\ MW}$	5.3 ± 0.4	4.7 ± 0.9	46.2 ± 1.1
$CMC_{0.75,\ low\ MW}$	6.7 ± 1.3	4.8 ± 3.1	42.6 ± 1.0
$CMC_{0.67,\ low\ MW}$	6.6 ± 1.2	1.7 ± 1.0	35.6 ± 4.2
$CMC_{0.55,\ low\ MW}$	9.6 ± 0.3	3.0 ± 0.3	30.2 ± 0.7
$CMC_{0.42,\ low\ MW}$	11.3 ± 0.8	3.0 ± 0.8	24.6 ± 0.8
$CMC_{0.34,\ low\ MW}$	6.8 ± 0.2	2.6 ± 1.1	34.3 ± 0.7

Solid sample	γ_S	γ_S^d	γ_S^p
		in mN m^{-1}	
Copper CC	43.4 ± 0.8	42.2 ± 0.6	1.2 ± 0.4
Copper CC_{new}	35.5 ± 0.3	35.43 ± 0.2	0.1 ± 0.1
Copper CC_{500W}	39.3 ± 0.3	31.1 ± 0.2	8.2 ± 0.1
Graphite	48.1 ± 1.8	45.7 ± 1.4	2.4 ± 0.4
CB [a)]	31.7 ± 1.2	28.6 ± 1.0	3.1 ± 0.2
SBR	40.6 ± 0.7	39.2 ± 0.5	1.4 ± 0.2
$CMC_{1.23,\ low\ MW}$	46.0 ± 0.7	32.1 ± 0.5	13.8 ± 0.2
$CMC_{0.95,\ low\ MW}$	46.7 ± 0.5	34.2 ± 0.4	12.5 ± 0.1
$CMC_{0.85,\ low\ MW}$	47.3 ± 0.7	35.0 ± 0.5	12.3 ± 0.2
$CMC_{0.75,\ low\ MW}$	47.5 ± 1.0	36.9 ± 0.8	10.6 ± 0.2
$CMC_{0.67,\ low\ MW}$	48.4 ± 0.7	39.8 ± 0.5	8.6 ± 0.2
$CMC_{0.55,\ low\ MW}$	49.0 ± 1.5	42.0 ± 1.0	7.0 ± 0.5
$CMC_{0.42,\ low\ MW}$	49.9 ± 1.4	44.4 ± 1.1	5.5 ± 0.3
$CMC_{0.34,\ low\ MW}$	51.1 ± 1.4	46.3 ± 1.1	4.8 ± 0.3
$CMC_{0.7,\ high\ MW}$	47.3 ± 1.3	38.3 ± 0.7	9.0 ± 0.6
Gel_{250}	47.0 ± 2.5	36.8 ± 2.3	10.2 ± 0.2

[a)]: The values for the CB were measured via the Washburn method and reproduced from Weber et al. [67]

Appendix A 1: Upper Table: Results of the contact angle measurement via the sessile drop for slurry components and NaCMCs with different DS. Lower Table: Resulting surface free energy (γ_S), including the separation in the polar (γ_S^p) and dispersive (γ_S^d) contribution to the total surface free energy for the different components.

Regarding Chapter 5.2.2: NMR Results and ^{1}H NMR results for the pure d^{6}-DMSO solvent

Species	Chemical Shift in ppm	Multiplett
Ethylene Carbonate (EC)	4.48	*s*
Dimethyl Carbonate (DMC)	3.69	*s*
Hydrofluoric Acid (HF)	~ 10.6	*d*
DMSO (impurity)	6.28	*s*
Lithium Ethylene Dicarbonate (LEDC)	4.29	*s*
Ethyl Methyl Carbonate (EMC)	4.10 (J_{H-H}= 7.1 Hz)	*q*
Methanol	4.08 (J_{H-H}= 5.5 Hz)	*q*
EMC	3.70	*s*
Poly-Ethylene Oxide based oligomers	3.57	*m*
LP30 (impurity)	3.50	*s*
Water	3.34	*s*
DMSO (impurity)	3.31	*s*
LMC	3.24	*s*
Poly-Ethylene Oxide based oligomers	3.23	*m*
Methanol	3.17 (J_{H-H}= 5.5 Hz)	*d*
Lithium succinate	2.70	*s*
DMSO + DMSO satellites	2.50 (satellites: 2.67 + 2.33)	*m*
EMC	1.24 (J_{H-H}= 7.1 Hz)	*t*

Appendix A 2: Detailed summary of detected NMR species in ^{1}H-NMR for Figure 5.15 and Figure 5.16 (Chemical shift interpretation based on [185,186], impurities found in LP30 and DMSO are noted accordingly).

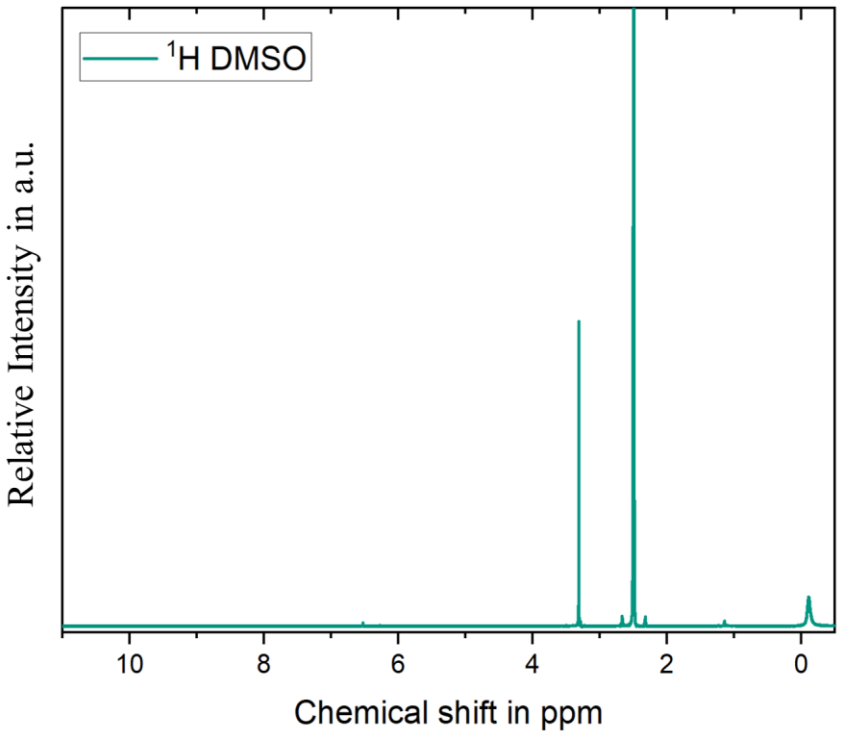

Appendix A 3: ^{1}H NMR results for the pure d^{6}-DMSO solvent used for the NMR investigations.

Regarding Chapter 5.2.4: Long-term cycling results for anodes with different gel particle contents

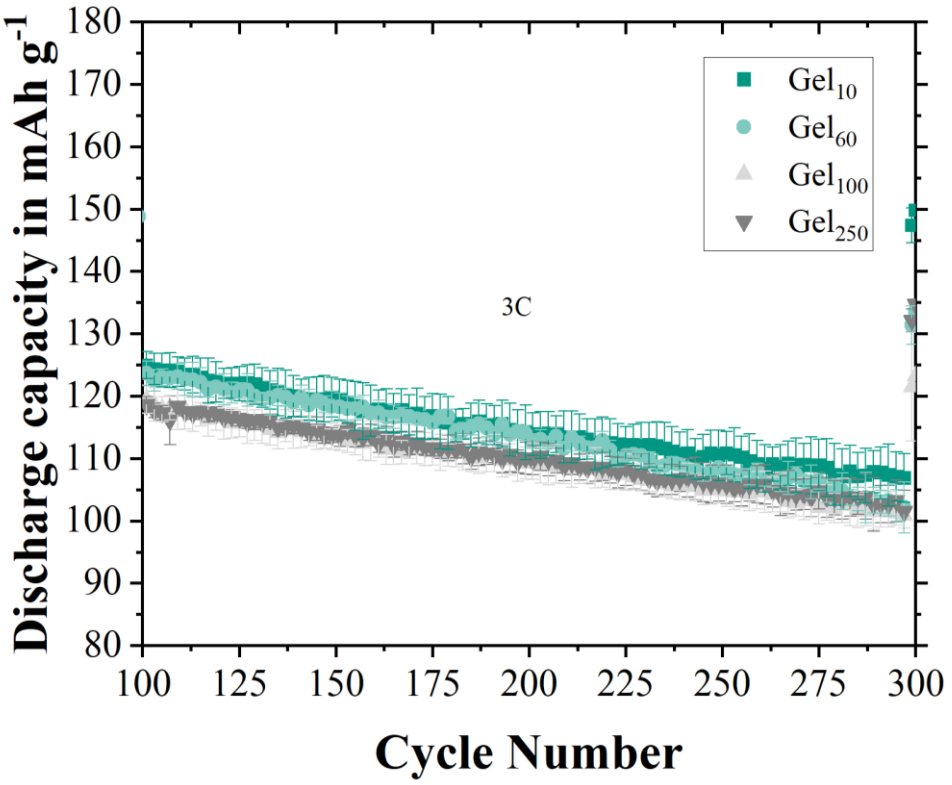

Appendix A 4: Long-term cycling results for anodes containing different amounts of gel particles in coin cell format.

Regarding Chapter 5.3: Enhanced carbon black (CB) agglomerate regarding staining agent

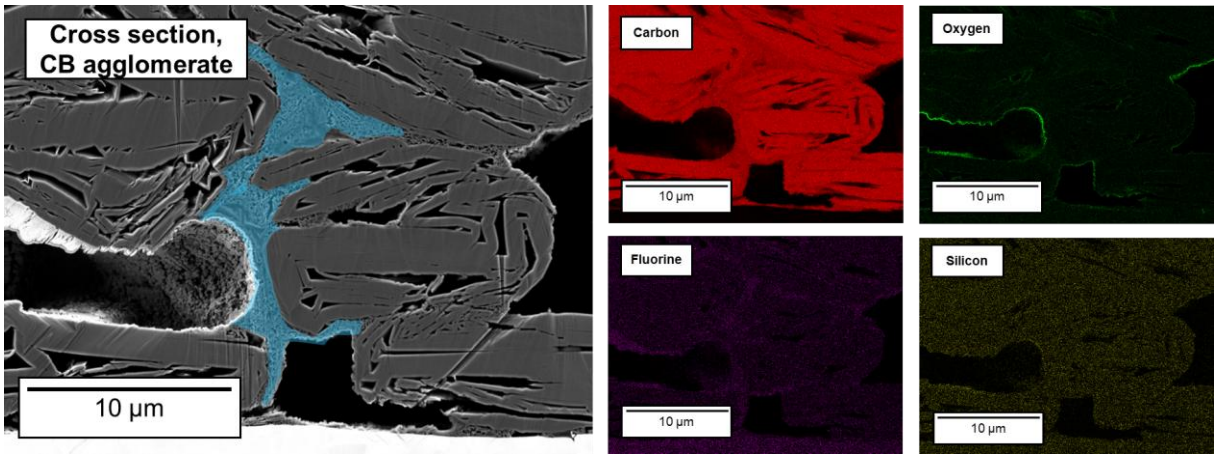

Appendix A 5: Enhanced and highlighted CB agglomerate in a graphite anode cross section. The left side shows the SEM micrograph with the CB agglomerate highlighted in blue. The right side lists the EDS mapping results for carbon (Red), oxygen (Green), fluorine (Magenta), and silicon (Yellow) (Reproduced from Keim et al. [192]). No residual staining agent is apparent in the fluorine EDS results.

For in-depth EDS results, please resort to Keim et al. [192] in ACS Applied Energy Materials.

9 Bibliography

1 Zou, F. & Manthiram, A. A Review of the Design of Advanced Binders for High-Performance Batteries. *Adv Energy Mater* **10** (2020). https://doi.org/10.1002/aenm.202002508

2 Bresser, D., Buchholz, D., Moretti, A., Varzi, A. & Passerini, S. Alternative binders for sustainable electrochemical energy storage – the transition to aqueous electrode processing and bio-derived polymers. *Energy & Environmental Science* **11**, 3096-3127 (2018). https://doi.org/10.1039/C8EE00640G

3 Cholewinski, A., Si, P. X., Uceda, M., Pope, M. & Zhao, B. X. Polymer Binders: Characterization and Development toward Aqueous Electrode Fabrication for Sustainability. *Polymers-Basel* **13** (2021). https://doi.org/10.3390/polym13040631

4 Wang, Y.-B., Yang, Q., Guo, X., Yang, S., Chen, A., Liang, G.-J. & Zhi, C.-Y. Strategies of binder design for high-performance lithium-ion batteries: a mini review. *Rare Metals*, 1-17 (2022). https://doi.org/10.1007/s12598-021-01816-y

5 Yoo, M., Frank, C. W., Mori, S. & Yamaguchi, S. Interaction of poly (vinylidene fluoride) with graphite particles. 2. Effect of solvent evaporation kinetics and chemical properties of PVDF on the surface morphology of a composite film and its relation to electrochemical performance. *Chemistry of materials* **16**, 1945-1953 (2004). https://doi.org/10.1021/cm0304593

6 Lestriez, B. Functions of polymers in composite electrodes of lithium ion batteries. *Comptes Rendus Chimie* **13**, 1341-1350 (2010). https://doi.org/10.1016/j.crci.2010.01.018

7 Wu, M. Y., Xiao, X. C., Vukmirovic, N., Xun, S. D., Das, P. K., Song, X. Y., Olalde-Velasco, P., Wang, D. D., Weber, A. Z., Wang, L. W., Battaglia, V. S., Yang, W. L. & Liu, G. Toward an Ideal Polymer Binder Design for High-Capacity Battery Anodes. *J Am Chem Soc* **135**, 12048-12056 (2013). https://doi.org/10.1021/ja4054465

8 Xu, J., Chou, S.-L., Gu, Q.-f., Liu, H.-K. & Dou, S.-X. The effect of different binders on electrochemical properties of LiNi1/3Mn1/3Co1/3O2 cathode material in lithium ion batteries. *Journal of Power Sources* **225**, 172-178 (2013). https://doi.org/10.1016/j.jpowsour.2012.10.033

9 Zhang, Z., Zeng, T., Lai, Y., Jia, M. & Li, J. A comparative study of different binders and their effects on electrochemical properties of LiMn2O4 cathode in lithium ion batteries. *Journal of Power Sources* **247**, 1-8 (2014). https://doi.org/10.1016/j.jpowsour.2013.08.051

10 Heiskanen, S. K., Kim, J. & Lucht, B. L. Generation and Evolution of the Solid Electrolyte Interphase of Lithium-Ion Batteries. *Joule* **3**, 2322-2333 (2019). https://doi.org/10.1016/j.joule.2019.08.018

11 Ui, K., Fujii, D., Niwata, Y., Karouji, T., Shibata, Y., Kadoma, Y., Shimada, K. & Kumagai, N. Analysis of solid electrolyte interface formation reaction and surface deposit of natural graphite negative electrode employing polyacrylic acid as a binder. *Journal of Power Sources* **247**, 981-990 (2014). https://doi.org/10.1016/j.jpowsour.2013.08.083

12 Liu, Y., Zhang, R., Wang, J. & Wang, Y. Current and future lithium-ion battery manufacturing. *iScience* **24**, 102332 (2021). https://doi.org/10.1016/j.isci.2021.102332

13 Buqa, H., Holzapfel, M., Krumeich, F., Veit, C. & Novák, P. Study of styrene butadiene rubber and sodium methyl cellulose as binder for negative electrodes in lithium-ion batteries. *Journal of Power Sources* **161**, 617-622 (2006). https://doi.org/10.1016/j.jpowsour.2006.03.073

14 Gordon, R., Orias, R. & Willenbacher, N. Effect of carboxymethyl cellulose on the flow behavior of lithium-ion battery anode slurries and the electrical as well as mechanical properties of corresponding dry layers. *Journal of Materials Science* **55**, 15867-15881 (2020). https://doi.org/10.1007/s10853-020-05122-3

15 Ishii, M. & Nakamura, H. Influence of molecular weight and concentration of carboxymethyl cellulose on rheological properties of concentrated anode slurries for lithium-ion batteries. *JCIS Open* **6**, 100048 (2022). https://doi.org/10.1016/j.jciso.2022.100048

16 Lopez, C. G., Colby, R. H. & Cabral, J. T. Electrostatic and Hydrophobic Interactions in NaCMC Aqueous Solutions: Effect of Degree of Substitution. *Macromolecules* **51**, 3165-3175 (2018). https://doi.org/10.1021/acs.macromol.8b00178

17 Wang, X., Liu, J., Gong, Z., Huang, C., He, S., Yu, L., Gan, L. & Long, M. Influence of Degree of Substitution of Carboxymethyl Cellulose on High Performance Silicon Anode in Lithium-Ion Batteries. *Electrochemistry* **87**, 94-99 (2019). https://doi.org/10.5796/electrochemistry.18-00012

18 Li, J., Fleetwood, J., Hawley, W. B. & Kays, W. From Materials to Cell: State-of-the-Art and Prospective Technologies for Lithium-Ion Battery Electrode Processing. *Chemical Reviews* **122**, 903-956 (2022). https://doi.org/10.1021/acs.chemrev.1c00565

19 Duan, J., Tang, X., Dai, H., Yang, Y., Wu, W., Wei, X. & Huang, Y. Building Safe Lithium-Ion Batteries for Electric Vehicles: A Review. *Electrochemical Energy Reviews* **3**, 1-42 (2020). https://doi.org/10.1007/s41918-019-00060-4

20 Amusa, H. K., Sadiq, M., Alam, G., Alam, R., Siefan, A., Ibrahim, H., Raza, A. & Yildiz, B. Electric vehicle batteries waste management and recycling challenges: a comprehensive review of green technologies and future prospects. *Journal of Material Cycles and Waste Management* **26**, 1959-1978 (2024). https://doi.org/10.1007/s10163-024-01982-y

21 Koech, A. K., Mwandila, G., Mulolani, F. & Mwaanga, P. Lithium-ion battery fundamentals and exploration of cathode materials: A review. *South African Journal of Chemical Engineering* **50**, 321-339 (2024). https://doi.org/10.1016/j.sajce.2024.09.008

22 Li, W., Erickson, E. M. & Manthiram, A. High-nickel layered oxide cathodes for lithium-based automotive batteries. *Nature Energy* **5**, 26-34 (2020). https://doi.org/10.1038/s41560-019-0513-0

23 Myung, S.-T., Maglia, F., Park, K.-J., Yoon, C. S., Lamp, P., Kim, S.-J. & Sun, Y.-K. Nickel-Rich Layered Cathode Materials for Automotive Lithium-Ion Batteries: Achievements and Perspectives. *ACS Energy Letters* **2**, 196-223 (2017). https://doi.org/10.1021/acsenergylett.6b00594

24 Asenbauer, J., Eisenmann, T., Kuenzel, M., Kazzazi, A., Chen, Z. & Bresser, D. The success story of graphite as a lithium-ion anode material - fundamentals, remaining challenges, and recent developments including silicon (oxide) composites. *Sustain Energ Fuels* **4**, 5387-5416 (2020). https://doi.org/10.1039/d0se00175a

25 Zhang, H., Yang, Y., Ren, D., Wang, L. & He, X. Graphite as anode materials: Fundamental mechanism, recent progress and advances. *Energy Storage Materials* **36**, 147-170 (2021). https://doi.org/10.1016/j.ensm.2020.12.027

26 Chung, D. D. L. Review Graphite. *Journal of Materials Science* **37**, 1475-1489 (2002). https://doi.org/10.1023/A:1014915307738

27 Kasnatscheew, J., Wagner, R., Winter, M. & Cekic-Laskovic, I. Interfaces and Materials in Lithium Ion Batteries: Challenges for Theoretical Electrochemistry. *Topics Curr Chem* **376** (2018). https://doi.org/10.1007/s41061-018-0196-1

28 Mundszinger, M., Farsi, S., Rapp, M., Golla-Schindler, U., Kaiser, U. & Wachtler, M. Morphology and texture of spheroidized natural and synthetic graphites. *Carbon* **111**, 764-773 (2017). https://doi.org/10.1016/j.carbon.2016.10.060

29 Kasnatscheew, J., Wagner, R., Winter, M. & Cekic-Laskovic, I. Interfaces and Materials in Lithium Ion Batteries: Challenges for Theoretical Electrochemistry. *Topics Curr Chem* **376**, 16 (2018). https://doi.org/10.1007/s41061-018-0196-1

30 Andersson, R., Borodin, O. & Johansson, P. Dynamic Structure Discovery Applied to the Ion Transport in the Ubiquitous Lithium-ion Battery Electrolyte LP30. *J Electrochem Soc* **169** (2022). https://doi.org/10.1149/1945-7111/ac96af

31 Luo, W., Cheng, S., Wu, M., Zhang, X., Yang, D. & Rui, X. A review of advanced separators for rechargeable batteries. *Journal of Power Sources* **509**, 230372 (2021). https://doi.org/10.1016/j.jpowsour.2021.230372

32 Costa, C. M., Lee, Y.-H., Kim, J.-H., Lee, S.-Y. & Lanceros-Méndez, S. Recent advances on separator membranes for lithium-ion battery applications: From porous membranes to solid electrolytes. *Energy Storage Materials* **22**, 346-375 (2019). https://doi.org/10.1016/j.ensm.2019.07.024

33 Huang, X. Separator technologies for lithium-ion batteries. *Journal of Solid State Electrochemistry* **15**, 649-662 (2011). https://doi.org/10.1007/s10008-010-1264-9

34 Lu, W., Yuan, Z., Zhao, Y., Zhang, H., Zhang, H. & Li, X. Porous membranes in secondary battery technologies. *Chem Soc Rev* **46**, 2199-2236 (2017). https://doi.org/10.1039/C6CS00823B

35 Nunes-Pereira, J., Costa, C. & Lanceros-Méndez, S. Polymer composites and blends for battery separators: state of the art, challenges and future trends. *Journal of Power Sources* **281**, 378-398 (2015). https://doi.org/10.1016/j.jpowsour.2015.02.010

36 Ali, S., Tan, C., Waqas, M., Lv, W., Wei, Z., Wu, S., Boateng, B., Liu, J., Ahmed, J. & Xiong, J. Highly efficient PVDF-HFP/colloidal alumina composite separator for high-temperature lithium-ion batteries. *Advanced Materials Interfaces* **5**, 1701147 (2018). https://doi.org/10.1002/admi.201701147

37 Dai, J., Shi, C., Li, C., Shen, X., Peng, L., Wu, D., Sun, D., Zhang, P. & Zhao, J. A rational design of separator with substantially enhanced thermal features for lithium-ion batteries by the polydopamine–ceramic composite modification of polyolefin membranes. *Energy & Environmental Science* **9**, 3252-3261 (2016). https://doi.org/10.1039/C6EE01219A

38 Huang, X. Performance evaluation of a non-woven lithium ion battery separator prepared through a paper-making process. *Journal of Power Sources* **256**, 96-101 (2014). https://doi.org/10.1016/j.jpowsour.2014.01.080

39 Wang, Y., Yang, Y., Yang, Y. & Shao, H. Enhanced electrochemical performance of unique morphological LiMnPO4/C cathode material prepared by solvothermal method. *Solid State Communications* **150**, 81-85 (2010). https://doi.org/10.1016/j.ssc.2009.09.046

40 Zhong, S., Yuan, B., Guang, Z., Chen, D., Li, Q., Dong, L., Ji, Y., Dong, Y., Han, J. & He, W. Recent progress in thin separators for upgraded lithium ion batteries. *Energy Storage Materials* **41**, 805-841 (2021). https://doi.org/10.1016/j.ensm.2021.07.028

41 Waqas, M., Ali, S., Feng, C., Chen, D., Han, J. & He, W. Recent development in separators for high-temperature lithium-ion batteries. *Small* **15**, 1901689 (2019). https://doi.org/10.1002/smll.201901689

42 Li, Y., Lu, Y. X., Adelhelm, P., Titirici, M. M. & Hu, Y. S. Intercalation chemistry of graphite: alkali metal ions and beyond. *Chem Soc Rev* **48**, 4655-4687 (2019). https://doi.org/10.1039/c9cs00162j

43 Massé, R. C., Liu, C., Li, Y., Mai, L. & Cao, G. Energy storage through intercalation reactions: electrodes for rechargeable batteries. *National Science Review* **4**, 26-53 (2016). https://doi.org/10.1093/nsr/nww093

44 Whittingham, M. S. Ultimate Limits to Intercalation Reactions for Lithium Batteries. *Chemical Reviews* **114**, 11414-11443 (2014). https://doi.org/10.1021/cr5003003

45 Tarascon, J. M. & Guyomard, D. The Li1+XMn2O4/C Rocking-Chair System - a Review. *Electrochim Acta* **38**, 1221-1231 (1993). https://doi.org/10.1016/0013-4686(93)80053-3
46 Link, S., Neef, C. & Wicke, T. Trends in Automotive Battery Cell Design: A Statistical Analysis of Empirical Data. *Batteries* **9**, 261 (2023). https://doi.org/10.3390/batteries9050261
47 Smith, A., Stüble, P., Leuthner, L., Hofmann, A., Jeschull, F. & Mereacre, L. Potential and Limitations of Research Battery Cell Types for Electrochemical Data Acquisition. *Batteries Supercaps* **6** (2023). https://doi.org/10.1002/batt.202300080
48 Schwolow, S., Siddiqui, M. A. R., Bauer, P. & Vietor, T. Impact Tests and Computed Tomography Scans of Prismatic Battery Cells. *Energies* **15**, 8330 (2022). https://doi.org/10.3390/en15228330
49 Aalund, R., Endreddy, B. & Pecht, M. How Gas Generates in Pouch Cells and Affects Consumer Products. *Frontiers in Chemical Engineering* **4** (2022). https://doi.org/10.3389/fceng.2022.828375
50 Blomgren, G. E. The development and future of lithium ion batteries. *J Electrochem Soc* **164**, A5019 (2016). https://doi.org/10.1149/2.0251701jes
51 Long, B. R., Rinaldo, S. G., Gallagher, K. G., Dees, D. W., Trask, S. E., Polzin, B. J., Jansen, A. N., Abraham, D. P., Bloom, I. & Bareño, J. Enabling high-energy, high-voltage lithium-ion cells: standardization of coin-cell assembly, electrochemical testing, and evaluation of full cells. *J Electrochem Soc* **163**, A2999 (2016). https://doi.org/10.1149/2.0691614jes
52 Luc, P.-M., Bauer, S. & Kowal, J. Reproducible production of lithium-ion coin cells. *Energies* **15**, 7949 (2022). https://doi.org/10.3390/en15217949
53 Lingappan, N., Kong, L. & Pecht, M. The significance of aqueous binders in lithium-ion batteries. *Renewable and Sustainable Energy Reviews* **147**, 111227 (2021). https://doi.org/10.1016/j.rser.2021.111227
54 Burger, D., Keim, N., Shabbir, J., Gao, Y., Müller, M., Bauer, W., Hoffmann, A., Scharfer, P. & Schabel, W. Simultaneous Primer Coating for Fast Drying of Battery Electrodes. *Energy Technol-Ger* **n/a**, 2401668 (2024). https://doi.org/10.1002/ente.202401668
55 Chen, H., Ling, M., Hencz, L., Ling, H. Y., Li, G. R., Lin, Z., Liu, G. & Zhang, S. Q. Exploring Chemical, Mechanical, and Electrical Functionalities of Binders for Advanced Energy-Storage Devices. *Chemical Reviews* **118**, 8936-8982 (2018). https://doi.org/10.1021/acs.chemrev.8b00241
56 Liu, H., Cheng, X., Chong, Y., Yuan, H., Huang, J.-Q. & Zhang, Q. Advanced electrode processing of lithium ion batteries: A review of powder technology in battery fabrication. *Particuology* **57**, 56-71 (2021). https://doi.org/10.1016/j.partic.2020.12.003
57 Ndour, M., Bonnet, J.-P., Cavalaglio, S., Lombard, T., Courty, M., Aymard, L., Przybylski, C. & Bonnet, V. The formulation of a CMC binder/silicon composite anode for Li-ion batteries: from molecular effects of ball milling on polymer chains to consequences on electrochemical performances. *Materials Advances* **3**, 8522-8533 (2022). https://doi.org/10.1039/D2MA00702A
58 Stefanovic, B., Pirker, K. F., Rosenau, T. & Potthast, A. Effects of tribochemical treatments on the integrity of cellulose. *Carbohydrate polymers* **111**, 688-699 (2014). https://doi.org/10.1016/j.carbpol.2014.05.011
59 Ishii, M., Makino, S. & Nakamura, H. The role of carboxymethyl cellulose on the rheology of anode slurries in lithium-ion batteries. *Current Opinion in Colloid & Interface Science* **74**, 101858 (2024). https://doi.org/10.1016/j.cocis.2024.101858
60 Burger, D., Klemens, J., Keim, N., Müller, M., Bauer, W., Schmatz, J., Kumberg, J., Scharfer, P. & Schabel, W. Additive Influence on Binder Migration in Electrode Drying. *Energy Technol-Ger* **12** (2024). https://doi.org/10.1002/ente.202400057

61 Jaiser, S., Müller, M., Baunach, M., Bauer, W., Scharfer, P. & Schabel, W. Investigation of film solidification and binder migration during drying of Li-Ion battery anodes. *Journal of Power Sources* **318**, 210-219 (2016). https://doi.org/10.1016/j.jpowsour.2016.04.018

62 Kumberg, J., Bauer, W., Schmatz, J., Diehm, R., Tönsmann, M., Müller, M., Ly, K., Scharfer, P. & Schabel, W. Reduced drying time of anodes for lithium-ion batteries through simultaneous multilayer coating. *Energy Technol-Ger* **9**, 2100367 (2021). https://doi.org/10.1002/ente.202100367

63 Morasch, R., Landesfeind, J., Suthar, B. & Gasteiger, H. A. Detection of binder gradients using impedance spectroscopy and their influence on the tortuosity of Li-ion battery graphite electrodes. *J Electrochem Soc* **165**, A3459-A3467 (2018). https://doi.org/10.1149/2.1021814jes

64 Lestriez, B., Bahri, S., Sandu, I., Roué, L. & Guyomard, D. On the binding mechanism of CMC in Si negative electrodes for Li-ion batteries. *Electrochemistry Communications* **9**, 2801-2806 (2007). https://doi.org/10.1016/j.elecom.2007.10.001

65 Sung, S. H., Kim, S., Park, J. H., Park, J. D. & Ahn, K. H. Role of PVDF in rheology and microstructure of NCM cathode slurries for lithium-ion battery. *Materials* **13**, 4544 (2020). https://doi.org/10.3390/ma13204544

66 Wang, N., NuLi, Y., Su, S., Yang, J. & Wang, J. Effects of binders on the electrochemical performance of rechargeable magnesium batteries. *Journal of Power Sources* **341**, 219-229 (2017). https://doi.org/10.1016/j.jpowsour.2016.12.003

67 Weber, A., Keim, N., Gyulai, A., Mueller, M., Colombo, F., Bauer, W. & Ehrenberg, H. The Role of Surface Free Energy in Binder Distribution and Adhesion Strength of Aqueously Processed LiNiMnO Cathodes. *J Electrochem Soc* **171** (2024). https://doi.org/10.1149/1945-7111/ad3a24

68 Klemens, J., Schneider, L., Herbst, E. C., Bohn, N., Müller, M., Bauer, W., Scharfer, P. & Schabel, W. Drying of NCM cathode electrodes with porous, nanostructured particles versus compact solid particles: comparative study of binder migration as a function of drying conditions. *Energy Technol-Ger* **10**, 2100985 (2022). https://doi.org/10.1002/ente.202100985

69 Müller, M., Pfaffmann, L., Jaiser, S., Baunach, M., Trouillet, V., Scheiba, F., Scharfer, P., Schabel, W. & Bauer, W. Investigation of binder distribution in graphite anodes for lithium-ion batteries. *Journal of Power Sources* **340**, 1-5 (2017). https://doi.org/10.1016/j.jpowsour.2016.11.051

70 Yoo, M., Frank, C. W., Mori, S. & Yamaguchi, S. Effect of poly(vinylidene fluoride) binder crystallinity and graphite structure on the mechanical strength of the composite anode in a lithium ion battery. *Polymer* **44**, 4197-4204 (2003). https://doi.org/10.1016/S0032-3861(03)00364-1

71 Lux, S., Schappacher, F., Balducci, A., Passerini, S. & Winter, M. Low cost, environmentally benign binders for lithium-ion batteries. *J Electrochem Soc* **157**, A320 (2010). https://doi.org/10.1149/1.3291976

72 Biensan, P., Simon, B., Pérès, J. P., de Guibert, A., Broussely, M., Bodet, J. M. & Perton, F. On safety of lithium-ion cells. *Journal of Power Sources* **81-82**, 906-912 (1999). https://doi.org/10.1016/S0378-7753(99)00135-4

73 Zhang, S., Xu, K. & Jow, T. Poly (acrylonitrile-methyl methacrylate) as a non-fluorinated binder for the graphite anode of Li-ion batteries. *Journal of applied electrochemistry* **33**, 1099-1101 (2003). https://doi.org/10.1023/A:1026225001109

74 Maleki, H., Deng, G., Anani, A. & Howard, J. Thermal stability studies of Li-ion cells and components. *J Electrochem Soc* **146**, 3224 (1999). https://doi.org/10.1149/1.1392458

75 Lee, K., Chromey, N., Culik, R., Barnes, J. & Schneider, P. Toxicity of N-methyl-2-pyrrolidone (NMP): teratogenic, subchronic, and two-year inhalation studies.

Fundamental and Applied Toxicology **9**, 222-235 (1987). https://doi.org/10.1016/0272-0590(87)90045-5

76 Malek, D., Malley, L., Slone, T., Elliott, G., Kennedy, G., Mellert, W., Deckardt, K., Gembardt, C., Hildebrand, B. & Murphy, S. Repeated dose toxicity study (28 days) in rats and mice with N-methylpyrrolidone (NMP). *Drug and Chemical Toxicology* **20**, 63-77 (1997). https://doi.org/10.3109/01480549709011079

77 Zhu, W., Schmehl, D. R., Mullin, C. A. & Frazier, J. L. Four common pesticides, their mixtures and a formulation solvent in the hive environment have high oral toxicity to honey bee larvae. *PloS one* **9**, e77547 (2014). https://doi.org/10.1371/journal.pone.0077547

78 Lee, J.-H., Lee, S., Paik, U. & Choi, Y.-M. Aqueous processing of natural graphite particulates for lithium-ion battery anodes and their electrochemical performance. *Journal of Power Sources* **147**, 249-255 (2005). https://doi.org/10.1016/j.jpowsour.2005.01.022

79 Rahman, M. S., Hasan, M. S., Nitai, A. S., Nam, S., Karmakar, A. K., Ahsan, M. S., Shiddiky, M. J. A. & Ahmed, M. B. Recent Developments of Carboxymethyl Cellulose. *Polymers-Basel* **13** (2021).

80 Balser, K., Gerhartz, W., Yamamoto, Y. S., Campbell, F. T., Pfefferkorn, R., Rounsaville, J. F. & Ullmann, F. *Ullmann's encyclopedia of industrial chemistry*. 5th, completely rev. edn, 461 (VCH, 1985).

81 Heinze, T. & Pfeiffer, K. Studies on the synthesis and characterization of carboxymethylcellulose. *Angew Makromol Chem* **266**, 37-45 (1999). https://doi.org/10.1002/(SICI)1522-9505(19990501)266:1<37::AID-APMC37>3.0.CO;2-Z

82 Kästner, U., Hoffmann, H., Do¨nges, R. & Hilbig, J. Structure and solution properties of sodium carboxymethyl cellulose. *Colloids and Surfaces A: Physicochemical and Engineering Aspects* **123-124**, 307-328 (1997). https://doi.org/10.1016/S0927-7757(96)03786-7

83 Baran, A., Sulukan, E., Türkoğlu, M., Ghosigharehagaji, A., Yildirim, S., Kankaynar, M., Bolat, I., Kaya, M., Topal, A. & Ceyhun, S. B. Is sodium carboxymethyl cellulose (CMC) really completely innocent? It may be triggering obesity. *International Journal of Biological Macromolecules* **163**, 2465-2473 (2020). https://doi.org/10.1016/j.ijbiomac.2020.09.169

84 Younes, M., Aggett, P., Aguilar, F., Crebelli, R., Di Domenico, A., Dusemund, B., Filipic, M., Frutos, M. J., Galtier, P., Gott, D., Gundert-Remy, U., Kuhnle, G. G., Lambré, C., Leblanc, J. C., Lillegaard, I. T., Moldeus, P., Mortensen, A., Oskarsson, A., Stankovic, I., Tobback, P., Waalkens-Berendsen, I., Wright, M., Tard, A., Tasiopoulou, S., Woutersen, R. A. & Nutrient, E. P. F. A. Re-evaluation of celluloses E 460(i), E 460(ii), E 461, E 462, E 463, E 464, E 465, E 466, E 468 and E 469 as food additives. *Efsa J* **16** (2018). https://doi.org/10.2903/j.efsa.2018.5047

85 Younes, M., Aquilina, G., Castle, L., Degen, G., Engel, K. H., Fowler, P. J., Fernandez, M. J. F., Fuerst, P., Guertler, R., Husoy, T., Manco, M., Mennes, W., Moldeus, P., Passamonti, S., Shah, R. M. A., Waalkens-Berendsen, I., Wright, M., Dusemund, B., Mortensen, A., Turck, D., Woelfle, D., Barmaz, S., Mech, A., Rincon, A. M., Tard, A., Vianello, G. & Gundert-Remy, U. Opinion on the re-evaluation of sodium carboxy methyl cellulose (E 466) as a food additive in foods for infants below 16 weeks of age and follow-up of its re-evaluation as food additive for uses in foods for all population groups. *Efsa J* **20** (2022). https://doi.org/10.2903/j.efsa.2022.7665

86 Aliu, A. O., Guo, J., Wang, S. & Zhao, X. Hydraulic fracture fluid for gas reservoirs in petroleum engineering applications using sodium carboxy methyl cellulose as gelling

agent. *Journal of Natural Gas Science and Engineering* **32**, 491-500 (2016). https://doi.org/10.1016/j.jngse.2016.03.064

87 Kukrety, A., Singh, R. K., Singh, P. & Ray, S. S. Comprehension on the Synthesis of Carboxymethylcellulose (CMC) Utilizing Various Cellulose Rich Waste Biomass Resources. *Waste and Biomass Valorization* **9**, 1587-1595 (2018). https://doi.org/10.1007/s12649-017-9903-3

88 Palmer, D., Levina, M., Nokhodchi, A., Douroumis, D., Farrell, T. & Rajabi-Siahboomi, A. The Influence of Sodium Carboxymethylcellulose on Drug Release from Polyethylene Oxide Extended Release Matrices. *Aaps Pharmscitech* **12**, 862-871 (2011). https://doi.org/10.1208/s12249-011-9648-4

89 Zhang, L., Sun, H., Han, B., Peng, L., Ning, F., Jiang, G. & Chehotkin, V. F. Effect of shearing actions on the rheological properties and mesostructures of CMC, PVP and CMC+PVP aqueous solutions as simple water-based drilling fluids for gas hydrate drilling. *Journal of Unconventional Oil and Gas Resources* **14**, 86-98 (2016). https://doi.org/10.1016/j.juogr.2016.02.002

90 Mondal, M. I. H., Yeasmin, M. S. & Rahman, M. S. Preparation of food grade carboxymethyl cellulose from corn husk agrowaste. *International Journal of Biological Macromolecules* **79**, 144-150 (2015). https://doi.org/10.1016/j.ijbiomac.2015.04.061

91 Veeramachineni, A. K., Sathasivam, T., Muniyandy, S., Janarthanan, P., Langford, S. J. & Yan, L. Y. Optimizing Extraction of Cellulose and Synthesizing Pharmaceutical Grade Carboxymethyl Sago Cellulose from Malaysian Sago Pulp. *Applied Sciences* **6** (2016).

92 Yao, Y., Sun, Z., Li, X., Tang, Z., Li, X., Morrell, J. J., Liu, Y., Li, C. & Luo, Z. Effects of Raw Material Source on the Properties of CMC Composite Films. *Polymers-Basel* **14**, 32 (2022). https://doi.org/10.3390/polym14010032

93 K. Kimani, P., G. Kareru, P., E. Madivoli, S., K. Kairigo, P., G. Maina, E. & S. Rechab, O. Comparative Study of Carboxymethyl Cellulose Synthesis from Selected Kenyan Biomass. *Chemical Science International Journal* **17**, 1-8 (2016). https://doi.org/10.9734/CSJI/2016/29390

94 Singh, R. K. & Singh, A. K. Optimization of Reaction Conditions for Preparing Carboxymethyl Cellulose from Corn Cobic Agricultural Waste. *Waste and Biomass Valorization* **4**, 129-137 (2013). https://doi.org/10.1007/s12649-012-9123-9

95 Ramakrishnan, R., Kim, J. T., Roy, S. & Jayakumar, A. Recent advances in carboxymethyl cellulose-based active and intelligent packaging materials: A comprehensive review. *International Journal of Biological Macromolecules* **259**, 129194 (2024). https://doi.org/10.1016/j.ijbiomac.2023.129194

96 Wahyuni, H. S., Yuliasmi, S., Aisyah, H. S. & Riati, D. Characterization of Synthesized Sodium Carboxymethyl Cellulose with Variation of Solvent Mixture and Alkali Concentration. *Open Access Maced J Med Sci* **7**, 3878-3881 (2019). https://doi.org/10.3889/oamjms.2019.524

97 Kokol, V. Influence of hydroxyethyl and carboxymethyl celluloses on the rheology, water retention and surface tension of water-suspended microfibrillated cellulose. *Cellulose* **29**, 7063-7081 (2022). https://doi.org/10.1007/s10570-022-04737-w

98 Ferro, M., Mannu, A., Panzeri, W., Theeuwen, C. H. J. & Mele, A. An Integrated Approach to Optimizing Cellulose Mercerization. *Polymers-Basel* **12**, 1559 (2020). https://doi.org/10.3390/polym12071559

99 Lin, Q., Huang, Y. & Yu, W. An in-depth study of molecular and supramolecular structures of bamboo cellulose upon heat treatment. *Carbohydrate Polymers* **241**, 116412 (2020). https://doi.org/10.1016/j.carbpol.2020.116412

100 Sawada, D., Nishiyama, Y., Shah, R., Forsyth, V. T., Mossou, E., O'Neill, H. M., Wada, M. & Langan, P. Untangling the threads of cellulose mercerization. *Nature Communications* **13**, 6189 (2022). https://doi.org/10.1038/s41467-022-33812-w

101 Solhi, L., Guccini, V., Heise, K., Solala, I., Niinivaara, E., Xu, W., Mihhels, K., Kröger, M., Meng, Z., Wohlert, J., Tao, H., Cranston, E. D. & Kontturi, E. Understanding Nanocellulose–Water Interactions: Turning a Detriment into an Asset. *Chemical Reviews* **123**, 1925-2015 (2023). https://doi.org/10.1021/acs.chemrev.2c00611

102 Mann, G., Kunze, J., Loth, F. & Fink, H.-P. Cellulose ethers with a block-like distribution of the substituents by structure-selective derivatization of cellulose. *Polymer* **39**, 3155-3165 (1998). https://doi.org/10.1016/S0032-3861(97)10006-4

103 Park, J.-H. Carboxymethyl cellulose-based binder material and lithium battery using the same. United States of America patent (2004).

104 Pensini, E., Yip, C. M., O'Carroll, D. & Sleep, B. E. Carboxymethyl cellulose binding to mineral substrates: Characterization by atomic force microscopy–based Force spectroscopy and quartz-crystal microbalance with dissipation monitoring. *Journal of Colloid and Interface Science* **402**, 58-67 (2013). https://doi.org/10.1016/j.jcis.2013.03.053

105 Costa, E. M., Pereira, C. F., Ribeiro, A. A., Casanova, F., Freixo, R., Pintado, M. & Ramos, O. L. Characterization and Evaluation of Commercial Carboxymethyl Cellulose Potential as an Active Ingredient for Cosmetics. *Applied Sciences* **12**, 6560 (2022). https://doi.org/10.3390/app12136560

106 Keim, N., Weber, A., Müller, M., Kaufmann, U., Bauer, W., Petermann, O., Bayer, R. & Ehrenberg, H. Understanding Key NaCMC Properties to Optimize Electrodes and Battery Performance. *Advanced Energy and Sustainability Research* **6**, 2400364 (2025). https://doi.org/10.1002/aesr.202400364

107 Eyjolfsson, R. in *Design and Manufacture of Pharmaceutical Tablets* (ed Reynir Eyjolfsson) 29-41 (Academic Press, 2015).

108 Rowe, R. C., Sheskey, P. J., Owen, S. n. C. & American Pharmacists Association. *Handbook of pharmaceutical excipients / edited by Raymond C. Rowe, Paul J. Sheskey, Marian E. Quinn*. 6th edn, (APhA/Pharmaceutical Press ;, 2009).

109 Zarmpi, P., Flanagan, T., Meehan, E., Mann, J. & Fotaki, N. Biopharmaceutical aspects and implications of excipient variability in drug product performance. *European Journal of Pharmaceutics and Biopharmaceutics* **111**, 1-15 (2017). https://doi.org/10.1016/j.ejpb.2016.11.004

110 *Handbook of pharmaceutical wet granulation : theory and practice in a quality by design paradigm*. 1st edition. edn, (Academic Press an imprint of Elsevier, 2019).

111 Li, B. R., Chao, Y., Li, M. C., Xiao, Y. B., Li, R., Yang, K., Cui, X. C., Xu, G., Li, L. Y., Yang, C. K., Yu, Y., Wilkinson, D. P. & Zhang, J. J. A Review of Solid Electrolyte Interphase (SEI) and Dendrite Formation in Lithium Batteries. *Electrochem Energy R* **6** (2023). https://doi.org/10.1007/s41918-022-00147-5

112 Wang, A. P., Kadam, S., Li, H., Shi, S. Q. & Qi, Y. Review on modeling of the anode solid electrolyte interphase (SEI) for lithium-ion batteries. *Npj Comput Mater* **4** (2018). https://doi.org/10.1038/s41524-018-0064-0

113 Cheng, X.-B., Yan, C., Zhang, X.-Q., Liu, H. & Zhang, Q. Electronic and Ionic Channels in Working Interfaces of Lithium Metal Anodes. *ACS Energy Letters* **3**, 1564-1570 (2018). https://doi.org/10.1021/acsenergylett.8b00526

114 Shi, S., Lu, P., Liu, Z., Qi, Y., Hector, L. G., Jr., Li, H. & Harris, S. J. Direct Calculation of Li-Ion Transport in the Solid Electrolyte Interphase. *J Am Chem Soc* **134**, 15476-15487 (2012). https://doi.org/10.1021/ja305366r

115 Yan, C., Xu, R., Xiao, Y., Ding, J. F., Xu, L., Li, B. Q. & Huang, J. Q. Toward Critical Electrode/Electrolyte Interfaces in Rechargeable Batteries. *Adv Funct Mater* **30** (2020). https://doi.org/10.1002/adfm.201909887

116 Goodenough, J. B. & Kim, Y. Challenges for Rechargeable Li Batteries. *Chemistry of Materials* **22**, 587-603 (2010). https://doi.org/10.1021/cm901452z

117 Gauthier, M., Carney, T. J., Grimaud, A., Giordano, L., Pour, N., Chang, H.-H., Fenning, D. P., Lux, S. F., Paschos, O., Bauer, C., Maglia, F., Lupart, S., Lamp, P. & Shao-Horn, Y. Electrode–Electrolyte Interface in Li-Ion Batteries: Current Understanding and New Insights. *The Journal of Physical Chemistry Letters* **6**, 4653-4672 (2015). https://doi.org/10.1021/acs.jpclett.5b01727

118 Hou, J. B., Yang, M., Wang, D. Y. & Zhang, J. L. Fundamentals and Challenges of Lithium Ion Batteries at Temperatures between-40 and 60 °C. *Adv Energy Mater* **10** (2020). https://doi.org/10.1002/aenm.201904152

119 Peled, E. & Menkin, S. Review-SEI: Past, Present and Future. *J Electrochem Soc* **164**, A1703-A1719 (2017). https://doi.org/10.1149/2.1441707jes

120 Fang, C., Tran, T. N., Zhao, Y. Z. & Liu, G. Electrolyte decomposition and solid electrolyte interphase revealed by mass spectrometry. *Electrochim Acta* **399** (2021). https://doi.org/10.1016/j.electacta.2021.139362

121 Gachot, G., Ribière, P., Mathiron, D., Grugeon, S., Armand, M., Leriche, J.-B., Pilard, S. & Laruelle, S. Gas Chromatography/Mass Spectrometry As a Suitable Tool for the Li-Ion Battery Electrolyte Degradation Mechanisms Study. *Analytical Chemistry* **83**, 478-485 (2011). https://doi.org/10.1021/ac101948u

122 Nie, M., Chalasani, D., Abraham, D. P., Chen, Y., Bose, A. & Lucht, B. L. Lithium Ion Battery Graphite Solid Electrolyte Interphase Revealed by Microscopy and Spectroscopy. *The Journal of Physical Chemistry C* **117**, 1257-1267 (2013). https://doi.org/10.1021/jp3118055

123 Strehle, B., Solchenbach, S., Metzger, M., Schwenke, K. U. & Gasteiger, H. A. The Effect of CO on Alkyl Carbonate Trans-Esterification during Formation of Graphite Electrodes in Li-Ion Batteries. *J Electrochem Soc* **164**, A2513-A2526 (2017). https://doi.org/10.1149/2.1001712jes

124 Aurbach, D. Review of selected electrode–solution interactions which determine the performance of Li and Li ion batteries. *Journal of Power Sources* **89**, 206-218 (2000). https://doi.org/10.1016/S0378-7753(00)00431-6

125 Leroy, S., Blanchard, F., Dedryvère, R., Martinez, H., Carré, B., Lemordant, D. & Gonbeau, D. Surface film formation on a graphite electrode in Li-ion batteries:: AFM and XPS study. *Surf Interface Anal* **37**, 773-781 (2005). https://doi.org/10.1002/sia.2072

126 Leroy, S., Martinez, H., Dedryvère, R., Lemordant, D. & Gonbeau, D. Influence of the lithium salt nature over the surface film formation on a graphite electrode in Li-ion batteries: An XPS study. *Applied Surface Science* **253**, 4895-4905 (2007). https://doi.org/10.1016/j.apsusc.2006.10.071

127 Eriksson, T., Andersson, A. M., Bishop, A. G., Gejke, C., Gustafsson, T. & Thomas, J. O. Surface analysis of LiMnO electrodes in carbonate-based electrolytes. *J Electrochem Soc* **149**, A69-A78 (2002). https://doi.org/10.1149/1.1426398

128 Borodin, O., Olguin, M., Spear, C. E., Leiter, K. W. & Knap, J. Towards high throughput screening of electrochemical stability of battery electrolytes. *Nanotechnology* **26** (2015). https://doi.org/10.1088/0957-4484/26/35/354003

129 Wang, Y., Nakamura, S., Ue, M. & Balbuena, P. B. Theoretical Studies To Understand Surface Chemistry on Carbon Anodes for Lithium-Ion Batteries: Reduction Mechanisms of Ethylene Carbonate. *J Am Chem Soc* **123**, 11708-11718 (2001). https://doi.org/10.1021/ja0164529

130 Aurbach, D., Gofer, Y., Ben-Zion, M. & Aped, P. The behaviour of lithium electrodes in propylene and ethylene carbonate: Te major factors that influence Li cycling efficiency. *Journal of Electroanalytical Chemistry* **339**, 451-471 (1992). https://doi.org/10.1016/0022-0728(92)80467-I

131 Zhuang, G. V., Xu, K., Yang, H., Jow, T. R. & Ross, P. N. Lithium Ethylene Dicarbonate Identified as the Primary Product of Chemical and Electrochemical Reduction of EC in

1.2 M LiPF6/EC:EMC Electrolyte. *The Journal of Physical Chemistry B* **109**, 17567-17573 (2005). https://doi.org/10.1021/jp052474w

132 Broussely, M., Biensan, P., Bonhomme, F., Blanchard, P., Herreyre, S., Nechev, K. & Staniewicz, R. J. Main aging mechanisms in Li ion batteries. *Journal of Power Sources* **146**, 90-96 (2005). https://doi.org/10.1016/j.jpowsour.2005.03.172

133 Herstedt, M., Abraham, D. P., Kerr, J. B. & Edström, K. X-ray photoelectron spectroscopy of negative electrodes from high-power lithium-ion cells showing various levels of power fade. *Electrochim Acta* **49**, 5097-5110 (2004). https://doi.org/10.1016/j.electacta.2004.06.021

134 Vetter, J., Novák, P., Wagner, M. R., Veit, C., Möller, K. C., Besenhard, J. O., Winter, M., Wohlfahrt-Mehrens, M., Vogler, C. & Hammouche, A. Ageing mechanisms in lithium-ion batteries. *Journal of Power Sources* **147**, 269-281 (2005). https://doi.org/10.1016/j.jpowsour.2005.01.006

135 Seo, D. M., Chalasani, D., Parimalam, B. S., Kadam, R., Nie, M. Y. & Lucht, B. L. Reduction Reactions of Carbonate Solvents for Lithium Ion Batteries. *Ecs Electrochem Lett* **3**, A91-A93 (2014). https://doi.org/10.1149/2.0021409eel

136 Ponomar, M., Krasnyuk, E., Butylskii, D., Nikonenko, V., Wang, Y., Jiang, C., Xu, T. & Pismenskaya, N. Sessile Drop Method: Critical Analysis and Optimization for Measuring the Contact Angle of an Ion-Exchange Membrane Surface. *Membranes* **12**, 765 (2022). https://doi.org/10.3390/membranes12080765

137 Huhtamäki, T., Tian, X., Korhonen, J. T. & Ras, R. H. A. Surface-wetting characterization using contact-angle measurements. *Nature Protocols* **13**, 1521-1538 (2018). https://doi.org/10.1038/s41596-018-0003-z

138 Erbil, H. Y. The debate on the dependence of apparent contact angles on drop contact area or three-phase contact line: A review. *Surface Science Reports* **69**, 325-365 (2014). https://doi.org/10.1016/j.surfrep.2014.09.001

139 Young, T. III. An essay on the cohesion of fluids. *Philosophical Transactions of the Royal Society of London* **95**, 65-87 (1805). https://doi.org/doi:10.1098/rstl.1805.0005

140 Berezina, N. P., Kononenko, N. A., Dyomina, O. A. & Gnusin, N. P. Characterization of ion-exchange membrane materials: Properties vs structure. *Advances in Colloid and Interface Science* **139**, 3-28 (2008). https://doi.org/10.1016/j.cis.2008.01.002

141 Cassie, A. B. D. Contact angles. *Discussions of the Faraday Society* **3**, 11-16 (1948). https://doi.org/10.1039/DF9480300011

142 Wenzel, R. N. RESISTANCE OF SOLID SURFACES TO WETTING BY WATER. *Industrial & Engineering Chemistry* **28**, 988-994 (1936). https://doi.org/10.1021/ie50320a024

143 Marmur, A. Solid-Surface Characterization by Wetting. *Annual Review of Materials Research* **39**, 473-489 (2009). https://doi.org/10.1146/annurev.matsci.38.060407.132425

144 International Symposium on Contact Angle, W., Adhesion, International Symposium on Contact Angle, W., Adhesion, Mittal, K. L., International Symposium on Contact Angle, W. & Adhesion. *Contact angle, wettability and adhesion*. (VSP, 2009).

145 Cassie, A. B. D. & Baxter, S. Wettability of porous surfaces. *Transactions of the Faraday Society* **40**, 546-551 (1944). https://doi.org/10.1039/TF9444000546

146 Dupré, A. & Dupré, P. C. d. E. *Théorie mécanique de la Chaleur. Par ... A. D. ... (Partie expérimentale en commun avec ... P. Dupré.)*. (1869).

147 Schrader, M. E. Young-Dupre Revisited. *Langmuir* **11**, 3585-3589 (1995). https://doi.org/10.1021/la00009a049

148 Adam, N. K. The physics and chemistry of surfaces. (1941).

149 Fowkes, F. M. DETERMINATION OF INTERFACIAL TENSIONS, CONTACT ANGLES, AND DISPERSION FORCES IN SURFACES BY ASSUMING

ADDITIVITY OF INTERMOLECULAR INTERACTIONS IN SURFACES. *The Journal of Physical Chemistry* **66**, 382-382 (1962). https://doi.org/10.1021/j100808a524

150 Fowkes, F. M. ATTRACTIVE FORCES AT INTERFACES. *Industrial & Engineering Chemistry* **56**, 40-52 (1964). https://doi.org/10.1021/ie50660a008

151 Fowkes, F. M. Donor-Acceptor Interactions at Interfaces. *The Journal of Adhesion* **4**, 155-159 (1972). https://doi.org/10.1080/00218467208072219

152 Law, K.-Y., Zhao, H. & SpringerLink. *Surface Wetting : Characterization, Contact Angle, and Fundamentals*. 1st 2016. edn, (Springer International Publishing : Imprint: Springer, 2015).

153 Kaelble, D. H. Dispersion-Polar Surface Tension Properties of Organic Solids. *The Journal of Adhesion* **2**, 66-81 (1970). https://doi.org/10.1080/0021846708544582

154 Owens, D. K. & Wendt, R. C. Estimation of the surface free energy of polymers. *Journal of Applied Polymer Science* **13**, 1741-1747 (1969). https://doi.org/10.1002/app.1969.070130815

155 Rabel, W. Einige Aspekte der Benetzungstheorie und ihre Anwendung auf die Untersuchung und Veränderung der Oberflächeneigenschaften von Polymeren. *Farbe und Lack* **77**, 997-1005 (1971).

156 Matavž, A., Bobnar, V. & Malič, B. Tailoring Ink–Substrate Interactions via Thin Polymeric Layers for High-Resolution Printing. *Langmuir* **33**, 11893-11900 (2017). https://doi.org/10.1021/acs.langmuir.7b02181

157 Weber, A. K., N.; Koch, P.; Müller, M.; Bauer, W.; Ehrenberg, H. The Impact of Binder Polarity on the Properties of Aqueously Processed Positive and Negative Electrodes for Lithium-Ion Batteries. *Nature Scientific Reports* **15**, 10024 (2025). https://doi.org/10.1038/s41598-025-93813-9

158 Van Oss, C. J. *Interfacial forces in aqueous media*. 2nd edn, (Taylor & Francis, 2006).

159 Van Oss, C. J., Good, R. J. & Chaudhury, M. K. The role of van der Waals forces and hydrogen bonds in "hydrophobic interactions" between biopolymers and low energy surfaces. *Journal of Colloid and Interface Science* **111**, 378-390 (1986). https://doi.org/10.1016/0021-9797(86)90041-X

160 Van Oss, C. J., Ju, L., Chaudhury, M. K. & Good, R. J. Estimation of the polar parameters of the surface tension of liquids by contact angle measurements on gels. *Journal of Colloid and Interface Science* **128**, 313-319 (1989). https://doi.org/10.1016/0021-9797(89)90345-7

161 Van Oss, C. J., Good, R. J. & Chaudhury, M. K. Additive and nonadditive surface tension components and the interpretation of contact angles. *Langmuir* **4**, 884-891 (1988). https://doi.org/10.1021/la00082a018

162 van Oss, C. J. & Good, R. J. On the Mechanism of "Hydrophobic" Interactions. *Journal of Dispersion Science and Technology* **9**, 355-362 (1988). https://doi.org/10.1080/01932698808943994

163 Chaudhury, M. K. Interfacial interaction between low-energy surfaces. *Materials Science and Engineering: R: Reports* **16**, 97-159 (1996). https://doi.org/10.1016/0927-796X(95)00185-9

164 van Oss, C. J., Visser, J., Absolom, D. R., Omenyi, S. N. & Neumann, A. W. The concept of negative hamaker coefficients, II. Thermodynamics, experimental evidence and applications. *Advances in Colloid and Interface Science* **18**, 133-148 (1983). https://doi.org/10.1016/0001-8686(83)87001-8

165 Marmur, A. Solid-Surface Characterization by Wetting. *Annu Rev Mater Res* **39**, 473-489 (2009). https://doi.org/10.1146/annurev.matsci.38.060407.132425

166 Decker, E. L. & Garoff, S. Using vibrational noise to probe energy barriers producing contact angle hysteresis. *Langmuir* **12**, 2100-2110 (1996). https://doi.org/10.1021/la951021n

167 Etzler, F. M. Determination of the surface free energy of solids: A critical review. *Reviews of Adhesion and Adhesives* **1** (2013). https://doi.org/10.7569/RAA.2013.097301
168 Cazaux, J. Recent developments and new strategies in scanning electron microscopy. *J Microsc-Oxford* **217**, 16-35 (2005). https://doi.org/10.1111/j.0022-2720.2005.01414.x
169 Goldstein, J. I., Newbury, D. E., Michael, J. R., Ritchie, N. W., Scott, J. H. J. & Joy, D. C. *Scanning electron microscopy and X-ray microanalysis*. (springer, 2017).
170 Mahltig, B. & Grethe, T. High-performance and functional fiber materials—a review of properties, scanning electron microscopy SEM and electron dispersive spectroscopy EDS. *Textiles* **2**, 209-251 (2022). https://doi.org/10.3390/textiles2020012
171 Mlynárik, V. Introduction to nuclear magnetic resonance. *Analytical Biochemistry* **529**, 4-9 (2017). https://doi.org/10.1016/j.ab.2016.05.006
172 Washburn, E. W. The Dynamics of Capillary Flow. *Physical Review* **17**, 273-283 (1921). https://doi.org/10.1103/PhysRev.17.273
173 Susana, L., Campaci, F. & Santomaso, A. C. Wettability of mineral and metallic powders: Applicability and limitations of sessile drop method and Washburn's technique. *Powder Technology* **226**, 68-77 (2012). https://doi.org/10.1016/j.powtec.2012.04.016
174 van Oss, C. J., Giese, R. F., Li, Z., Murphy, K., Norris, J., Chaudhury, M. K. & Good, R. J. Determination of Contact Angles and Pore Sizes of Porous-Media by Column and Thin-Layer Wicking. *J Adhes Sci Technol* **6**, 413-428 (1992). https://doi.org/10.1163/156856192x00755
175 Fischer, K. Neues Verfahren zur maßanalytischen Bestimmung des Wassergehaltes von Flüssigkeiten und festen Körpern. *Angewandte Chemie* **48** (1935). https://doi.org/10.1002/ange.19350482605
176 Rivera-Quintero, P., Patience, G. S., Patience, N. A., Boffito, D. C., Banquy, X. & Schieppati, D. Experimental methods in chemical engineering: Karl Fischer titration. *Can J Chem Eng* **102**, 2980-2997 (2024). https://doi.org/10.1002/cjce.25295
177 Grünke, S. The influence of conductivity on the Karl Fischer titration. *Food chemistry* **82**, 99-105 (2003). https://doi.org/10.1016/S0308-8146(02)00544-7
178 Isengard, H.-D., Kling, R. & Reh, C. Proposal of a new reference method to determine the water content of dried dairy products. *Food chemistry* **96**, 418-422 (2006). https://doi.org/10.1016/j.foodchem.2004.12.046
179 Larsson, W., Panitz, J.-C. & Cedergren, A. Interference-free coulometric titration of water in lithium bis(oxalato)borate using Karl Fischer reagents based on N-methylformamide. *Talanta* **69**, 276-280 (2006). https://doi.org/10.1016/j.talanta.2005.10.004
180 Eser, J. C., Deichmann, B., Wirsching, T., Merklein, L., Müller, M., Scharfer, P. & Schabel, W. Diffusion kinetics of water in graphite anodes for Li-ion batteries. *Drying Technology* **40**, 1130-1145 (2022). https://doi.org/10.1080/07373937.2020.1852568
181 Eser, J. C., Wirsching, T., Weidler, P. G., Altvater, A., Börnhorst, T., Kumberg, J., Schöne, G., Müller, M., Scharfer, P. & Schabel, W. Moisture adsorption behavior in anodes for Li-ion batteries. *Energy Technol-Ger* **8**, 1801162 (2020). https://doi.org/10.1002/ente.201801162
182 Kosfeld, M., Westphal, B. & Kwade, A. Correct water content measuring of lithium-ion battery components and the impact of calendering via Karl-Fischer titration. *Journal of Energy Storage* **51**, 104398 (2022). https://doi.org/10.1016/j.est.2022.104398
183 Leroy, S., Blanchard, F., Dedryvère, R., Martinez, H., Carré, B., Lemordant, D. & Gonbeau, D. Surface film formation on a graphite electrode in Li-ion batteries: AFM and XPS study. *Surf Interface Anal* **37**, 773-781 (2005). https://doi.org/10.1002/sia.2072
184 Verma, P., Maire, P. & Novák, P. A review of the features and analyses of the solid electrolyte interphase in Li-ion batteries. *Electrochim Acta* **55**, 6332-6341 (2010). https://doi.org/10.1016/j.electacta.2010.05.072

185 Rinkel, B. L. D., Hall, D. S., Temprano, I. & Grey, C. P. Electrolyte Oxidation Pathways in Lithium-Ion Batteries. *J Am Chem Soc* **142**, 15058-15074 (2020). https://doi.org/10.1021/jacs.0c06363

186 Rinkel, B. L. D., Vivek, J. P., Garcia-Araez, N. & Grey, C. P. Two electrolyte decomposition pathways at nickel-rich cathode surfaces in lithium-ion batteries. *Energy & Environmental Science* **15**, 3416-3438 (2022). https://doi.org/10.1039/d1ee04053g

187 Aurbach, D. in *Nonaqueous Electrochemistry* 289-411 (Marcel Dekker, 1999).

188 Hayashi, K., Nemoto, Y., Tobishima, S.-i. & Yamaki, J.-i. Mixed solvent electrolyte for high voltage lithium metal secondary cells. *Electrochim Acta* **44**, 2337-2344 (1999). https://doi.org/10.1016/S0013-4686(98)00374-0

189 Zhang, X. R., Kostecki, R., Richardson, T. J., Pugh, J. K. & Ross, P. N. Electrochemical and infrared studies of the reduction of organic carbonates. *J Electrochem Soc* **148**, A1341-A1345 (2001). https://doi.org/10.1149/1.1415547

190 Klamet, T. Determination of gel particle content in CMC for battery applications: Visual assessment of a wet film. (DDP Specialty Products Germany GmbH & Co. KG, 2023).

191 DIN ISO 813:2020-12: Rubber, vulcanized or thermoplastic - Determination of adhesion to a rigid substrate - 90° peel method (ISO 813:2019). (2020). https://doi.org/10.31030/3205556

192 Keim, N., Weber, A., Müller, M., Burger, D., Bauer, W., Scharfer, P., Schabel, W. & Ehrenberg, H. CMC staining method for the visualisation of the binder distribution in water-based electrodes with EDS. *ACS Applied Energy Materials* **N/A**, N/A (2025). https://doi.org/10.1021/acsaem.5c00048

193 Elliot, J. H. & Ganz, A. J. Some rheological properties of sodium carboxymethylcellulose solutions and gels. *Rheologica Acta* **13**, 670-674 (1974). https://doi.org/10.1007/BF01527058

194 Lopez, C. G., Rogers, S. E., Colby, R. H., Graham, P. & Cabral, J. T. Structure of Sodium Carboxymethyl Cellulose Aqueous Solutions: A SANS and Rheology Study. *J Polym Sci Pol Phys* **53**, 492-501 (2015). https://doi.org/10.1002/polb.23657

195 Koumarianos, S., Kaiyum, R., Barrett, C. J., Madras, N. & Mermut, O. Theory and experiment of chain length effects on the adsorption of polyelectrolytes onto spherical particles: the long and the short of it. *Phys Chem Chem Phys* **23**, 300-310 (2021). https://doi.org/10.1039/d0cp04359a

196 Bauer, W., Çetinel, F. A., Müller, M. & Kaufmann, U. Effects of pH control by acid addition at the aqueous processing of cathodes for lithium ion batteries. *Electrochimica Acta* **317**, 112-119 (2019). https://doi.org/10.1016/j.electacta.2019.05.141

197 Jagau, R., Huttner, F., Mayer, J. K., Cavers, H., Scheffler, S., Brokmann, J. & Kwade, A. Influence of Different Alginate and Carboxymethyl Cellulose Binders on Moisture Content, Electrode Structure, and Electrochemical Properties of Graphite-Based Anodes for Lithium-Ion Batteries. *Energy Technol-Ger* **11** (2023). https://doi.org/10.1002/ente.202200871

198 Yang, D. J., Li, X. J., Wu, N. N. & Tian, W. H. Effect of moisture content on the electrochemical performance of LiNiCoMnO /graphite battery. *Electrochimica Acta* **188**, 611-618 (2016). https://doi.org/10.1016/j.electacta.2015.12.063

199 Huttner, F., Haselrieder, W. & Kwade, A. The Influence of Different Post-Drying Procedures on Remaining Water Content and Physical and Electrochemical Properties of Lithium-Ion Batteries. *Energy Technol-Ger* **8**, 1900245 (2020). https://doi.org/10.1002/ente.201900245

200 Langklotz, U., Schneider, M. & Michaelis, A. Water Uptake of Tape-Cast Cathodes for Lithium Ion Batteries. *J Ceram Sci Technol* **4**, 69-76 (2013). https://doi.org/10.4416/Jcst2012-00036

201 Smith, A., Stüble, P., Leuthner, L., Hofmann, A., Jeschull, F. & Mereacre, L. Potential and Limitations of Research Battery Cell Types for Electrochemical Data Acquisition. *Batteries Supercaps* **6**, e202300080 (2023). https://doi.org/10.1002/batt.202300080

202 Yuan, Y., Lin, H., Yu, D., Yin, Y., Tang, B., Li, E. & Zhang, S. Effects of perfluorooctyltriethoxysilane coupling agent on the properties of silica filled PTFE composites. *Journal of Materials Science: Materials in Electronics* **28**, 8810-8817 (2017). https://doi.org/10.1007/s10854-017-6608-0

203 Gadhave, R. D., P.; Sorate, C. Surface Modification of Cellulose with Silanes for Adhesive Application: Review. *Open Journal of Polymer Chemistry* **11**, 11-30 (2021). https://doi.org/10.4236/ojpchem.2021.112002